



LEHIGH  
UNIVERSITY

Library &  
Technology  
Services

The Preserve: Lehigh Library Digital Collections

# Effect of mechanical properties on erosion resistance of ductile materials.

## Citation

Levin, Boris Feliksovich - Lehigh University. *Effect of Mechanical Properties on Erosion Resistance of Ductile Materials*. 1998, <https://preserve.lehigh.edu/lehigh-scholarship/graduate-publications-theses-dissertations/theses-dissertations/effect-31>.

Find more at <https://preserve.lehigh.edu/>

*This document is brought to you for free and open access by Lehigh Preserve. It has been accepted for inclusion by an authorized administrator of Lehigh Preserve. For more information, please contact [preserve@lehigh.edu](mailto:preserve@lehigh.edu).*

## INFORMATION TO USERS

This manuscript has been reproduced from the microfilm master. UMI films the text directly from the original or copy submitted. Thus, some thesis and dissertation copies are in typewriter face, while others may be from any type of computer printer.

**The quality of this reproduction is dependent upon the quality of the copy submitted.** Broken or indistinct print, colored or poor quality illustrations and photographs, print bleedthrough, substandard margins, and improper alignment can adversely affect reproduction.

In the unlikely event that the author did not send UMI a complete manuscript and there are missing pages, these will be noted. Also, if unauthorized copyright material had to be removed, a note will indicate the deletion.

Oversize materials (e.g., maps, drawings, charts) are reproduced by sectioning the original, beginning at the upper left-hand corner and continuing from left to right in equal sections with small overlaps. Each original is also photographed in one exposure and is included in reduced form at the back of the book.

Photographs included in the original manuscript have been reproduced xerographically in this copy. Higher quality 6" x 9" black and white photographic prints are available for any photographs or illustrations appearing in this copy for an additional charge. Contact UMI directly to order.

# UMI

A Bell & Howell Information Company  
300 North Zeeb Road, Ann Arbor MI 48106-1346 USA  
313/761-4700 800/521-0600



## **NOTE TO USERS**

**The original manuscript received by UMI contains pages with slanted print. Pages were microfilmed as received.**

**This reproduction is the best copy available**

**UMI**



**Effect of Mechanical Properties on Erosion Resistance of Ductile  
Materials**

by

Boris F. Levin

Presented to the Graduate and Research Committee  
of Lehigh University  
in Candidacy for the Degree of  
Doctor of Philosophy

in

Materials Science and Engineering

Lehigh University

April 1998

**UMI Number: 9831993**

---

**UMI Microform 9831993**  
**Copyright 1998, by UMI Company. All rights reserved.**

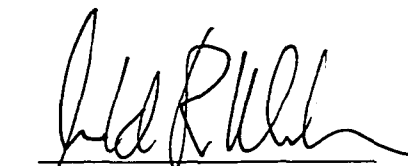
**This microform edition is protected against unauthorized  
copying under Title 17, United States Code.**

---

**UMI**  
**300 North Zeeb Road**  
**Ann Arbor, MI 48103**

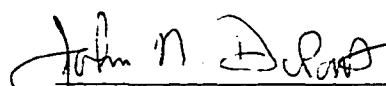
Approved and recommended for acceptance as a dissertation in partial fulfilment of the requirement for the degree of Doctor of Philosophy.

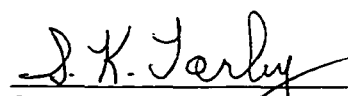
04/15/98  
Date

  
Dr. A.R. Marder  
Committee Chairman

04/15/98  
Accepted Date

Committee Members:

  
Dr. J. N. DuPont

  
Dr. S. K. Tarby

  
Dr. I. G. Wright



## Acknowledgments

I would like to express my deep appreciation to my adviser, Dr. A.R. Marder, for his support during my work at Lehigh. Thank you and Carole for teaching me so much over the past several years. Without you I would never be where I am today. I am still not sure what you saw in me six years ago, but I will be always grateful for your love and support in most difficult time of my life. You always gave me a reason to smile and were next to me when I needed. I look forward to many more occasions to taste Slivovitz, Sve-toch-nee, and sweet potatoes!

My gratitude also extends to my committee members, Drs. J. N. DuPont, S.K. Tarby, and I.G. Wright, for their guidance in my research and life at Lehigh. John, thank you for your friendship. I learned a lot from you. Most importantly, how to think critically and how not to take myself too seriously. Your confidence means a great deal to me. Dr. Tarby, your class was the first that I took at Lehigh and it was all downhill from there. I will miss our hockey discussions, Ryerson short courses and hope that Penguins will win the Cup soon. Dr. Wright, your comments and suggestions helped me to be more practical in my research and I thank you for it.

Also, I wish to thank Dr. Kristin Breder and Laura Riester from High Temperature Materials Laboratory in Oak Ridge, TN for their help during my work on the Nanoindenter.

My work at Lehigh could not have been accomplished without the assistance of Arlan Benscoter, who helped me to use common sense before doing anything. I am sorry that we never had our contest, but it would not be even close...

I must also thank my fellow graduate students from the Team Marder for their support. This unit of fabulous five includes: Stephen Banovic (Bruiser), Chad Kusco (Mr. Whitehall), Kevin Luer (The King), Jessie Nawrocki (Rock), and Don Susan (Floater). You always raised my spirit when I needed and made my life at Lehigh a lot of fun. Thank you for teaching me how to speak, proof reading my documents, and great parties. Also, I thank Antony DiGiovani and Jason Goodelle. It was a privilege to hang out with you guys and I hope that we will continue to do this! Also, I would like to thank Scott Bluni, Bruce Lindsley, Kevin Stein, and Brian Smith for helping me from my first days at Lehigh. You

taught me how to combine hard work and have fun.

I would like to thank Rory, Larisa, Emily and Rod MacFarquhar, and Stephen Feldberg for everything that you have done. I would not have enough space to describe your support. The time that I spent in Jaffrey and Cambridge is unforgettable.

I would like to thank Bob and Ruth Lipschutz for your love and support. How can I forget your English and life lessons!

Also, I wish to thank Bob and Eileen Levin-Dando and Steve and Gloria Duetch. I am very lucky to be your friend. Thank you for all the fun that we had.

I wish to thank Drs. K. Klear, M. R. Notis, and J. I. Goldstein for their kindness and trust.

I would like to thank my friends, Jason and Ted MacLean, and David Saef, who I met long time ago in another country, for their advice and help.

Last, but not least I would like to thank my parents, Felix and Anna Levin, and my brother Vitaly, for their unconditional love and support. You made many sacrifices for this dream to come through.

Funding for this work was provided by U.S. Department of Energy to whom I am very thankful

My apologies to those whom I may have inadvertently failed to mention. Thank you all!

## Table of Contents

	<b>Page</b>
<b>Acknowledgments</b>	iii
<b>List of Tables</b>	vii
<b>List of Figures</b>	viii
<b>I. ABSTRACT</b>	1
<b>II. INTRODUCTION</b>	3
<b>III. BACKGROUND</b>	4
<b>III.A. EROSION DEFINITION AND MECHANISMS</b>	4
III.A.1. Ductile materials	4
III.A.2. Brittle materials	9
III.A.3. Other erosion mechanisms	11
<b>III.B. EFFECT OF MECHANICAL PROPERTIES ON EROSION RESISTANCE</b>	12
III.B.1. Hardness	13
III.B.2. Strain hardening	18
III.B.3. Fracture toughness	26
<b>III.C. MODELING OF THE EROSION BEHAVIOR OF DUCTILE MATERIALS</b>	29
<b>III.D. SUMMARY</b>	33
<b>IV. EXPERIMENTAL PROCEDURE</b>	37
<b>IV.A. MATERIALS</b>	37
<b>IV.B. EROSION TESTING</b>	37
IV.B.1. Erosion apparatus	37
IV.B.2. Erosion sample and erodent preparation	41
IV.B.3. Steady state erosion rate determination	41
IV.B.4. Determination of tests reproducibility	44
IV.B.5. Erosion tests procedure	45
<b>IV.C. MECHANICAL TESTS</b>	45
IV.C.1. Microhardness tests and plastic zone depth estimation	45
IV.C.2. Nanoindentation tests	47
IV.C.3. Quasi-static and high strain rate compression tests	52
<b>V. RESULTS AND DISCUSSION</b>	54
<b>V.A. EROSION TESTS AND PLASTIC DEFORMATION DURING EROSION</b>	54

## **Table of Contents (cont.)**

	<b>Page</b>
<b>V.B. EROSION MODEL FOR DUCTILE MATERIALS.</b>	<b>54</b>
<b>EFFECT OF MECHANICAL PROPERTIES ON ENERGY DISSIPATION DURING EROSION</b>	
V.B.1. Plastic deformation energy	61
V.B.2. Erosion parameter	63
V.B.3. Mechanical properties during erosion	66
V.B.4. Erosion model correlation. Effect of mechanical	76
V.B.5. Summary of the erosion model for ductile materials	77
<b>V.C. ANALYSIS OF SUBSURFACE DEFORMATION DURING EROSION BY USING NANOINDENTATION TECHNIQUE</b>	<b>83</b>
V.C.1. Theoretical basis for the indentation load-displacement and stress-strain analysis.	83
V.C.2. Measurements of subsurface elastic recovery and plastic deformation.	85
V.C.3. Summary of the analysis of the subsurface deformation during erosion.	103
<b>V.D. MECHANISM OF ENERGY DISSIPATION DURING EROSION AT NORMAL IMPACT ANGLE</b>	<b>106</b>
V.D.1. Measurements of energy absorbed during erosion	106
V.D.2. Surface hardening effect during erosion	113
V.D.3. Summary of the energy dissipation during erosion	125
<b>VI. CONCLUSIONS</b>	<b>126</b>
<b>VII. REFERENCES</b>	<b>128</b>
<b>Vita</b>	<b>133</b>

## List of Tables

	<b>Page</b>
<b>Table I.</b> Chemical compositions of the tested alloys (wt %).	38
<b>Table II.</b> Erosion tests conditions.	46
<b>Table III.</b> Volumetric erosion rates for tested alloys	56
<b>Table IV.</b> Plastic zone depth due to erosion. Depth was estimated using microhardness technique.	60
<b>Table V.</b> Summary of the terms included in the erosion model.	65
<b>Table VI.</b> Hardness-Strength conversion ( $H = A \cdot \sigma$ )	79
<b>Table VII.</b> Estimated failure stress, failure, strain, and toughness values during erosion.	81
<b>Table VIII.</b> Summary of the load-displacement data for eroded materials.	91
<b>Table IX.</b> Stress-strain relationship for all materials eroded at 90° particle impact angle and velocity of 40 m/s.	96
<b>Table X.</b> Indentation stress-strain relationship obtained on samples below the eroded surface and on bulk high strain-rate compression samples (Hopkinson bar method, strain rates $10^3$ - $10^4$ s <sup>-1</sup> ).	102
<b>Table XI.</b> Comparison of the effect of strain-rate on strength increase during high strain-rate compression and erosion tests.	116
<b>Table XII.</b> Estimated strain-rate sensitivities of eroded materials.	116

## List of Figures

	<b>Page</b>
<b>Figure 1.</b> Schematic diagram of material loss during erosion of ductile materials.	6
<b>Figure 2.</b> A schematic illustration of the localization of plastic flow during indentation or erosion process.	7
<b>Figure 3.</b> A schematic diagram of the deformation and cracking during erosion of brittle materials.	10
<b>Figure 4.</b> Dependence of erosion resistance (1/volume erosion) on Vickers hardness for several pure metals and steels, and for various states of work-hardening and heat-treatment.	14
<b>Figure 5.</b> Erosion rate as a function of hardness for low chromium cast iron.	16
<b>Figure 6.</b> Schematic illustration of the deformed surface layer of an abraded or eroded material.	19
<b>Figure 7.</b> The hypothetical stress-strain curves for the erosive wear of two materials (A and B) having identical yield stresses and strain to fracture.	20
<b>Figure 8.</b> Hypothetical stress-strain curves for two materials.	22
<b>Figure 9.</b> Erosion rate vs. (Microstructural spacing) <sup>-1/2</sup> for Fe-C alloys.	25
<b>Figure 10.</b> Schematic diagram showing how the abrasive wear resistance depends on fracture toughness.	27

	<b>Page</b>
<b>Figure 11.</b> Experimentally measured erosion rates ( $\text{g/g} \cdot 10^4$ ) for Cu-Zn and Cu-Al alloys plotted versus calculated erosion rates using data presented in Reddy et al. [43] erosion model.	34
<b>Figure 12.</b> Schematic diagram of the test apparatus used for erosion research.	39
<b>Figure 13.</b> Schematic diagram of the Laser Doppler Velocimeter.	40
<b>Figure 14.</b> Plot of the particle velocity and data rate across the erodent stream.	42
<b>Figure 15.</b> Schematic diagram of the erosion kinetics.	43
<b>Figure 16.</b> Schematic diagram of the microhardness profile that was taken in order to estimate plastic zone size due to erosion.	48
<b>Figure 17.</b> Schematic diagram of the Nano Indenter® II.	49
<b>Figure 18.</b> Schematic diagram of the typical load-displacement curve obtained during the nanoindentation test.	51
<b>Figure 19.</b> Volume loss versus erosion time plots for all materials tested.	55
<b>Figure 20.</b> Microhardness profiles obtained on the cross-sections of the eroded samples after the longest exposure time (240 min).	57
<b>Figure 21.</b> Stress-strain curves generated for each material over a range of strain rates.	68
<b>Figure 22.</b> Stress-strain curves of several of the materials which were first tested at high strain rate at room temperature, then reloaded at low strain rate.	73

	<b>Page</b>
<b>Figure 23.</b> Schematic diagram showing procedure that was used to estimate tensile toughness during erosion using high-strain-rate compression and microhardness tests.	80
<b>Figure 24.</b> Erosion parameter calculated from Equation 20 is plotted against experimentally determined volumetric erosion rate.	82
<b>Figure 25.</b> Indentation load, P, versus displacement, d, for tested materials as a function of distance from the eroded surface.	87
<b>Figure 26.</b> Effect of hardness on restitution coefficient.	94
<b>Figure 27.</b> Dependence of the restitution coefficient, e, within the velocity range 20-100m/s on the Vickers hardness.	95
<b>Figure 28.</b> Stress-strain curves obtained by using load-displacement measurements at various distances below the eroded surface of the 316L SS alloy. .	97
<b>Figure 29</b> Correlations between indentation tests performed on annealed materials and conventional compression tests performed on the bulk samples.	99
<b>Figure 30.</b> Indentation stress-strain diagrams obtained for samples below the eroded surface and on bulk high strain-rate compression samples (Hopkinson bar method, strain rates $10^3$ - $10^4$ s <sup>-1</sup> ).	100



	<b>Page</b>
<b>Figure 31.</b> A schematic diagram of change in microhardness with distance from the eroded surface.	108
<b>Figure 32.</b> The slopes of microhardness profiles for all materials are plotted against their average strain hardening coefficient within the plastically deformed volume.	109
<b>Figure 33.</b> A schematic diagram that illustrates calculation of the area under the microhardness curve.	111
<b>Figure 34.</b> Erosion parameter calculated from equation 35 is plotted against experimentally determined volumetric erosion rates.	114
<b>Figure 35.</b> The effect of hardness on strain-rate sensitivity. Strain-rate sensitivity decreases with increasing hardness.	119
<b>Figure 36.</b> The effect of strain-rate sensitivity and hardness on plastic zone size during erosion. a) strain-rate sensitivity effect; b) hardness effect.	121
<b>Figure 37.</b> Combined effect of strain-rate sensitivity and hardness ( $m/H$ ) on plastic zone size during erosion.	122

## **I. ABSTRACT**

Solid particle erosion (SPE) resistance of ductile Fe, Ni, and Co-based alloys as well as commercially pure Ni and Cu was studied. A model for SPE behavior of ductile materials is presented. The model incorporates the mechanical properties of the materials at the deformation conditions associated with SPE process, as well as the evolution of these properties during the erosion induced deformation. An erosion parameter was formulated based on consideration of the energy loss during erosion, and incorporates the material's hardness and toughness at high strain rates. The erosion model predicts that materials combining high hardness and toughness can exhibit good erosion resistance. To measure mechanical properties of materials, high strain rate compression tests using Hopkinson bar technique were conducted at strain rates similar to those during erosion. From these tests, failure strength and strain during erosion were estimated and used to calculate toughness of the materials. The proposed erosion parameter shows good correlation with experimentally measured erosion rates for all tested materials.

To analyze subsurface deformation during erosion, microhardness and nanoindentation tests were performed on the cross-sections of the eroded materials and the size of the plastically deformed zone and the increase in materials hardness due to erosion were determined. A nanoindentation method was developed to estimate the restitution coefficient within plastically deformed regions of the eroded samples which provides a measure of the rebounding ability of a material during particle impact. An increase in hardness near the eroded surface led to an increase in restitution coefficient. Also, the stress rates imposed below the eroded surface were comparable to those

measured during high strain-rate compression tests ( $10^3$ - $10^4$  s<sup>-1</sup>).

A new parameter, "area under the microhardness curve" was developed that represents the ability of a material to absorb impact energy. By incorporating this parameter into a new erosion model, good correlation was observed with experimentally measured erosion rates. An increase in area under the microhardness curve led to an increase in erosion resistance. It was shown that an increase in hardness below the eroded surface occurs mainly due to the strain-rate hardening effect. Strain-rate sensitivities of tested materials were estimated from the nanoindentation tests and showed a decrease with an increase in materials hardness. Also, materials combining high hardness and strain-rate sensitivity may offer good erosion resistance. A methodology is presented to determine the proper mechanical properties to incorporate into the erosion parameter based on the physical model of the erosion mechanism in ductile materials.

## **II. INTRODUCTION**

Solid Particle Erosion (SPE) is a loss of material during repetitive impacts of solid particles and is one of the primary reasons for the damage of power generation components, such as boiler tubes, turbine blades, and valve stems. Damage associated with SPE costs the utility industry at least \$150 million annually in reduced efficiency of power generation [1]. One method to combat SPE is to select erosion resistant materials for use in components that are subject to an erosive environment. Therefore, the design and proper selection of the erosion resistant materials can significantly reduce operating cost of power generation facilities.

Depending upon its mechanical properties, a material may erode by different mechanisms or a combination of mechanisms. Since the mechanical properties of a material are a reflection of its composition and microstructure, many attempts have been made to correlate erosion resistance to some readily measurable mechanical properties. Some of these properties include hardness, ductility, yield strength, strain hardening coefficient, fatigue strength and fatigue strain hardening coefficient [2,3]. However, no simple correlation to predict erosion resistance using a single property or combination of properties has been developed. There is wide uncertainty as to what various erosion mechanisms exist, and to what mechanical properties control erosion behavior of materials.

The purpose of this research is to achieve a fundamental understanding of the effect of mechanical properties on erosion resistance of ductile materials. Once this effect is understood, the microstructure and composition of a material can be optimized to

provide the best combination of mechanical properties for erosion protection. The results of this research can be useful for developing selection criteria for erosion resistant materials based upon their mechanical properties.

### **III. BACKGROUND**

#### **III.A. EROSION DEFINITION AND MECHANISMS**

Erosion is defined as the progressive loss of original material from a solid surface due to mechanical interaction between the surface and impinging solid particles [4].

Erosion mechanisms may include plastic deformation, chipping, cracking, and melting. Specific mechanisms depend upon the composition, microstructure and mechanical properties of the material being eroded, along with the composition, size, shape, density, velocity, and angle of impact of the eroding particles [5].

##### ***III.A.1. Ductile Materials***

Hutchings et al. [6] established that the erosion mechanism for ductile materials shows certain common features, irrespective of the alloy type. In all cases, severe plastic deformation occurs in a localized region surrounding the point of particle impact. The observed erosion mechanism involves three distinct stages that occur sequentially at any one location. In the initial stage, an impacting particle forms a crater and the material extruded or displaced from the crater forms a raised lip. In the second stage, the displaced metal is deformed by subsequent impacts; this may lead to lateral displacement of the surface material, and can be accompanied by some ductile fracture in heavily strained regions. Finally, after relatively few impacts, the displaced material becomes so

severely strained that it is detached from the surface by ductile fracture. Evidence of this mechanism for erosion of ductile materials has been observed by other authors [7,8] and a schematic diagram of this process is shown in **Figure 1**.

A description of the ductile erosion mechanism in terms of the mechanical properties was presented by Bitter [9]. During impact, when the yield strength of the material is locally exceeded, plastic deformation takes place in the vicinity of the impact. After multiple impacts, a plastically deformed surface layer forms near the eroded surface, and therefore, the yield strength of the material increases due to strain hardening. Upon further deformation, the yield strength at the surface of the material will eventually become equal to its fracture strength and no further plastic deformation will occur. At this point, the material surface becomes brittle and its fragments may be removed by the subsequent impacts.

Sundararajan [10] suggested that erosion of ductile materials is accompanied by accommodation of the strain underneath the eroded surface. When a critical strain is exceeded in the deformation volume beneath the surface, material is detached from the eroded surface by ductile fracture. In this case, the ability of a material to *absorb* impact energy through plastic deformation may play a major role in its erosion resistance.

Sundararajan then proposed that formation of the erosion lip is controlled by the strain localization [11, 12]. A schematic illustration of the strain localization process is shown in **Figure 2** [12]. According to this mechanism, during the initial stages of erosion, the particle impact energy is absorbed by a large volume of material that deforms homogeneously and exhibits net strain hardening ( $d\sigma/d\epsilon > 0$ , where  $\sigma$  is the flow stress

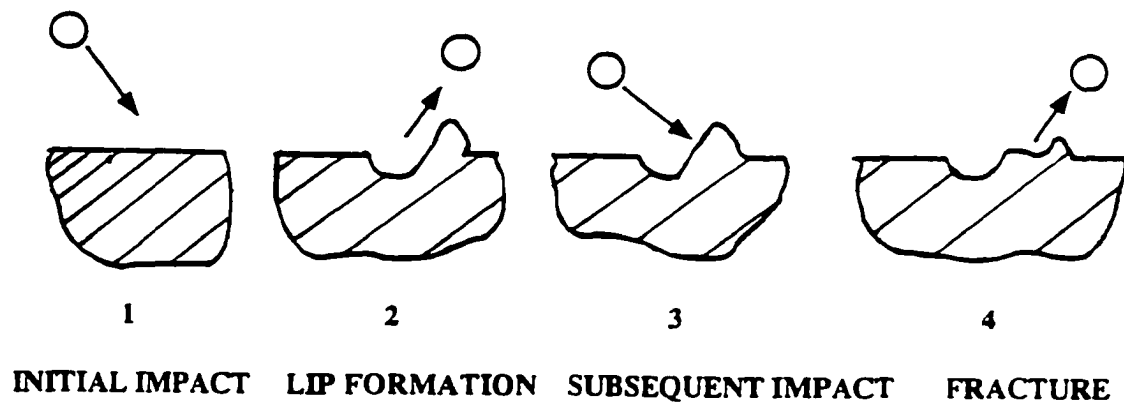


**Figure 1.** Schematic diagram of material loss during erosion of ductile materials.

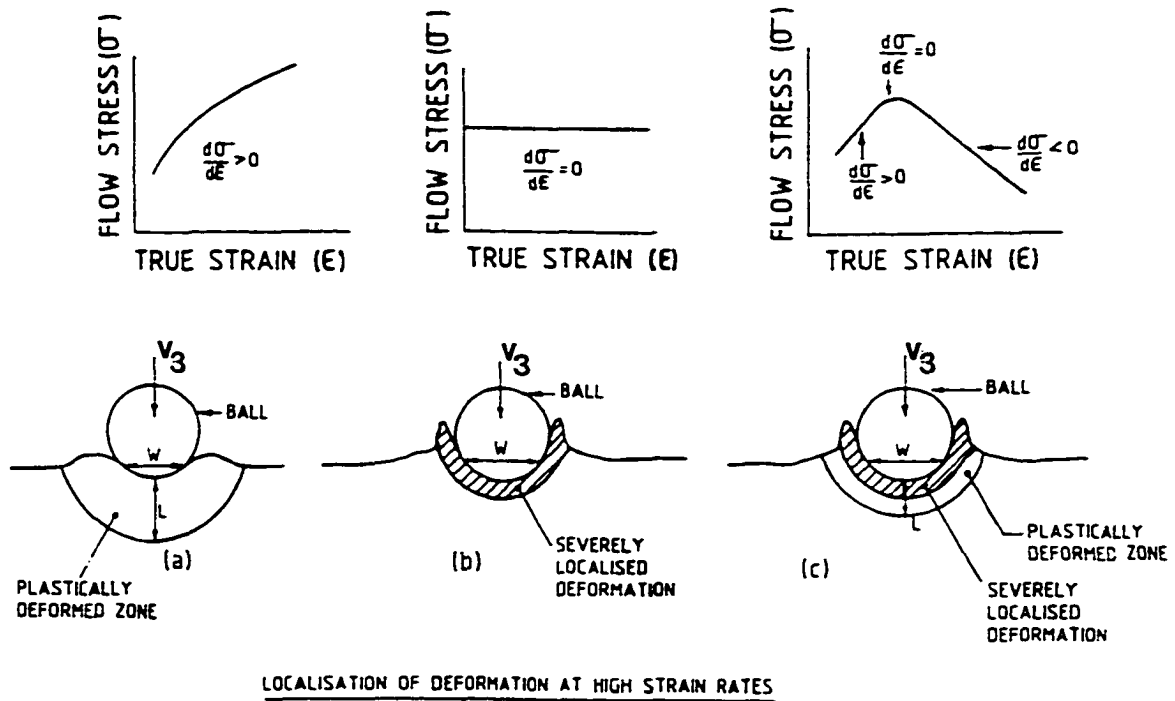


**Figure 2.** A schematic illustration of the localization of plastic flow during indentation or erosion process.



and  $\epsilon$  is the true strain). As a result of strain hardening, a plastically deformed zone develops beneath the impacting particle (**Figure 2a**). However, when a certain critical localization strain is reached, the eroded material loses its strain hardening capacity ( $d\sigma/d\epsilon=0$ ). Thus, deformation beneath the impacting particle becomes localized only to the near surface layers leading to an extrusion of material (lip formation) as shown in **Figure 2b**. At strains higher than the localization strain, deformation becomes even more localized and material may exhibit softening behavior ( $d\sigma/d\epsilon<0$ ) due to the heating and dynamic re-crystallization in the vicinity of the eroded surface, **Figure 2c**.

The proposed strain localization mechanism indicates that material near the eroded surface should be perfectly plastic ( $d\sigma/d\epsilon=0$ ) or soften ( $d\sigma/d\epsilon<0$ ). However, nanoindentation tests performed on cross-sections of the several eroded materials (single and multiple impacts) showed no softening within the erosion lip or beneath the eroded surface for nickel-base Hastelloy C-276, annealed 1100 Al, and 7075-T6Al alloys [13]. On the other hand, some softening was observed near the eroded surface of the ordered iron-aluminum ( $\text{Fe}_3\text{Al}$ ) alloy [13]. In contrast to the  $\text{Fe}_3\text{Al}$  alloy, transmission electron microscopy (TEM) analysis of eroded copper showed no evidence of dynamic re-crystallization or softening near the eroded surface [14]. Also, a TEM examination revealed an increase in dislocation cell diameter with distance from the eroded surface. Hardness or flow stress is inversely proportional to the dislocation cell size according to [15,16]:

$$\tau = \frac{KGb}{d} \quad (1)$$

where  $\tau$  is the flow stress,  $d$  is the dislocation cell diameter,  $G$  is the shear modulus,  $b$  is the Burgers vector, and  $K$  is a constant. Thus, an increase in dislocation cell diameter with distance from the eroded surface causes a decrease in hardness with distance from the surface that is often observed in strain hardened materials. It should be noted that, although some materials may exhibit softening at the eroded surface, the strain localization model may not be applied to materials that do not exhibit softening during erosion.

In summary, erosion mechanisms for ductile materials are complex and involve significant plastic deformation below the eroded surface. Therefore, the energy absorption properties of eroded materials are important in determining their erosion resistance.

### ***III.A.2. Brittle Materials***

The erosion of brittle materials, (i.e., ceramic-type materials) involves brittle fracture, chipping, and cracking after particle impact [4]. When a particle strikes the material surface, the material may remain undamaged, it may fracture, or deform by plastic flow. Hard particles striking relatively soft targets will tend to produce large plastic deformation. However, brittle materials do not experience significant plastic deformation and therefore, brittle fracture (radial and lateral cracking) occurs during an impact [17]. A schematic diagram of the deformation and cracking during erosion is shown in **Figure 3** [18]. The lateral cracks propagate parallel to the surface, while radial/median cracks propagate outward from the contact zone. Evans et al. [19] established that erosion loss in ceramics is related to the formation and growth of only

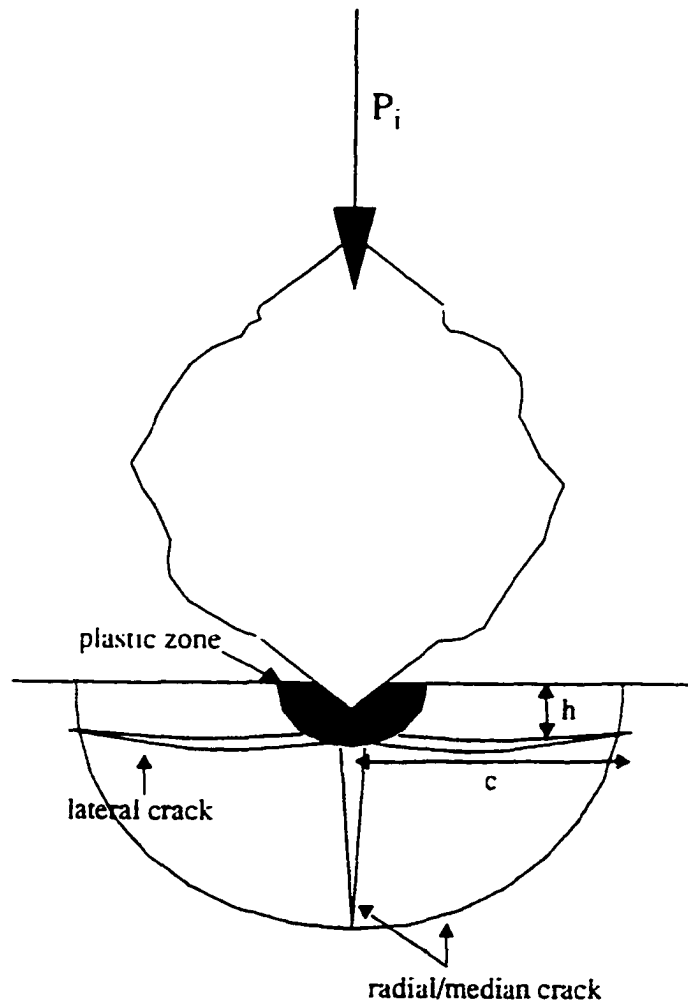


**Figure 3.** A schematic diagram of the deformation and cracking during erosion of brittle materials.

lateral cracks. Therefore, the severity of the erosion damage in brittle material is determined by the depth of the lateral crack layer. Lateral cracks form because of the large tensile stresses resulting from the strain mismatch between the plastically deformed zone and elastically deformed surroundings [18, 19]. Since erosion of brittle materials involves crack formation and propagation, fracture toughness appears to be an important property that contributes to their erosion resistance.

### ***III.A.3. Other Erosion Mechanisms***

Several other erosion mechanisms have been proposed to account for loss of material. Material removal by melting has been suggested by some investigators [20,21,22]. A large portion of the kinetic energy of the impacting particles may transform into heat during plastic deformation around the impact area. This may lead to a significant temperature rise in this region. Doule et al. [20] suggested that the maximum temperature rise is determined by the work done on the target material, its specific heat and density. For example, it was calculated that a local temperature rise of about 200<sup>0</sup>C may be experienced during particle impact on steel [20]. Because of this temperature increase, local thermal cycling may assist the formation and propagation of subsurface cracks and, therefore, accelerate material loss. It appears that in low melting point materials, particle impact may cause surface melting and accelerated erosion, while melting is unlikely to occur in high melting point materials. For example, Hutchings et al. [23] have suggested that melting is not an important erosion mechanism in steels.

Other proposed erosion mechanisms are associated with the cyclic nature of deformation (repetitive impacts) at the eroded surface and involve cyclic fatigue

processes. Richman et al. [3] have found that the *cavitation erosion* rate for different steels and nickel-base alloys is inversely proportional to their fatigue strength,  $\sigma_f$ . However, there are few definitive experimental observations (i.e., striations) to prove a fatigue-type mechanism for the case of *solid particle erosion*.

### **III.B. EFFECT OF MECHANICAL PROPERTIES ON EROSION RESISTANCE**

Many studies have been conducted to determine the effect of mechanical properties of various materials on their erosion resistance. However, good correlations were obtained only within narrow classes of materials. The effect of mechanical properties on erosion resistance depends on the mechanism of material removal. For example, for ductile materials the erosion process involves significant plastic deformation near the eroded surface. Therefore, the material properties that contribute to its ability to absorb plastic deformation may contribute to erosion resistance. These properties include toughness, ductility, strain hardening coefficient, and hardness. In contrast to ductile materials, brittle materials erode by forming lateral and radial cracks below the eroded surface. Typically, the depth of crack formation below the surface and crack propagation through the material determines the erosion wastage. Thus, properties such as hardness and fracture toughness are expected to contribute to erosion resistance of brittle materials. By determining the effects of mechanical properties on erosion resistance, the microstructure of a given alloy can be optimized to provide the best combination of mechanical properties for erosion protection.

### ***III.B.1. Hardness***

In the past, the hardness of a material was thought to be the property that determined erosion resistance. For pure metals, some correlation between erosion rate and hardness has been shown by Finney et al.[24]. The best correlation was found with the hardness of the metal in the fully annealed condition, rather than with the hardness of the metal in a heavily work-hardened condition. The dependence of erosion resistance on hardness for different materials is shown in **Figure 4** [24]. It can be seen that for metals in the fully annealed condition, an increase in hardness led to an increase in the erosion resistance. However, deviation of three metals (W, Mo, Fe), with BCC crystal structures, from the straight line relationship was not explained by the authors. Also, **Figure 4** indicates the deviation of the work hardening materials from the straight line relationship. In addition, several heat treated steels exhibited independence of erosion rate from hardness. Several other researchers have reported that the erosion rate is not dependent on material hardness [25,26]. Levy et. al [25] showed that an increase in the hardness of a steel by microstructural modifications can lead to an *increase* in erosion rate. For example, soft 1075 carbon steel with a spheroidized microstructure exhibited better erosion resistance than harder 1075 carbon steel with perlitic microstructure.

Oca et al. [26] have shown that for a series of tool steels, carbon steels, brass, copper, and aluminum, erosion resistance was proportional to the surface hardness after erosion. Also, Hutchings [17], proposed that the effect of hardness on erosion resistance is strongly dependent on the properties of the erosive particles (velocity, shape, size, and density). When hard angular particles strike a relatively soft target, the target surface

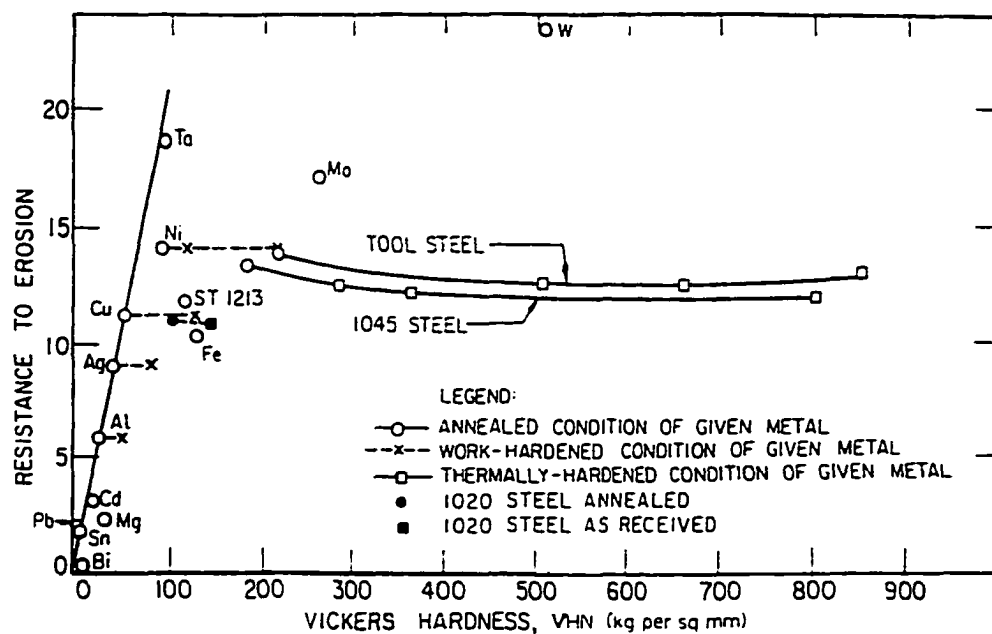


**Figure 4.** Dependence of erosion resistance (1/volume erosion) on Vickers hardness for several pure metals and steels, and for various states of work-hardening and heat-treatment.

will tend to deform plastically. On the other hand, erodent particles of lower hardness may distort or even fragment on impact. In this case, erosion damage will decrease as the target hardness increases. This theory is in good agreement with results obtained by Guo et al. [27]. The authors found that, when eroded by hard silicon carbide particles, the erosion resistance of low chromium white cast irons did not change significantly with a hardness increase. However, when eroded by softer particles (glass sand) the erosion resistance of cast irons increased with an increase in hardness. Researchers suggested that for a softer erodent, the impacting particles are easily broken and therefore, produce less damage to the surface. The effect of the erodent particle hardness and target material hardness on erosion resistance of white cast irons is shown in **Figure 5** [27]. It can be seen that when eroded by soft glass sand particles, the erosion rate decreases with an increase in target hardness. But when eroded by hard silicon carbide particles, the erosion rate increases with an increase in target hardness. In addition, the effect of hardness on erosion resistance depends on the velocity of the erosive particles. For example, it was established that a critical particle velocity below which plastic deformation of the target does not occur is proportional to the target hardness. This relationship is given by [28]:

$$v_c = 4.3H^{2.5}J^2\rho^{-0.5} \quad (2)$$

$$J = \frac{(1-\mu_t^2)}{E_t} + \frac{(1-\mu_p^2)}{E_p} \quad (3)$$

where  $v_c$  is the critical velocity,  $H$  is the hardness of the target material,  $J$  is a parameter



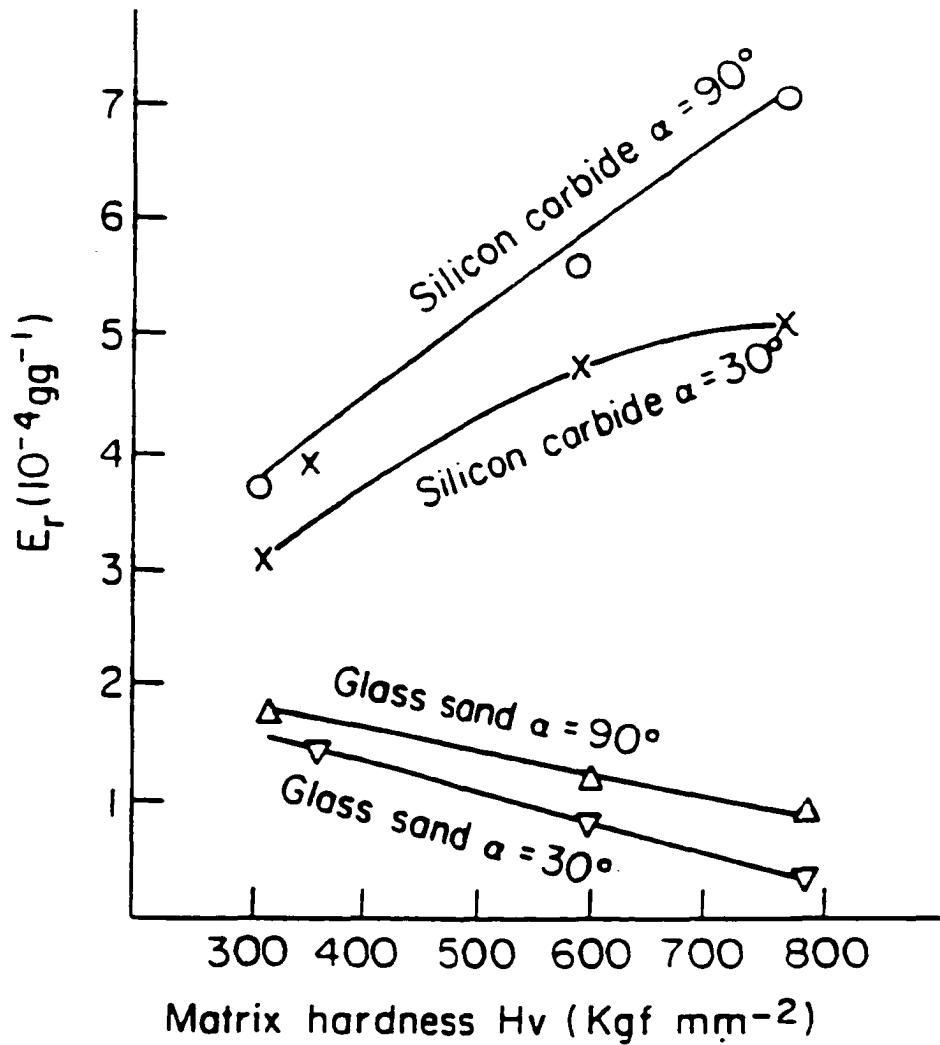


**Figure 5.** Erosion rate as a function of hardness for low chromium cast iron. Two different erodent were used (silicon carbide and glass sand).  $\alpha$  is the particle impact angle and  $E_r$  is the erosion rate.

that depends on elastic modulus of the target and particle materials (eq 3),  $\rho$  is the density of the impacting particle,  $u_t$  and  $u_p$  are the Poisson coefficients of the target and particle materials, respectively, and  $E_t$  and  $E_p$  are the elastic modulus of the target and particle materials, respectively. Based on equation 2, it can be suggested that at low particle velocities ( $v_p < v_c$ ) materials with high hardness may offer good erosion resistance because particles cannot produce plastic deformation and/or cracking of the target material. However, at high particle velocities ( $v_p > v_c$ ), when plastic deformation and/or cracking are common, hardness may not significantly contribute to the erosion resistance of the target.

Evans et al. [19] found that for ceramic materials an increase in hardness led to a decrease in depth of cracking and thus, decreased erosion damage. Several empirical expressions that relate erosion damage in ceramics to their hardness and fracture toughness were obtained [18,19,29,30]. These expressions have the general form of [18]:

$$Z \sim E^n * H^p * K_{Ic}^q \quad (4)$$

where  $Z$  is the erosion rate,  $E$  is elastic modulus,  $K_{Ic}$  is fracture toughness,  $H$  is hardness, and  $n, p, q$  are constants. Typically, values for  $p$  range between -1.4 to -0.25, while values for  $q$  range between -1.3 to -1 [18,19]. These results suggest that brittle materials with high hardness and fracture toughness may provide good erosion resistance. However, for many ceramics, an increase in hardness causes a decrease in fracture toughness. Thus, only an optimum combination of these properties can result in improved erosion resistance.

In spite of many attempts to correlate hardness to the erosion resistance of various alloys, no adequate quantitative relationship was obtained. The effect of hardness on erosion resistance must be considered in relation to other material properties, erodent properties (i.e. size, shape, and density), and erosion test conditions (i.e. velocity).

### ***III.B.2. Strain Hardening***

Several studies proposed that material loss during erosion occurs when a critical fracture strain is attained at the surface [10-12]. A critical fracture strain may be achieved locally after single or multiple impacts by the erodent particles. As a result of particle impact, the material is plastically deformed and the dislocation density increases in the vicinity of the impact. The increase in dislocation density leads to an increase in hardness at the surface. It should be noted that as material is lost at the attainment of the critical strain, the material below the surface is still plastically yielding. A schematic diagram of this process is shown in **Figure 6** [31]. Ball [31] proposed that in order to design a material to resist erosion, attention must be given to providing a microstructure which ideally never accumulates the critical fracture strain under the stress imposed by the impacting particles. Therefore, the ability of a material to accommodate impact energy through plastic deformation may contribute to its erosion resistance.

Materials with high strain hardening capacity are able to dissipate impact energy and therefore, the critical strain is accumulated after a much longer time. This effect is illustrated in **Figure 7** [31]. In this figure the hypothetical stress-strain curves for the erosive wear of two materials (A and B) are shown. The impacting particles produced a

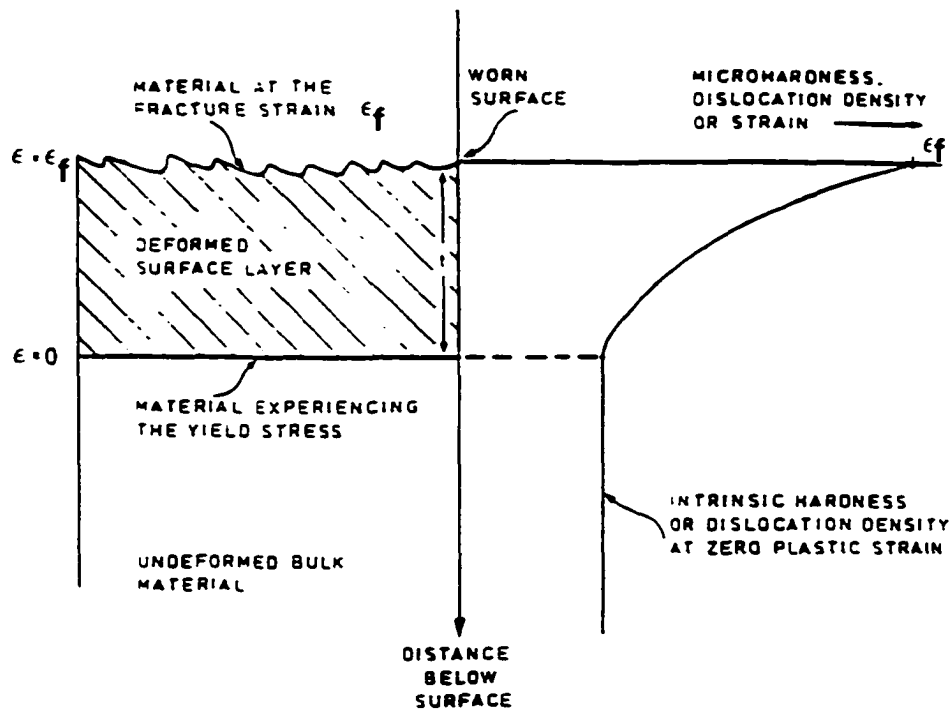


**Figure 6.** Schematic illustration of the deformed surface layer of an abraded or eroded material. The curve on the right-hand side indicates the change in microhardness, dislocation density or strain with depth below the worn surface.

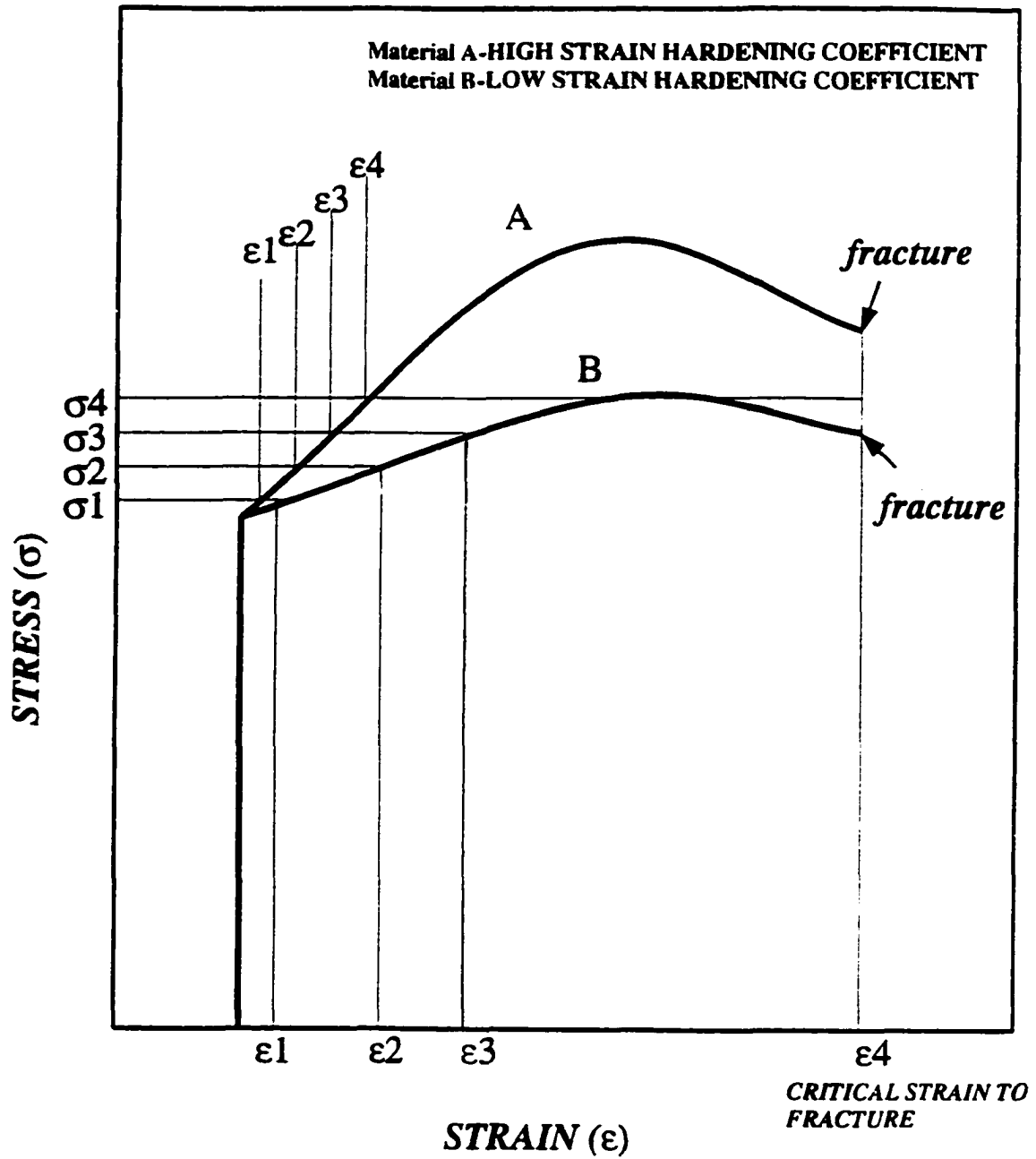


**Figure 7.** The hypothetical stress-strain curves for the erosive wear of two materials (A and B) having identical yield stresses and strain to fracture. The strains ( $\epsilon$ ) produced in each material by erosive particles having stress magnitudes from  $\sigma_1$  to  $\sigma_4$  are indicated.

stress that increased from  $\sigma_1$  to  $\sigma_4$ . As a result of stress increase, the strains ( $\epsilon$ ) produced in each material are also increased. From this figure it can be seen that material with a higher strain hardening coefficient (material A) requires a higher stress to achieve the critical strain to fracture compared to a material with low strain hardening coefficient (material B). Gee [32] pointed out that generally metals with face centered cubic (FCC) crystal structures exhibit superior wear resistance compared with body centered cubic (BCC) metals at equivalent hardness. This effect was attributed to the higher strain hardening coefficient ( $n$ ) of the FCC metals. This coefficient appears in the following relationship:

$$\sigma_t = K\epsilon_t^n \quad (5)$$

where,  $\sigma_t$  is the true stress,  $\epsilon_t$  is the true strain, and  $K$  is a strength coefficient. However, the strain hardening coefficient is not the only factor that contributes to the amount of energy that materials can absorb during particle impact. The area under the stress-strain curve represents the energy per unit volume that a material can absorb before fracture (tensile toughness) and can be found by integrating eq. 5:

$$T = K \frac{\epsilon_f^{n+1}}{n+1} \quad (6)$$

Thus, toughness depends on fracture strain, strength, and the strain hardening coefficient. For example, if a material has a high strain hardening coefficient but low fracture strain, its toughness may be lower than for a material with a low strain hardening coefficient and high strain to fracture. **Figure 8** illustrates this effect. The ability of a material to

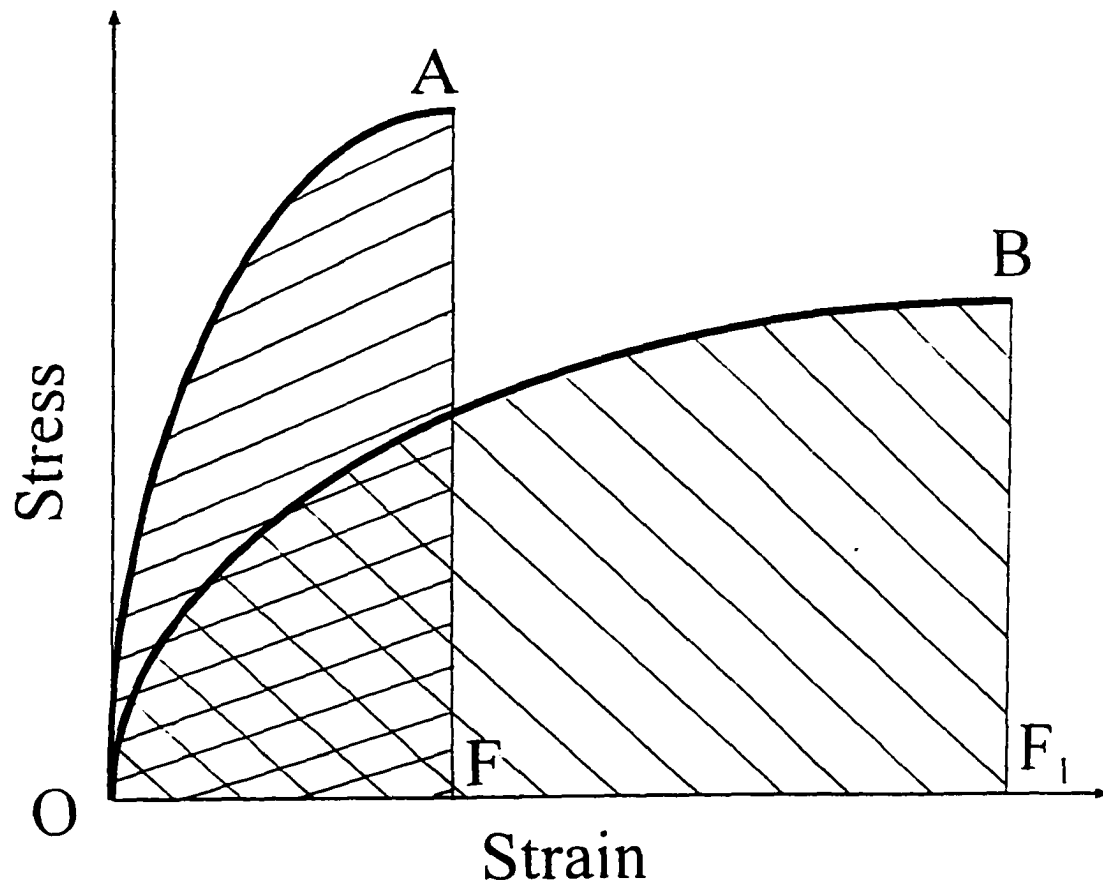


**Figure 8.** Hypothetical stress-strain curves for two materials. This figure illustrates that toughness is a material property that combines the effects of strength, strain hardening, and strain. Material A has a high strength, high strain hardening coefficient, and low fracture strain, while materials B has a low strength, low strain hardening coefficient, and high fracture strain. Toughness of material B (area OFB) is higher than that for material A (area OAF).

absorb energy during particle impact cannot be characterized based upon only one property (i.e., strain hardening coefficient, strength, fracture strain). The combined effect of these properties on the tensile toughness must be considered and only then correlations with erosion resistance may be drawn. Some examples that illustrate different effects of strain hardening on toughness and erosion resistance are discussed below.

Venugopal et al. [33] have studied the erosion behavior of Cu-Al, Cu-Zn, and Cu-Si alloys. It was documented that their erosion rates decreased linearly with an increase in the strain hardening coefficient. The authors suggested that a higher  $n$  value corresponds to a higher critical strain necessary for material removal. As a result of an increase in the critical strain to fracture, the erosion resistance of tested alloys increased. However, Srinivas et al. [34,35] have found that for the series of steels (1040, Cr-Mo and A533 B) with relatively high fraction of second phase particles (i.e., carbides), an increase in strain hardening coefficient led to a decrease in the critical strain to fracture. It is believed that void nucleation in materials that consist of a high fraction of second phases particles occurs either by decohesion of the particle/matrix interface or by breaking of the particles when the local stress exceeds a critical value [36]. Higher strain hardening coefficient values enable rapid attainment of the critical stress for decohesion of the particle/matrix interface. Therefore, a lower critical strain is required to promote fracture. Also, second phase particles may disrupt plastic flow during plastic deformation [21]. As a result of this, the fracture strain significantly decreases. However, Lindsley et al. [37] found that an increase in carbide volume percent in iron from 0 to 20 vol.% could lead to improved erosion resistance. It was found that microstructural spacing, and not the



volume fraction of the second phase, was the critical parameter that controls erosion resistance. The researchers established that erosion rate was proportional to the microstructural spacing parameter according to:

$$E=0.090-0.040\Lambda^{-1/2} \quad (7)$$

where E is the erosion rate and  $\Lambda$  is the microstructural spacing. The microstructural spacing parameter was defined as:

$$\Lambda=\frac{(1-f)}{N} \quad (8)$$

where f is carbide volume fraction and  $N_i$  is the number of ferrite-ferrite and ferrite carbide boundaries. **Figure 9** shows the effect of microstructural spacing on erosion resistance [37]. It was concluded that, since the erosion is controlled by plastic deformation of the ductile matrix, barriers that impede the movements of dislocations in the materials, such as grain boundaries and carbides within the grains, as well as at the grain boundaries, determine the erosion resistance. Although the presence of carbides may decrease failure strain of metal-carbide composites, the increase in strength produced by these carbides can contribute to the erosion resistance.

Strain hardening coefficient may have a different effect on the critical strain to fracture for single phase materials. For example, with commercially pure iron, an increase in the strain hardening coefficient (n) leads to an increase in the critical strain to fracture [35]. In single phase systems fracture nucleation occurs by slip band impingement on grain boundaries or by intersection of slip bands [32]. Therefore, a

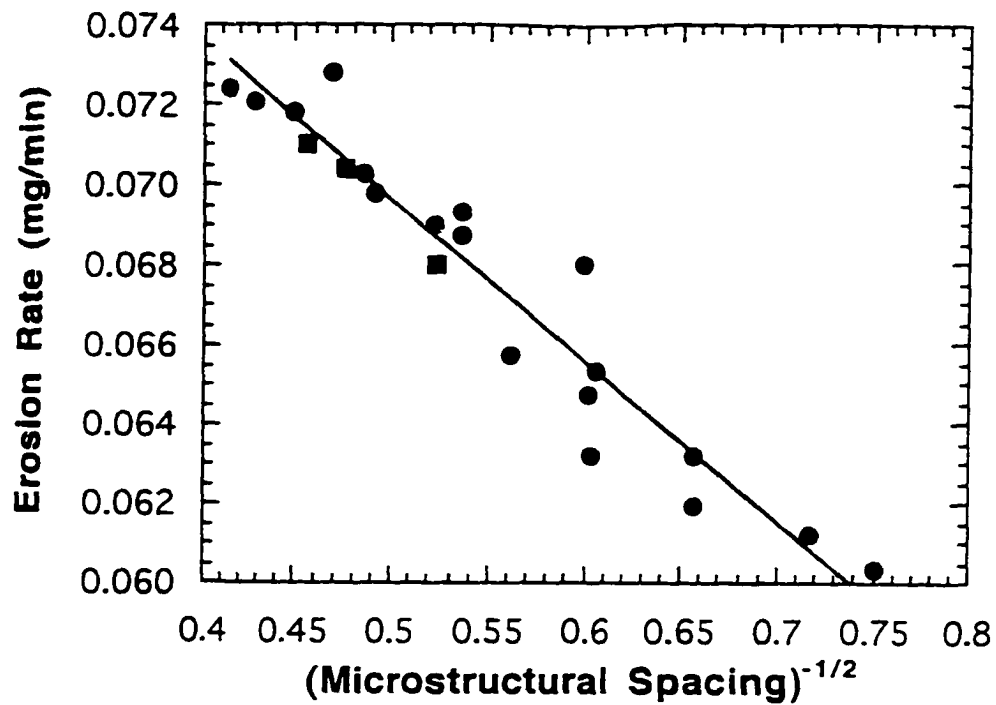


**Figure 9.** Erosion rate vs.  $(\text{Microstructural spacing})^{-1/2}$  for Fe-C alloys. Alloy 0.2 wt.% C is given by the square points and alloy 1.4 wt.% C is given by the circle points. Erosion conditions: velocity 40m/s,  $90^\circ$  impact angle, and  $\text{Al}_2\text{O}_3$  erodent.

higher strain is required to initiate fracture. As a result of this effect, toughness of commercially pure iron was found to be proportional to the strain hardening coefficient.

Strain hardening and plastic deformation play an important role in determining the erosion resistance of ductile materials. However, the effect of strain hardening on erosion resistance may vary with the alloy system. With single phase materials, an increase in strain hardening coefficient may lead to an increase in the erosion resistance, while with multiphase materials an increase in the strain hardening coefficient may lead to a decrease in the erosion resistance. Only a few metallic systems were studied to evaluate the effects of strain hardening and fracture strain on erosion resistance. Moreover, toughness, a material property that *combines* the effects of stress, strain hardening, and fracture strain on fracture energy may be a better property to represent erosion resistance of ductile materials. In addition, the erosion behavior of brittle materials that do not deform plastically cannot be explained based upon the strain hardening concept.

### ***III.B.3. Fracture Toughness***

The fracture toughness of a material is defined by Hertzberg [38] as a unique stress intensity level that causes fracture. It is well known that fracture toughness is a primary factor that contributes to a material's resistance to crack propagation. Since erosion of brittle materials is accompanied by subsurface crack initiation and propagation, fracture toughness may contribute to their erosion resistance.

The effect of fracture toughness on two-body abrasion resistance is shown in **Figure 10 [17]**. The author hypothesized that the erosion resistance of materials varies

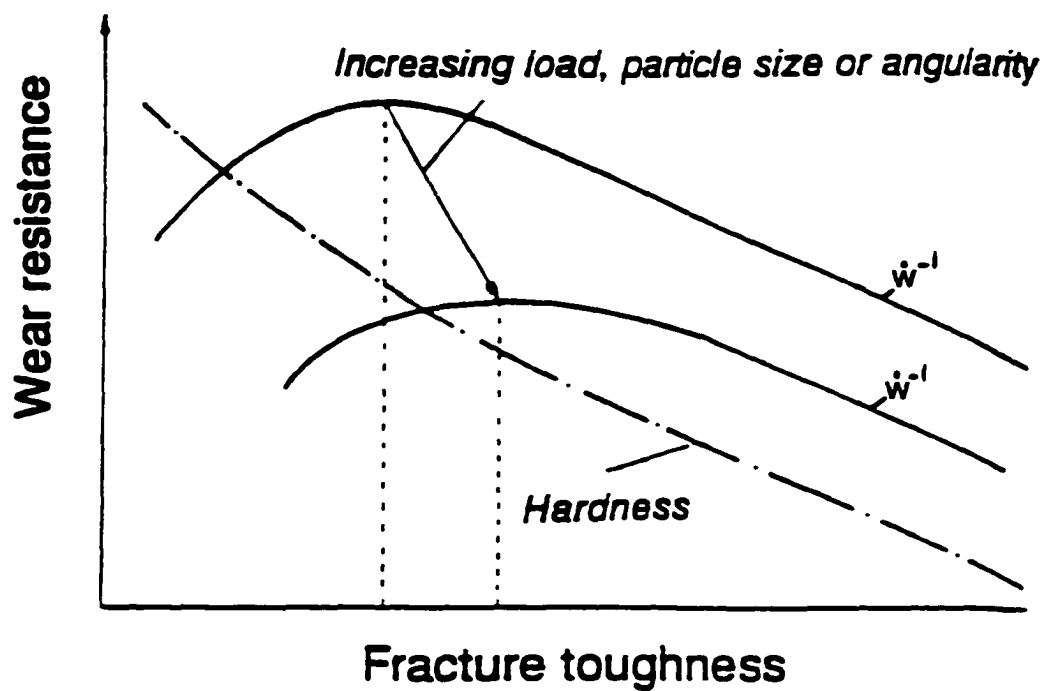


**Figure 10.** Schematic diagram showing how the abrasive wear resistance depends on fracture toughness. The hardness of the target material is also indicated, falling as the fracture toughness increased.

with fracture toughness in the same manner as abrasion resistance. **Figure 10** illustrates that abrasion resistance initially increases with an increase in fracture toughness. However, when fracture toughness reaches a certain critical value, wear resistance decreases with further increase in fracture toughness. Hutchings [17] proposed that during abrasion of low fracture toughness materials, brittle fracture is the primary mechanism of abrasion. Therefore, an increase in fracture toughness leads to a decrease in abrasion wear rate. On the other hand, in materials with relatively high fracture toughness, abrasive wear is controlled by plastic deformation. In this case the abrasive wear rate is controlled by the hardness of the material. Hutchings [17] suggested that the peak in the abrasion resistance-fracture toughness curve (**Figure 10**) occurs at the point of transition between the two regimes, in which wear is controlled by fracture toughness or hardness, respectively. Thus, the optimum combination of hardness and fracture toughness provides the best abrasion resistance.

Guo et al. [27] have studied the erosion behavior of brittle low chromium white cast irons. When eroded by hard silicon carbide particles, the erosion rate drastically decreased as the matrix fracture toughness increased. The microstructure of low chromium white cast irons consists of a large volume fraction of hard chromium carbides within a soft iron-chromium matrix. The erosion mechanism of these materials may include microcutting, subsurface crack initiation and propagation, spalling, and fragmentation of carbides. When eroded by much harder silicon carbide particles, the chromium carbides cannot absorb the energy of impact. This leads to crack initiation and crack growth into the matrix. However, if the matrix has a high fracture toughness it can

partially absorb the impact energy and delay crack propagation and fracture, thus leading to lower erosion rate. Several authors have concluded that, when impacted by a harder erodent, materials with a high fracture toughness and hardness offer good protection against erosion [18, 19, 27].

In summary, the effect of mechanical properties on erosion resistance is complex because of property interdependence. For example, an increase in hardness may lead to a decrease in toughness. This may explain a relative insensitivity of erosion wastage to the changes in any one mechanical property, as found by many studies. It appears that erosion resistance is controlled by a combination of mechanical properties and to determine this combination, a physical model of the erosion process must be developed.

### **III.C. MODELING OF THE EROSION BEHAVIOR OF DUCTILE MATERIALS**

Erosion modeling has become important in the design of materials because of the need to predict erosion behavior based on mechanical properties and environmental conditions. Usually, erosion modeling consists of two steps. First, a theoretical model is developed that explains the observed erosion process and second, derivation of the mathematical expressions to predict the erosion resistance. A few theories have been developed to explain the erosion mechanisms of ductile materials (see section III.A.). However, no accurate quantitative prediction of erosion resistance has been produced.

One of the first erosion models for ductile materials was developed by Finnie et al. [24]. This model assumed that the target material is an ideally plastic (non-work hardening) solid. The authors proposed that hardness is the only material property that

controls the erosion process and the erosion rate expression was given as:

$$V=v^2 * \frac{g(\alpha)}{S_y \mu \theta f} \quad (8)$$

where  $S_y$  is the dynamic hardness of eroded material,  $v$  is the particle velocity,  $g(\alpha)$  is a function that adjusts particle velocity for the normal and tangential components depending on impact angle,  $\mu$  is the ratio between vertical and horizontal force of the particle,  $\theta$  is the ratio between the depth of particle contact and depth of the erosion damage, and  $f$  is the factor that accounts for the non-ideal nature of the eroded particle. Parameters,  $\mu$ ,  $\theta$ , and  $f$  were assumed to be constant. Finnie's model predicts maximum erosion rate for ductile materials to occur between 15 and 30° particle impact angle. This result was later verified by many studies. However, the proposed erosion model significantly underestimates erosion rates at normal impact angle. It is expected that ductile materials exhibit significant work hardening during normal impact because the maximum amount of impact energy is transferred into the material. But, Finnie's model assumes that eroded materials do not experience work hardening. Clearly, this assumption is unrealistic and could explain underestimates of erosion rates for normal impact angle. Also, this model predicts that erosion rate is inversely proportional to material hardness. While this is true for some pure metals, for many ductile materials erosion rate does not depend on material hardness (see Section III.A.2.).

Bitter [9] was the first researcher to consider the effect of work hardening in developing an erosion model. He argued that repeated impacts of particles will form a

plastically deformed layer beneath the eroded surface and hardness of this layer will increase with each impact until it becomes equal to the failure strength of the material. At this point, surface material is removed by subsequent impacts. Bitter then proposed that erosion rate is equal to the ratio of the input kinetic energy to the energy needed to remove a unit volume of the material. Input kinetic energy was determined from the Hertzian theory of elastic contact taking into consideration elastic properties of impacting particle and target material. However, the energy needed to remove a unit volume of the material could only be determined by fitting the experimentally measured erosion rate to the equation describing the erosion process. Also, no correlation between experimentally measured and calculated erosion rates for the same experimental conditions (i.e., constant impact angle and velocity) was shown. In addition, the strain rate effect during erosion was not addressed in this model. Therefore, it is difficult to use Bitter's erosion model in predicting erosion rates of ductile materials.

Hutchings [40] considered erosion to be a low-cycle fatigue process caused by repeated plastic straining of the target by impacting particles. Material is removed from the surface when a critical fatigue failure strain ( $\epsilon_c$  or "erosion ductility") is reached. According to the Coffin-Manson equation, fatigue failure strain is equal to:

$$\epsilon_c = \Delta\epsilon_p N_f^{1/2} \quad (9)$$

where  $N_f$  is the number of particles (impact cycles) and  $\Delta\epsilon_p$  is the strain increment introduced by each impact. Hutchings suggested that erosion rate is inversely proportional to  $N_f$ , and using the relationship between materials hardness ( $H$ ) and plastic



strain increments during each impact ( $\Delta\epsilon_p$ ), derived an equation to predict erosion rate:

$$E = 0.033 \frac{\alpha \rho \sigma^{1/2} v^3}{\epsilon_c^2 H^{1.5}} \quad (10)$$

where  $E$  is the unitless erosion rate,  $\alpha$  is a constant,  $\rho$  is the target density,  $\sigma$  is the erodent density,  $v$  is the particle velocity, and  $H$  is the dynamic hardness of the target. However, in Hutchings's model,  $\epsilon_c$  or the "erosion ductility" parameter could only be determined from the experimental measurements of erosion rate. Thus, it is difficult to use this model to predict erosion rates. Although this model predicted reasonably well the variation of erosion rate with velocity for Al 6061-T6 alloy, no correlations were presented for different materials at the same velocity. Therefore, it is difficult to evaluate the effect of mechanical properties parameter  $\epsilon_c^2 H^{1.5}$  on erosion resistance.

Only a few attempts have been made to measure the plastic zone size that forms in ductile materials in the vicinity of the eroded surface [41,42,43, 44]. This is particularly surprising, since the size of the plastically deformed region may represent a measure of energy absorbed before fracture during erosion. Only one erosion model [43] accounted for the plastic zone size. Assuming that the plastic zone depth is proportional to the size of the crater that forms during impact, the researchers concluded that erosion rate is proportional to  $L^3$  ( $L$  is the plastic zone depth) according to.

$$E = \frac{0.02 L^3 \rho_r F(t) \Delta\epsilon_m}{r_3 \rho_b \epsilon_c} \quad (11)$$

where  $E$  is the dimensionless erosion rate,  $L$  is the depth of plastic deformation,  $\rho_t$  is the target density,  $\rho_b$  is impacting particle density,  $F(t)$  is a numerically evaluated function dependent on temperature,  $\Delta\epsilon_m$  is the mean strain increment per impact,  $r$  is the impacting particle radius, and  $\epsilon_c$  is the critical strain for erosion lip formation. The authors concluded that their model showed good correlation with experimentally measured erosion rates for several Cu-Zn and Cu-Al alloys. However, upon plotting predicted erosion rates versus experimentally measured erosion rates in **Figure 11**, no significant correlation was observed. Also, this model contains several parameters that are not readily measurable and require post erosion analysis. Therefore, its applicability for selection of erosion resistant materials is limited. Moreover, the assumed relationship between the plastic zone depth and crater volume needs to be justified. For example, if the material is relatively soft and does not show significant work hardening (i.e., pure iron), its plastic zone depth may be small, but its crater size may be large. It is possible that the size of the plastic zone is controlled by the strain hardening ability of the material, while the size of the crater is controlled by material hardness or resistance to particle penetration.

### III. D. SUMMARY

The effect of mechanical properties on erosion resistance is complicated because of property interdependence. This may explain a relative insensitivity of erosion wastage to the changes in any one mechanical property that was found by many studies. It appears that the erosion resistance is controlled by a combination of mechanical properties and to determine this combination, a physical model of the erosion process

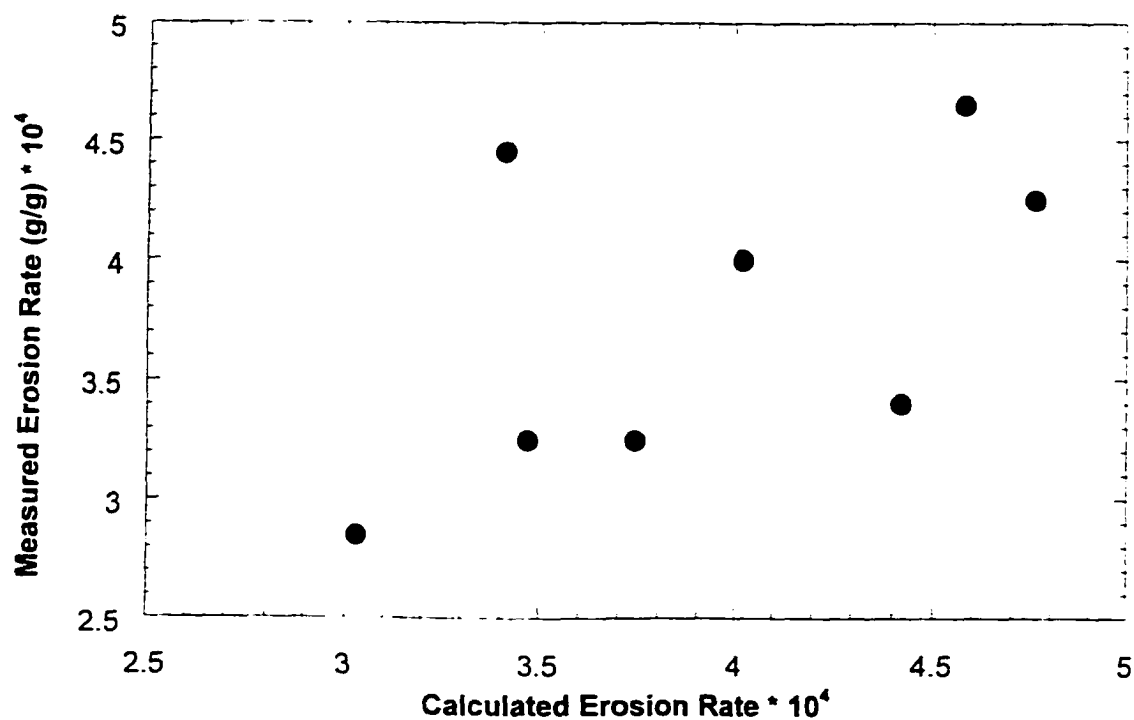


**Figure 11.** Experimentally measured erosion rates ( $\text{g/g} * 10^4$ ) for Cu-Zn and Cu-Al alloys plotted versus calculated erosion rates using data presented in Reddy et al. [43] erosion model.

must be developed.

Several models were proposed to correlate erosion resistance to material properties. Although these models showed a reasonable correlation with erosion resistance for different alloy systems, their major simplification is a neglect of the work hardening in ductile materials during particle impact. It was assumed that materials had constant mechanical properties during erosion (i.e., hardness, yield strength, fracture strain). However, because of work hardening, the material hardness will increase in the vicinity of the eroded surface and the strain introduced by each impact will be reduced. When work hardening of the eroded surface is considered, modeling of the erosion behavior becomes complex because of the change in mechanical properties within the plastically deformed zone. Thus, the efforts to model erosion behavior of ductile materials without considering the effect of work hardening do not accurately represent the mechanism of material removal in these materials.

To develop a quantitative model for erosion of ductile materials, it is essential to consider the energy balance during particle impact. Investigation of the relationship between erosion resistance and the energy transmitted from the impacting particle into the target material is a valid approach for the development of an erosion model. The portion of this energy that is *actually transferred* into the material depends on the material's mechanical properties such as yield strength, strain hardening coefficient, modulus, etc. Also, the size of the plastically deformed region may provide an estimate of the material's ability to absorb particle impact energy. In order to determine the effect of mechanical properties on erosion resistance, their effect on the plastic zone size that

forms during erosion must be investigated.

Finally, the development of an erosion model requires consideration of the strain rate effect on mechanical properties of materials. During erosion, the particles impose high strain rate deformation on the material. The erosion process involves strain rates on the order of  $10^3$ - $10^6$   $\text{sec}^{-1}$  [45]. In contrast, mechanical properties of a material are typically measured from low strain rate (quasi-static,  $10^{-2}$   $\text{sec}^{-1}$ ) tensile tests. Therefore, if a material is strain rate sensitive, the mechanical properties measured from a quasi-static tensile test may be different from those during solid particle erosion. For example, Meng et al. [2] reported that the dynamic hardness for some materials may be 10 times higher than their quasi-static hardness. Therefore, it is necessary to use dynamic mechanical properties for correlations with erosion resistance.

## **IV. EXPERIMENTAL PROCEDURE**

### **IV.A. Materials**

Six annealed ductile alloys (Ultimet, Inconel-625, Hastelloy C22, Haynes 230, 316L SS, and B3) and two commercially pure metals (Nickel and Copper,) were used in this study. Their chemical compositions were determined by the optical emission spectroscopy and are shown in **Table I**. The selected materials provided a broad variation in mechanical properties and therefore, the effect of mechanical properties on the erosion behavior of ductile materials could be analyzed.

### **IV.B. Erosion Testing**

#### **IV.B.1. Erosion apparatus**

A schematic diagram of the erosion tester that was used in this investigation is shown in **Figure 12**. The system is driven by an air compressor which can deliver up to  $1.65 \times 10^{-2} \text{ m}^3/\text{s}$  of air (35 scfm) at  $8.62 \times 10^5 \text{ Pa}$  (125 psi). The air is cleaned through a series of filters to remove any entrained water. The flow meter and pressure regulator control the amount of air that flows through the system. The air can be heated by two inline fluid heaters to temperatures up to  $500^\circ \text{C}$  by exiting the heaters. Eroding particles are fed into the air stream with a screw feeder to ensure constant feed rates. The particles and air are accelerated and impinge upon the sample at any angle between  $0^\circ$  and  $90^\circ$ .

The particle velocity distribution prior to impact is directly measured with a TSI Laser Doppler Velocimeter (LDV). A 20mW He-Ne laser produces a beam which first splits and then crosses under the particle stream as shown in **Figure 13**. The receiving

**Table I.** Chemical compositions of the tested alloys (wt %).

Alloy	Co	Cr	Fe	Mn	Mo	Ni	W	Ta	Cu	Other
Ultimet	Bal.	25.5	3.0	0.8	4.3	8.9	1.3	--	--	0.24Si , 0.07C
Inconel 625	--	21.6	4.4	0.03	8.9	Bal.	--	--	--	3.49N b0.26 Ti 0.15Al 0.02C
Hastelloy C22	1.8	21.6	5.0	0.23	13.8	Bal.	2.9	--	--	0.18V 0.007 C
Haynes 230	0.3	24.0	1.4	0.5	1.8	Bal.	13.2	--	--	0.33Al 0.07C 0.43Si
316L SS	--	17.3	Bal.	1.5	2.0	11.0	--	--	--	0.02C 0.5Si
B3	--	1.2	--	0.54	27.2	69.0	--	--	--	0.34Al
Nickel 200	--	--	0.2	--	--	99.2	--	--	--	
Copper	--	--	--	--	--	0.044	--	--	99.9	--

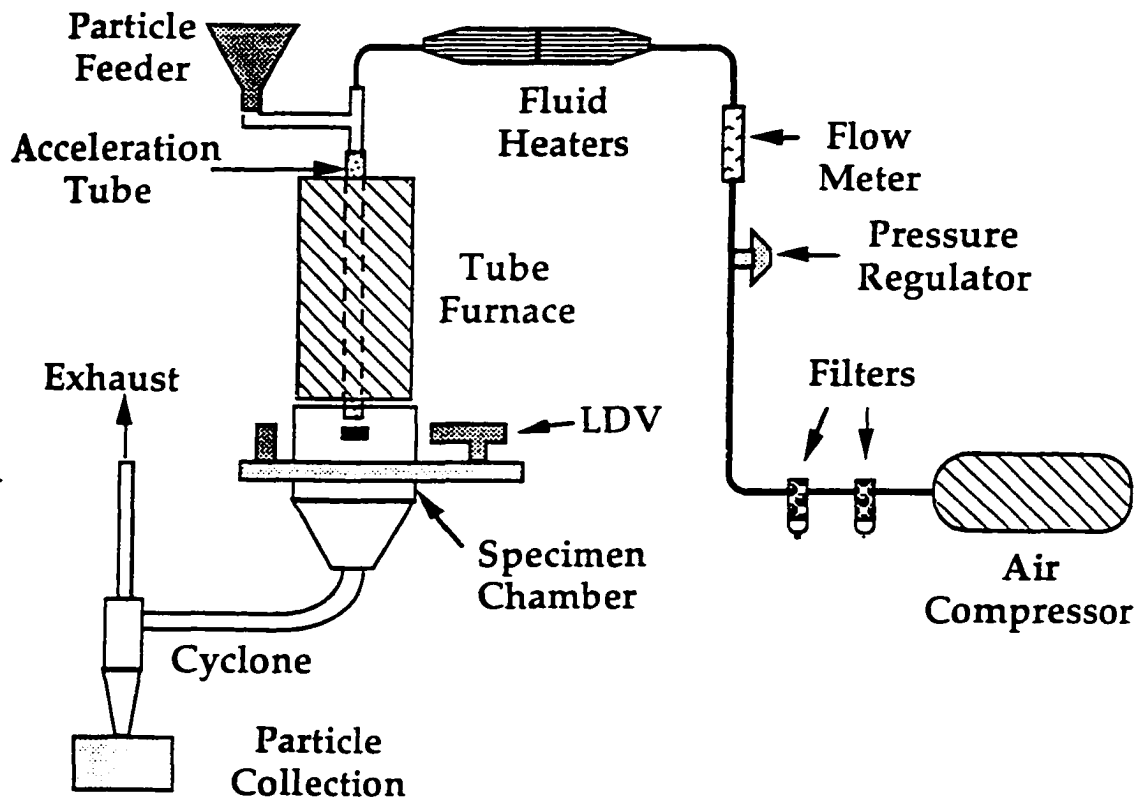


**Figure 12.** Schematic diagram of the test apparatus used for erosion research.



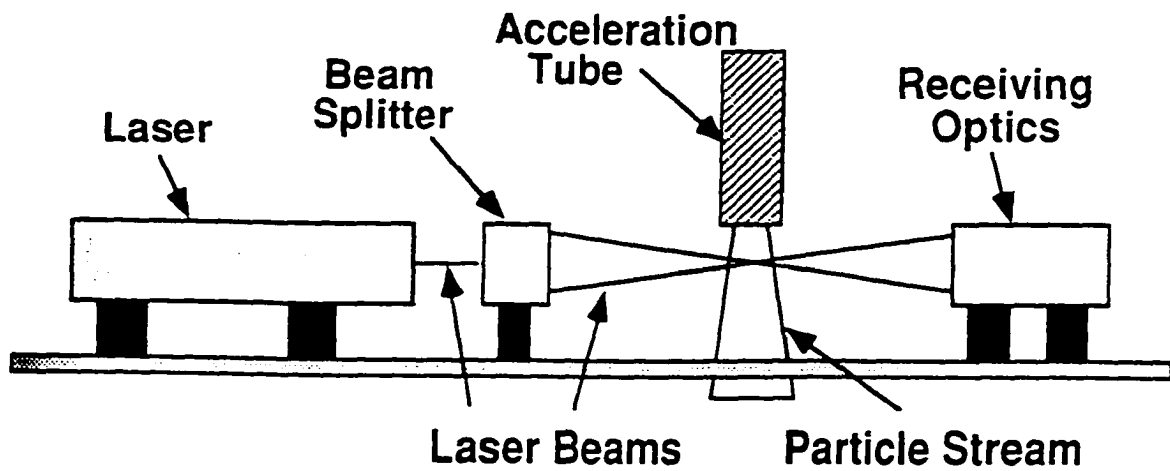


**Figure 13.** Schematic diagram of the Laser Doppler Velocimeter.

optics measure the interference between the laser and the particles and TSI computer software translates the data into a velocity profile. **Figure 14 [46]**, shows the velocity profile of the particles exiting the acceleration tube just before impact with the sample. It can be seen that, because the particle stream spreads out after exiting the acceleration tube, velocity quickly drops off outside a radius of 0.45 cm (0.175 in). Therefore, sample size of 0.95 cm x 0.95 cm (3/8" x 3/8") was chosen so that most of the sample surface area resided in the maximum velocity portion of the stream. Additional information regarding the erosion apparatus can be found in reference [47].

#### **IV.B.2. Erosion sample and erodent preparation**

The erosion samples were cut to a size of 3/8" x 3/8"  $\pm$  0.005" using a water cooled low speed diamond saw. Each sample was mechanically polished to a 1  $\mu$ m surface finish. Brown alumina (96% Al<sub>2</sub>O<sub>3</sub>, 3% TiO<sub>2</sub>), which has a size range from 300  $\mu$ m to 550  $\mu$ m was used as an erodent. The alumina was sieved to between 355  $\mu$ m and 425  $\mu$ m to minimize its size distribution because larger particles may cause a higher erosion rate. Thus, the narrow particle size range minimizes the error in erosion rate associated with the different size of the as-received alumina. Also, only fresh alumina particles (i.e., particles were not re-used) were used for the erosion tests.

#### **IV.B.3. Steady state erosion rate determination**

The erosion kinetics that are typical for most materials is schematically shown in **Figure 15**. Initially, the weight loss of a given material as a function of erosion time often displays a relatively short incubation period with little or no material removal. The material eventually experiences surface weight loss and surface hardening at the same

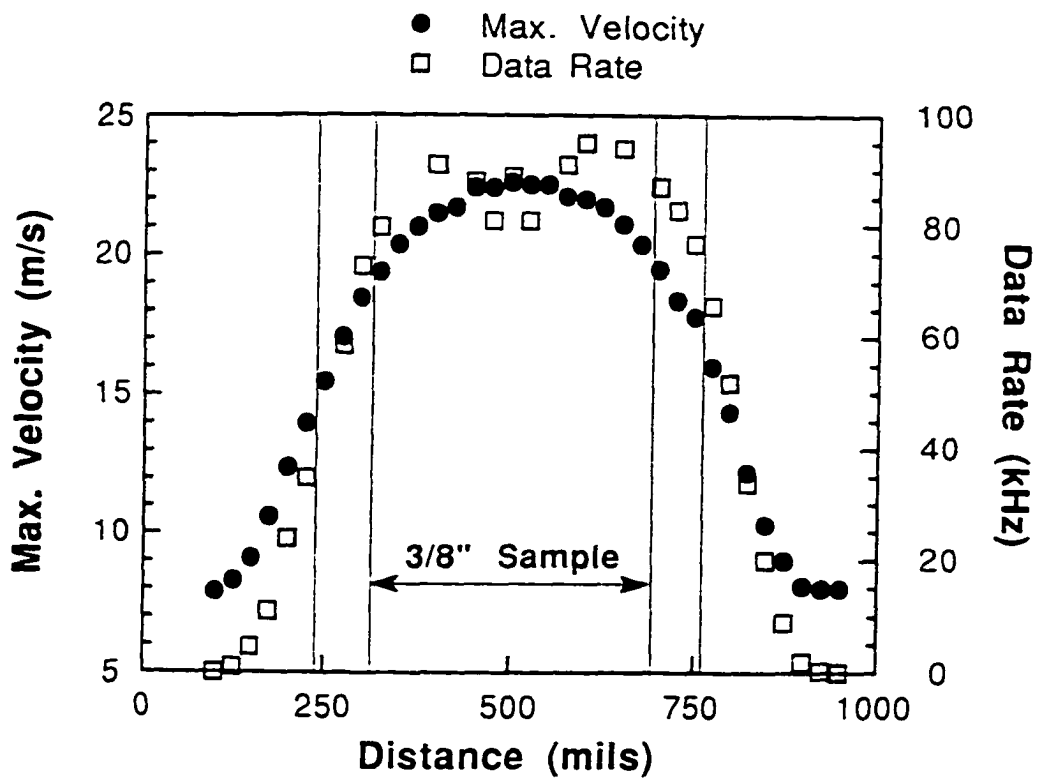


**Figure 14.** Plot of the particle velocity and data rate across the erodent stream. The vertical lines indicate the distance across the width and the diagonal of the erosion sample.

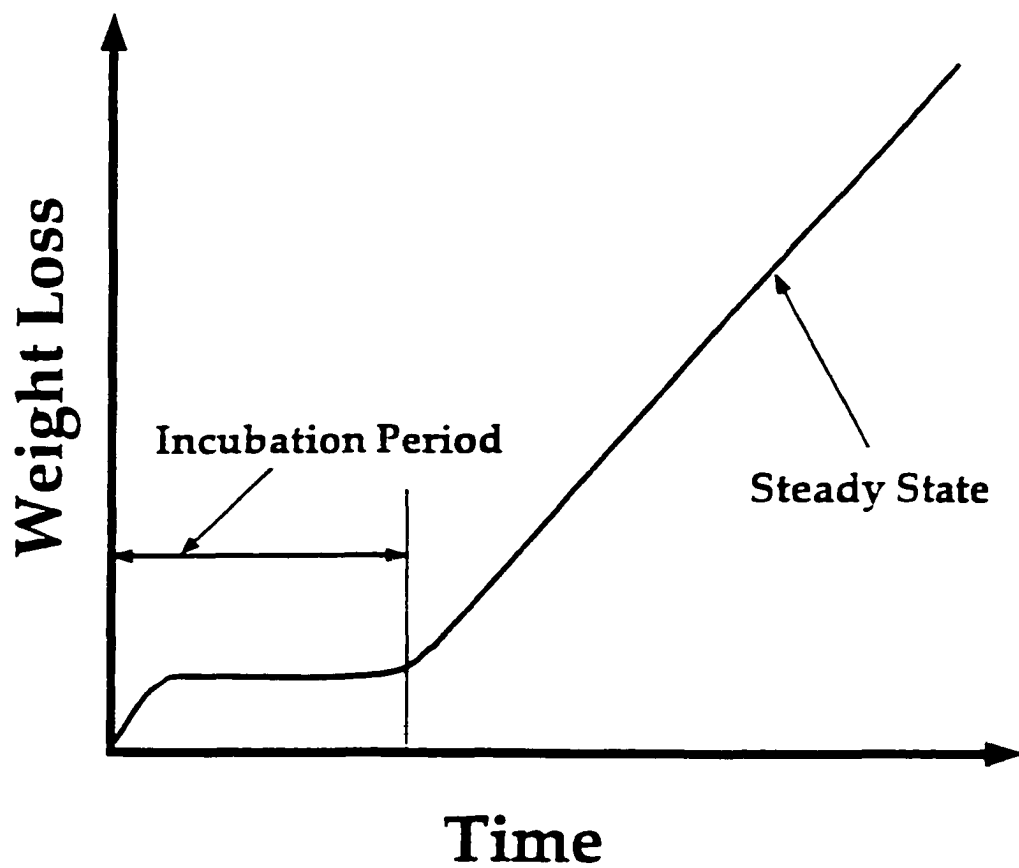


**Figure 15.** Schematic diagram of the erosion kinetics.

rates and attains a steady state erosion rate. Steady state erosion is defined by the linear portion of the weight loss versus time plot, as shown in **Figure 15**. Determination of the steady state erosion rate is very important from a practical point of view since most of the material removal occurs during this period. In order to adequately obtain the weight loss vs. erosion time plots, eight different erosion exposure times (30, 60, 90, 120, 150, 180, 210, 240 min.) were used for each material. To quantify weight loss during the erosion experiments, the erosion specimens were ultrasonically cleaned in acetone and weighed before and after the erosion tests to the nearest 0.1 mg using Mettler College 150 balance. A linear regression analysis was performed on the data in the steady state erosion regime of the weight loss versus time plots, the slopes of which yielded the steady state erosion rate. The volumetric erosion rates were obtained by dividing the weight loss rate by the density of the corresponding material. It is essential to determine volumetric erosion rates in order to compare materials with different densities. For example, two materials with different densities may exhibit an equal weight loss due to erosion, however, the high density material will have a lower volume loss than a material with lower density. Densities of all materials were experimentally measured using the Archimedes method.

#### **IV.B.4. Determination of tests reproducibility**

Lindsley [46] analyzed the reproducibility of the erosion tests using the Lehigh University erosion apparatus. The author conducted several erosion tests for the same material and determined that the standard deviation in erosion rate was less than 1%, indicating good reproducibility of the erosion tests. However, some deviation has been

noted between different groups of erosion tests (i.e., tests for the same materials run at different times of year). Possible causes of deviation include changes in air humidity and wear of the erosion tester itself, resulting in changes in air and particle flow. Therefore, if erosion samples were to be run at different times, a standard sample would be used to compare erosion rates. Also, each alloy was tested at least once per day, to ensure that slight changes in the operation of the erosion tester from day to day were experienced by each sample. Moreover, the order of the samples to be tested on each day was also chosen at random. These measures were taken to limit the error in the erosion rate determination for each material.

#### **IV.B.5. Erosion tests procedure**

Erosion test conditions used in this study are summarized in **Table II**. All materials were tested at a  $90^0$  impact angle and a velocity of 40 m/s. Erosion samples were cross-sectioned after testing using a low speed diamond saw. The samples were then mounted in cold curing, thermosetting epoxy and metallographically prepared using standard techniques to a 0.04  $\mu\text{m}$  surface finish. These samples were used to analyze the sub-surface damage in the eroded materials by microhardness and nanoindentation techniques.

#### **IV.C. Mechanical Tests**

##### **IV.C.1. Microhardness tests and plastic zone depth estimation**

To measure the depth of the deformed region beneath the eroded surface, microhardness tests were performed on a cross-section of each material after the longest exposure time in the erosion tester. The plastic zone depth was estimated by obtaining a

**Table II.** Erosion tests conditions.

Eroded Sample Planar Dimensions	0.95 cm x 0.95 cm
Sample Temperature	20 °C
Erodent Particle Velocity	40 m/s $\pm$ 3 m/s
Erodent Particles Flux	8.50 mg/(mm <sup>2</sup> /sec)
Impingement Angle	90 °
Erodent	angular brown alumina (Al <sub>2</sub> O <sub>3</sub> )
Erodent Size Range	355-425 $\mu$ m

microhardness profile from the eroded surface into the base material. A schematic diagram of this technique is shown in **Figure 16**. The depth at which the hardness value becomes constant is defined as the plastic zone depth. In order to minimize the specimen edge effect on microhardness results, the measurements were conducted using a Knoop indenter with a test load of 10g. Microhardness tests were conducted according to ASTM E 384 standard [48] and indents started at the distance of 5-10  $\mu\text{m}$  from the eroded surface, depending upon the size of the indent. Three to five microhardness profiles were obtained in different locations of each material in order to improve the statistical significance of the data. From these profiles, the size of the plastic zone and increase in surface hardness due to erosion were determined.

#### **IV.C.2. Nanoindentation tests**

Nanoindentation tests were performed at the Oak Ridge National Laboratory using the Nano Indenter<sup>®</sup> II system, **Figure 17** [49]. The load on the indenter is generated through the use of a current carrying coil and permanent magnet assembly. The resolution of the loading system is 50 nN. The displacement of the indenter is measured with a three plate capacitive system with a resolution of 0.04 nm. A detailed description of the system has been presented elsewhere and will not be discussed here [50]. In contrast to conventional microhardness tests, the Nano Indenter<sup>®</sup> II system is able to measure the displacement of the indenter as a function of the applied load within a small volume of the material. The use of this depth-sensing indentation technique made it possible to analyze the load-displacement and stress-strain response of the material within the plastically deformed layer (<150  $\mu\text{m}$ ) below the eroded surface. These results



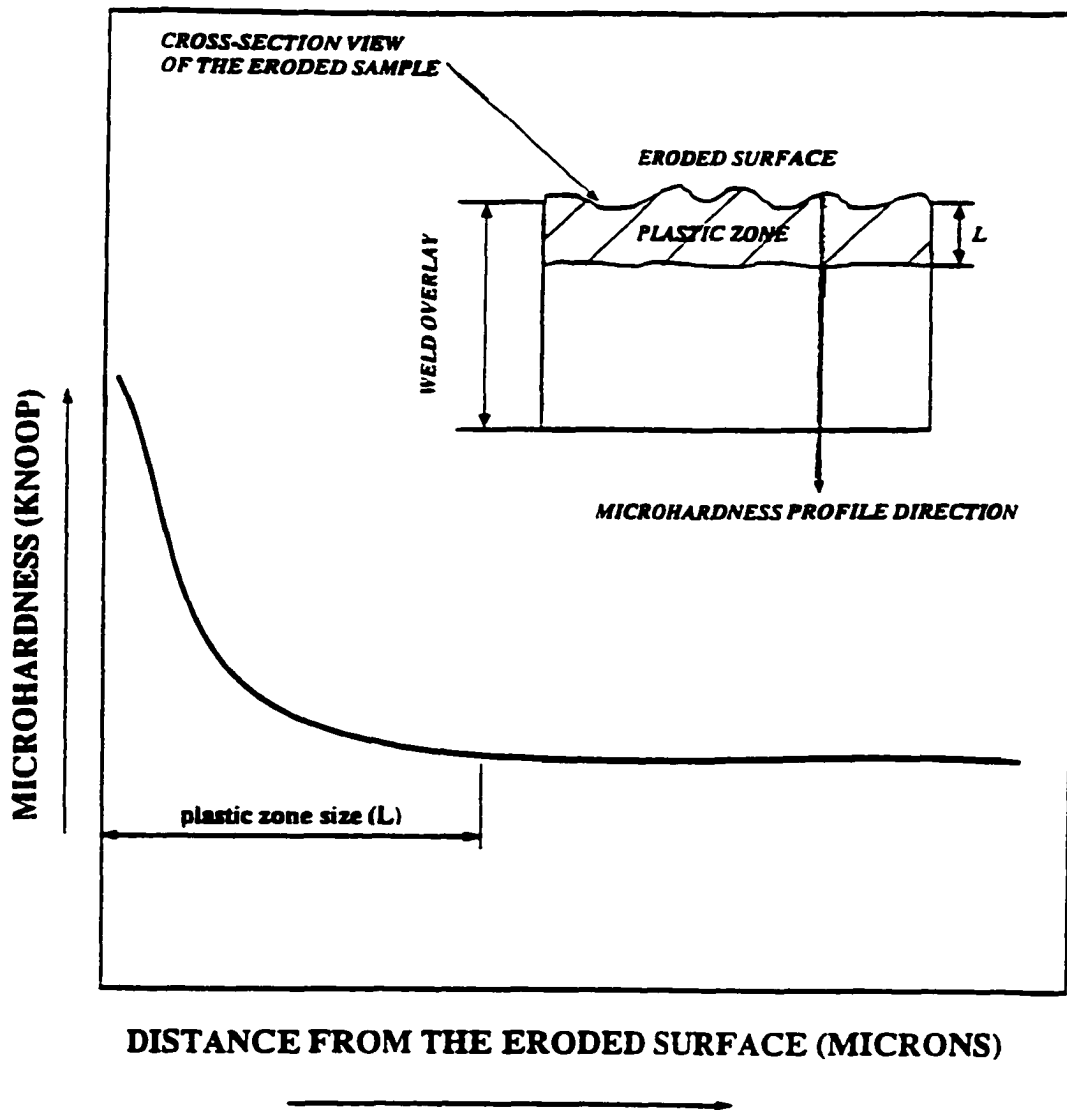


**Figure 16.** Schematic diagram of the microhardness profile that was taken in order to estimate plastic zone size due to erosion.

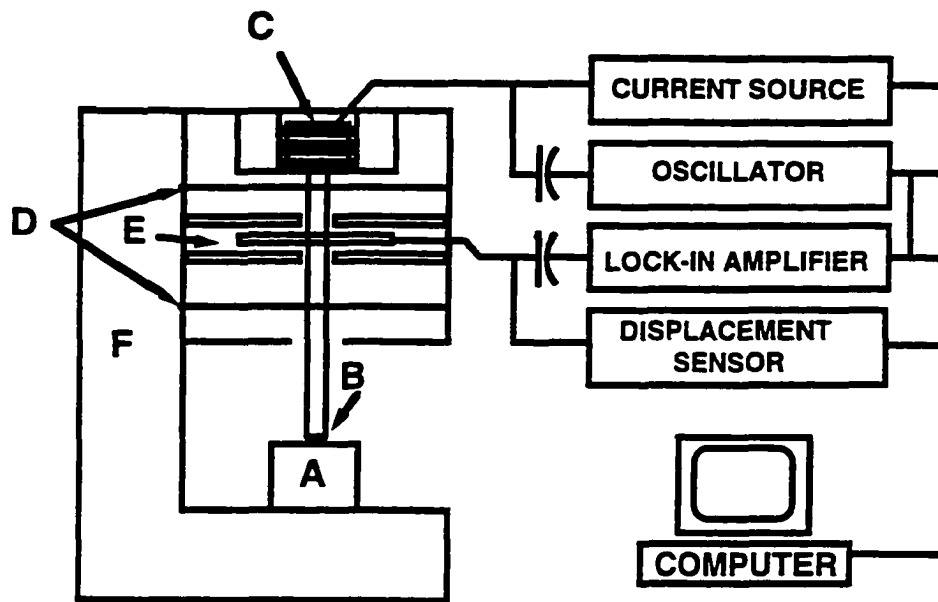


**Figure 17.** Schematic diagram of the Nano Indenter<sup>®</sup> II. A-sample; B-indenter column; C-load applications coil; D-indenter support springs; E-capacitive displacement gauge; and F-load frame.

provided an understanding of the energy absorption properties of the eroded materials.

#### Load-displacement measurements

A schematic diagram of the typical load-displacement curve that can be obtained by using the nanoindentation technique is shown in **Figure 18**. As the load,  $P$ , increases, displacement,  $\delta$ , occurs due to both elastic and plastic deformation of the material (loading curve). After the load is removed, the elastic displacement is recovered (unloading curve). Thus, because of the plastic deformation, a material exhibits contact hysteresis, i.e., some amount of energy that was transferred into the material during the loading cycle is absorbed through plastic deformation. The shaded area in **Figure 18** represents this plastic deformation energy.

Indentation tests were conducted with a 50  $\mu\text{m}$  radius diamond ball and a peak load of 80 mN on the cross-sections of all materials exposed to erosion. For each indentation a load-displacement curve was generated. The loading/unloading rate of 2 mN/sec and 20 seconds holding time at the peak load were used during the load-hold-unload cycle. Indents started at 10  $\mu\text{m}$  from the eroded surface and proceeded into the material with 25  $\mu\text{m}$  steps. Therefore, a series of load-displacement diagrams with distance from the eroded surface was produced for each material. Since the area under the load displacement curve represents the energy that materials absorb during the indentation process, a profile of the eroded material's ability to absorb this energy within the plastically deformed region was obtained. Four profiles (five indents in each profile) were obtained in different locations of each material in order to improve the statistical significance of the data.

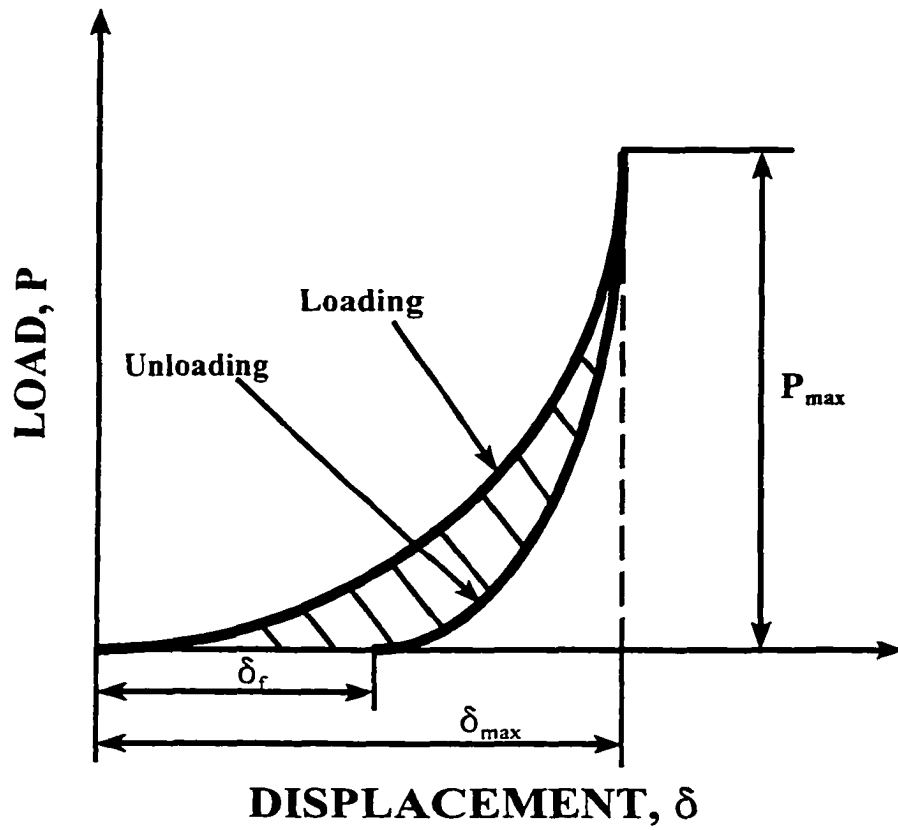


**Figure 18.** Schematic diagram of the typical load-displacement curve obtained during the nanoindentation test. Shaded area represents plastic deformation energy,  $\delta_f$  is the final indentation depth after indentation, and  $\delta_{\max}$  is the maximum indentation depth at the peak load.

#### IV.C.3. Quasi-static and high strain rate compression tests

Quasi-static and high strain rate compression tests were conducted to determine the effect of mechanical properties such as strength and toughness on erosion resistance of ductile materials. In contrast to the strain rates during the quasi-static tests ( $10^{-3} \text{ sec}^{-1}$ ), the strain rates during the high strain rate compression tests were varied from  $1500 \text{ s}^{-1}$  to  $9600 \text{ s}^{-1}$ . These strain rates are similar to those expected during the erosion process. To estimate strain rates imposed on the target material during particle impact, Hutchings [45] used the following equation:

$$\dot{\epsilon}' \equiv \frac{2^{3/2}}{5\pi} \frac{v^{1/2}}{r} \left( \frac{3P}{2\rho} \right)^{1/4} \quad (12)$$

where  $\dot{\epsilon}'$  is the mean strain rate ( $\text{s}^{-1}$ ),  $v$  is the particle velocity (m/s),  $r$  is the particle radius (m),  $P$  is the dynamic mean contact pressure or hardness of the target material ( $\text{N/m}^2$ ), and  $\rho$  is the particle density ( $\text{kg/m}^3$ ). By using this equation for the experimental conditions and materials used in this study, it was found that the strain rates during erosion could range between  $12\text{-}20 \times 10^4 \text{ s}^{-1}$ .

Compression tests in the quasi-static regime were conducted on a conventional servo-hydraulic test frame, and tests in the high strain rate regime were conducted using a compression split-Hopkinson pressure bar at the University of California at San Diego. Compression specimens were machined from each material as right, regular cylinders having a diameter of 5.08 mm and height of 5.08 mm. Detailed discussion of classical Hopkinson bar techniques [51] and recent experimental modifications [52] can be found

in the literature.

The microhardness measurements made on the eroded samples are quasi-static measurements of deformation which was introduced at high strain rate. In order to verify that these microhardness measurements could be correlated to the high strain rate behavior measured from compression samples, an additional set of experiments was conducted. In these experiments, compression samples were first deformed on the Hopkinson bar at high strain rate ( $>2000 \text{ s}^{-1}$ ) to a true strain of approximately 0.2 and were then unloaded. These same samples were then re-machined to right, regular cylinders, and retested in compression under quasi-static conditions to determine the reload yield strength. If the reload yield strength measured under quasi-static conditions was the same as the flow stress level at the end of the high-strain rate compression test, then it could be assumed that the microhardness measurements taken from the eroded samples reflect the flow stress level introduced by the high-strain rate deformation of the erosion process.

Finally, high strain rate compression samples were sectioned, polished, and tested using the microhardness and nanoindentation techniques to develop a correlation between flow stress in compression samples and microhardness in the eroded samples. This flow stress/microhardness correlation was then used to infer the strength and strain of the material below the eroded surface based on their microhardness readings.

## V. RESULTS AND DISCUSSION

### V.A. EROSION TESTS AND PLASTIC DEFORMATION DURING EROSION.

Volume loss versus time plot for all alloys tested at a particle velocity of 40 m/s and  $90^0$  impact angle are presented in **Figure 19**. The relative ranking of all alloys based on their volumetric erosion rates is listed in **Table III**. The Inconel-625 alloy showed the lowest erosion rate of  $0.0074 \text{ mm}^3/\text{min}$  while Cu exhibited the highest erosion rate of  $0.0104 \text{ mm}^3/\text{min}$ .

Results of the microhardness tests on cross-sectioned samples are shown in **Figure 20**. These results demonstrate that for all materials, the hardness significantly increased near the eroded surface. An increase in hardness indicates that the material beneath the eroded surface experienced plastic deformation and therefore, erosion resistance should be related to the ability of a material to *absorb* impact energy. The estimated plastic zone depth for all materials are listed in **Table IV**. It can be seen that Cu has the largest plastic zone of  $140 \text{ }\mu\text{m}$ , while Ultimet and B3 alloys have the smallest plastic zone of  $40 \text{ }\mu\text{m}$ . Mechanical properties such as hardness and toughness affect the ability of the material to deform plastically and may control its erosion resistance.

### V.B. EROSION MODEL FOR DUCTILE MATERIALS. EFFECT OF MECHANICAL PROPERTIES ON ENERGY DISSIPATION DURING EROSION.

To consider the effect of the target material mechanical properties on erosion resistance, the following assumptions can be made to simplify the energy balance

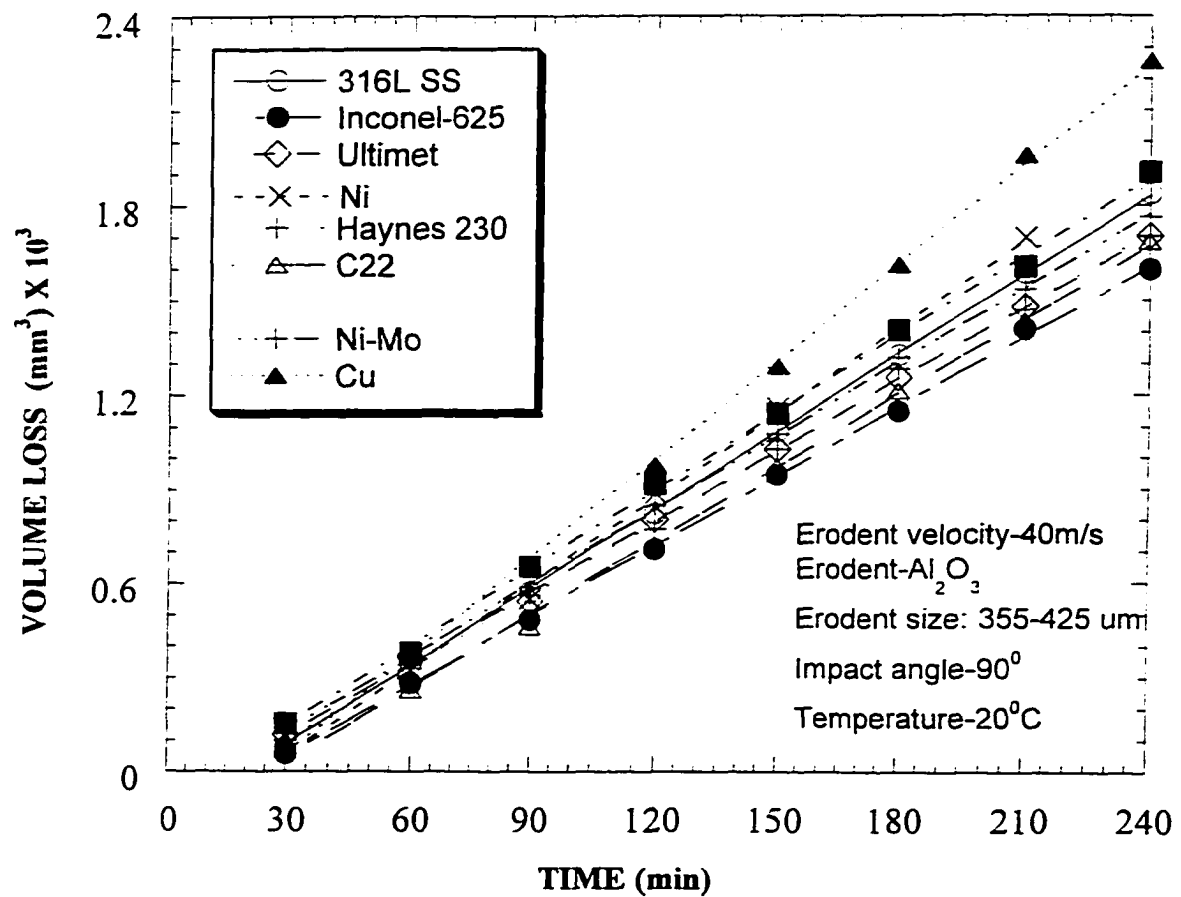


**Figure 19.** Volume loss versus erosion time plots for all materials tested. The slope of each line represents steady-state erosion rate.



**Table III.** Volumetric erosion rates for tested alloys at 90<sup>0</sup> particle impact angle and velocity of 40m/s.

<b>ALLOY</b>	<b>Volumetric erosion rate (mm<sup>3</sup>/min) *10<sup>3</sup></b>
Inconel-625	7.40±0.07
Ultimet	7.54±0.08
Haynes 230	7.67±0.08
Hastelloy-C22	7.80±0.12
B3	7.80±0.07
316L SS	8.30±0.05
Nickel	9.10±0.15
Copper	10.4±0.13

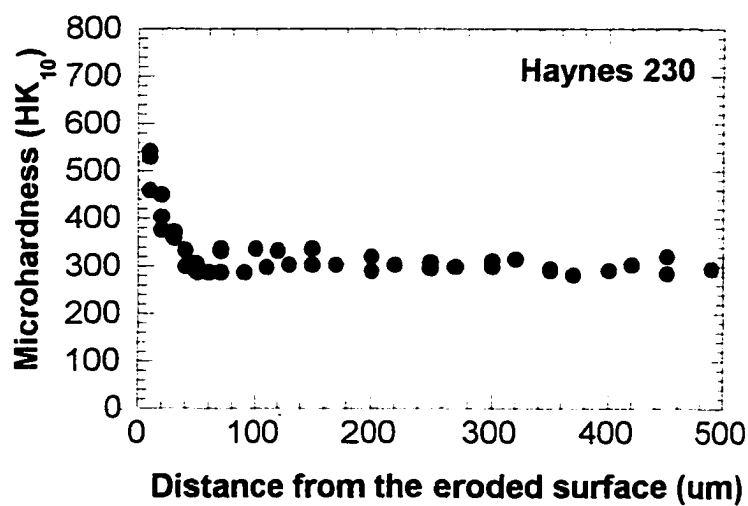
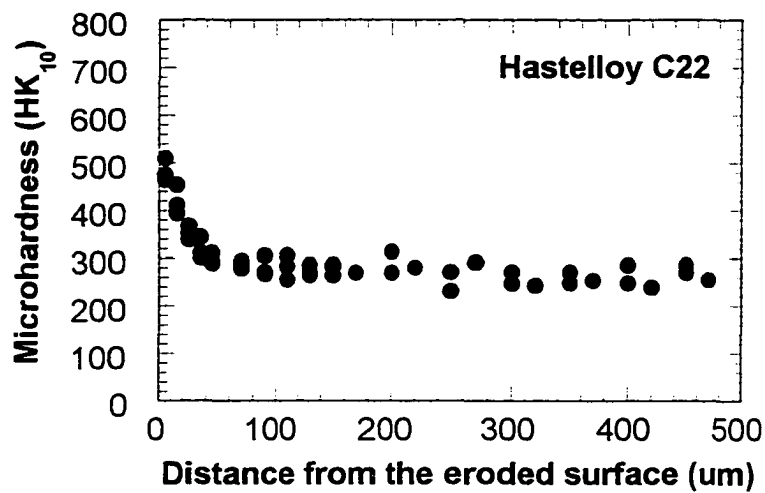
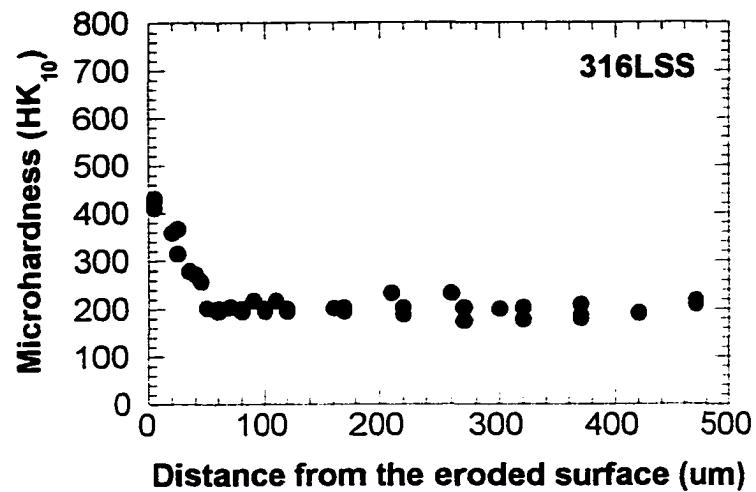


**Figure 20 (a-h).** Microhardness profiles obtained on the cross-sections of the eroded samples after the longest exposure time (240 min).  $90^0$  particle impact angle and 40m/s velocity.

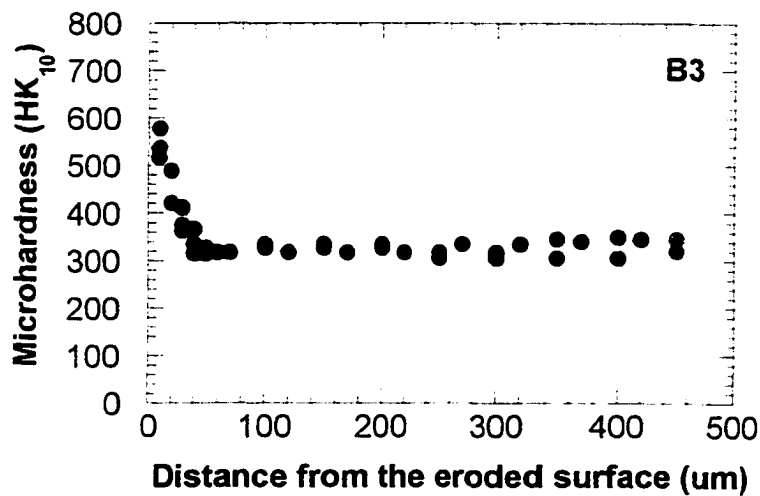
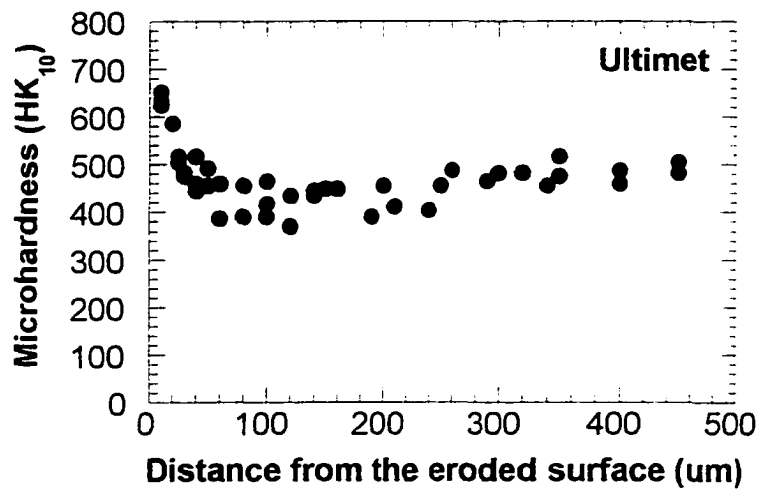
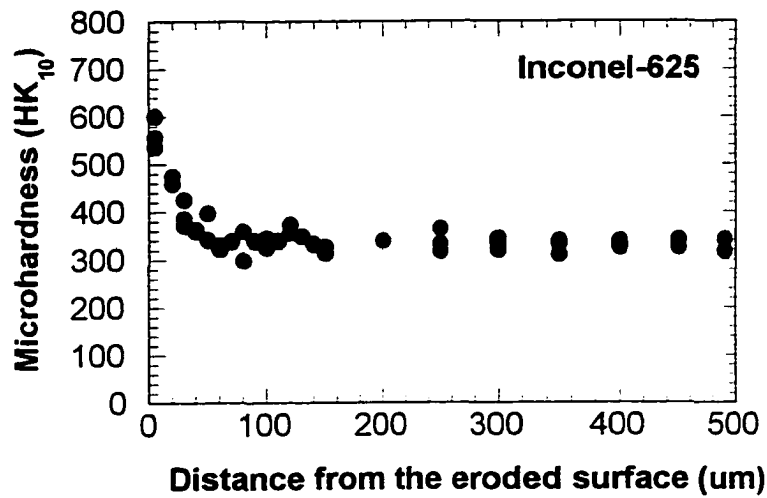
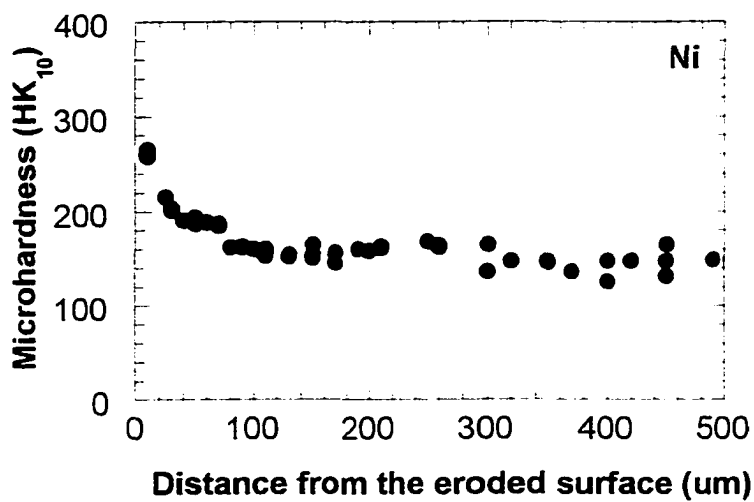
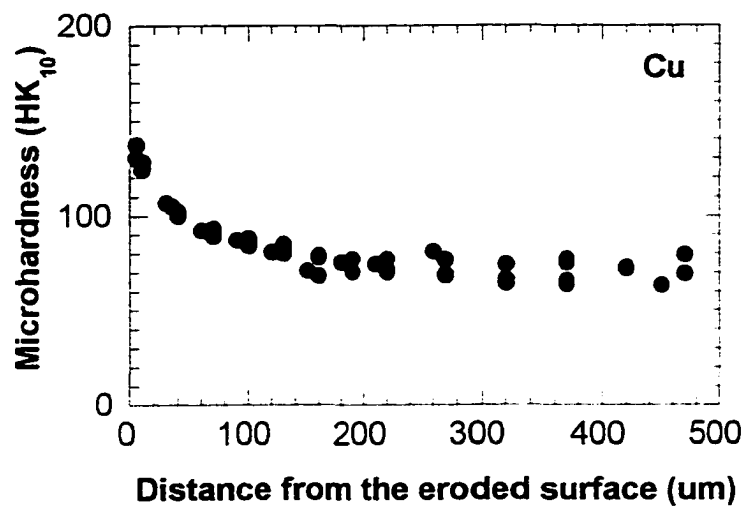


Figure 20 (cont.)



**Figure 20 (cont.)**

**Table IV.** Plastic zone depth due to erosion. Depth was estimated using microhardness technique.

Material	Plastic zone depth ( $\mu\text{m}$ )
Cu	140
Ni	80
316L SS	60
Inconel-625	50
Hastelloy-C22	50
Haynes 230	50
B3	40
Ultimet	40

between an impacting particle and the target material: 1) the erodent particle is spherical and does not break upon impact, and 2) the temperature rise in the target during impact is not significant enough to cause changes in its mechanical properties. The latter assumption appears to be reasonable for the erosion process due to the small size of the impacting particles and the comparatively large size of the target specimens. Therefore, the amount of energy converted to heat is insignificant to cause changes in mechanical properties of the target material.

#### ***V.B.1. Plastic deformation energy***

From the first principles, the kinetic energy of the particle before the impact is given by:

$$KE = \frac{mV_i^2}{2} = KE_{pd} + KE_{ed} \quad (13)$$

where  $m$  is the mass of the particle,  $V_i$  is initial velocity,  $KE_{pd}$  and  $KE_{ed}$  are the plastic and elastic deformation energies, respectively. However, the portion of this energy *transferred* or delivered into the target material depends upon the mechanical properties of the target and erodent such as surface hardness, elastic modulus, etc. Upon impact, the kinetic energy of the particle transfers into (1) rebound of the particle ( $KE_{ed}$ ) and (2) plastic deformation of the target ( $KE_{pd}$ ). The portion of the initial kinetic energy used for plastic deformation is equal to:

$$KE_{pd} = \frac{mV_i^2}{2} - \frac{mV_r^2}{2} = \frac{mV_i^2}{2} * \left[ 1 - \left( \frac{V_r}{V_i} \right)^2 \right] = \frac{mV_i^2}{2} * [1 - e^2] \quad (14)$$

where  $V_r$  is the rebound velocity of the particle. The term  $V_r/V_i$ , referred to as the coefficient of restitution ( $e$ ), represents the stored elastic energy in the particle and the target material after the impact [28]. For example, if the coefficient of restitution is high (i.e., the rebound velocity is close to the incident velocity), the energy transferred to elastic deformation of the target would also be high and therefore, the target material would not experience significant plastic deformation. The coefficient of restitution depends on the mechanical properties of the particle and target materials (i.e., hardness and elastic modulus).

According to Lankov [28] and Johnson [53], for spherical particles the coefficient of restitution ( $e$ ) can be expressed as a function of hardness and elastic modulus:

$$e = \left( \frac{V_r}{V_i} \right) = \frac{1.75 * H^{0.625} * J^{0.5}}{\rho_p^{0.125} * V_i^{0.25}} \quad (15)$$

$$\text{or} \quad e^2 = \left( \frac{V_r}{V_i} \right)^2 = \frac{3.06 * H^{1.25} * J}{\rho_p^{0.25} * V_i^{0.5}} \quad (16)$$

where  $\rho_p$  is the density of the impacting spherical particle in  $\text{kg/m}^3$ ,  $H$  is the target material hardness in  $\text{N/m}^2$ ,  $V_i$  is the initial particle velocity in  $\text{m/s}$ , and  $J$  is a parameter related to the elastic modulus and Poisson coefficients of the target and particle materials.

$J$  is given by:

$$J = \frac{(1 - \mu_t^2)}{E_t} + \frac{(1 - \mu_p^2)}{E_p} \quad (17)$$

where  $\mu_t$  and  $\mu_p$  are the Poisson coefficients of the target and particle materials respectively, and  $E_t$  and  $E_p$  are the elastic moduli of the target and particle materials, respectively in  $\text{N/m}^2$ . Substitution of the equation 17 into 16 gives:

$$e^2 = \left( \frac{3.06 * H^{1.25}}{\rho_p^{0.25} * V_i^{0.5}} \right) * \left[ \frac{(1 - \mu_t^2)}{E_t} + \frac{(1 - \mu_p^2)}{E_p} \right] \quad (18)$$

Therefore Equation 14 can be rewritten as:

$$KE_{pd} = \frac{mV^2}{2} * \left[ 1 - \left( \frac{3.06 * H^{1.25}}{\rho_p^{0.25} * V_i^{0.5}} \right) * \left( \frac{(1 - \mu_t^2)}{E_t} + \frac{(1 - \mu_p^2)}{E_p} \right) \right] \quad (19)$$

Equation 19 shows that for target material with high hardness to modulus ratio, a larger portion of the incident particle's kinetic energy transforms into rebound kinetic energy when compared to materials with low hardness. Therefore, the energy used for plastic deformation ( $KE_{pd}$ ) during erosion is lower for hard materials than for soft materials.

### ***V.B.2 Erosion parameter***

Bitter [9] suggested that the erosion rate is proportional to the ratio of the input kinetic energy to the energy needed to remove a unit volume of the material. Based on



this concept, the erosion rate of the material is proportional to the ratio of the energy used for plastic deformation,  $KE_{pd}$ , to the energy required to *cause fracture* or the fracture energy. A mechanical property that can represent the fracture energy per unit volume is the tensile toughness or area under the true stress-true strain curve. The volume within which plastic deformation is absorbed during erosion is defined by the plastic zone size. Now, the expression for the erosion parameter, can be written as follows:

$$E_{parameter} = \frac{mV^2}{2} * \left[ \frac{1 - \left( \frac{3.06 * H^{1.25}}{\rho_p^{0.25} * V_i^{0.5}} \right) * \left( \frac{(1-\mu_t^2)}{E_t} + \frac{(1-\mu_p^2)}{E_p} \right)}{T * L} \right] \quad (20)$$

where  $E_{parameter}$  is an erosion parameter, T is the tensile toughness of a material in Joules/m<sup>3</sup> and L is the plastic zone volume in m<sup>3</sup>. All the terms in equation 20 are summarized in **Table V**.

The developed erosion parameter represents a comprehensive model that includes mechanical properties of the target materials as well as properties of the erodent. In addition, Equation 20 shows that, for the same erosion conditions (i.e., erodent velocity and density are constant), the  $E_{parameter}$  is low for materials that combine high hardness to modulus ratio and high tensile toughness. To evaluate the validity of Equation 20, the tensile toughness of materials during erosion was estimated from the high-strain-rate

**Table V.** Summary of the terms included in the erosion model (equation 20).

<b>Term</b>	<b>Definition</b>	<b>Units</b>
$E_{\text{parameter}}$	erosion parameter	--
$m$	mass of the impacting particles	kg
$V_i$	initial particle velocity	m/s
$H$	target material hardness	$\text{N/m}^2$
$\rho$	density of the impacting spherical particle	$\text{kg/m}^3$
$\mu_p$	Poisson coefficient of the particle material	--
$\mu_t$	Poisson coefficient of the target material	--
$E_p$	elastic modulus of the particle material	$\text{N/m}^2$
$E_t$	elastic modulus of the target material	$\text{N/m}^2$
$T$	Toughness	$\text{Joules/m}^3$
$L$	plastic zone volume	$\text{m}^3$

compression tests. In addition, the maximum hardness measured beneath the eroded surface was substituted for  $H$  in Equation 20. Plastic zone volume ( $L$ ) was estimated from the surface area of the eroded samples (constant for all materials  $\approx 9 \times 10^{-5} \text{ m}^2$ ) and the depth of plastic deformation beneath the eroded surface as determined by microhardness measurements. The procedure for estimating the mechanical properties during erosion is presented below. It is worth noting here that if it were possible to directly measure the coefficient of restitution of the impacting particles, then it would be possible to use Equation 20 directly for determining the erosion parameter. However, direct measurement of the coefficient of restitution for very small particles presents a considerable experimental challenge.

### ***V.B.3 Mechanical properties during erosion***

The determination of the toughness of a material under the high-strain conditions associated with the erosion process is necessary to determine the erosion parameter calculated from Equation 20. Recall, toughness can be calculated by using equation 6 as shown below:

$$T = K * \frac{\varepsilon_f^{n+1}}{n+1} \quad (6)$$

where  $K$  is the strength coefficient,  $n$  is the strain hardening coefficient, and  $\varepsilon_f$  is the failure strain. To estimate toughness during erosion, *high strain-rate* compression stress-strain curves must be generated to determine strength and strain hardening coefficients. However, compression tests do not cause failure of the material and this prevents

determination of the failure strain. Consequently, a method was developed to determine failure strain and toughness of the material by using high-strain-rate compression tests and microhardness tests. To estimate the tensile toughness ( $T$ ) associated with the erosion process, the following procedure was utilized: 1) compression stress-strain curves at strain rates comparable to those during erosion were generated using the compression Hopkinson bar; 2) the failure stress at the eroded surface was estimated from microhardness measurements of the eroded samples; 3) the failure strain was inferred from the failure stress and compressive stress-strain curves; and 4) tensile toughness was found by integration of the compression stress-strain curves over the strain range from zero to failure strain.

#### High-strain-rate compression tests

Strain rates during solid particle erosion are different from those during quasi-static mechanical tests. Depending on the erosion conditions (i.e., erodent velocity, target temperature and erodent size), strain rates in target materials may range between  $10^3$  and  $10^7 \text{ s}^{-1}$ . In contrast, quasi-static tests are conducted using strain rates between  $10^{-4}$  and  $10^{-1} \text{ s}^{-1}$ . Clearly, for strain-rate sensitive materials, *high-strain-rate* mechanical tests are necessary to develop accurate correlation between mechanical properties and erosion resistance.

In this study, high-strain-rate compression tests were conducted at strain rates of

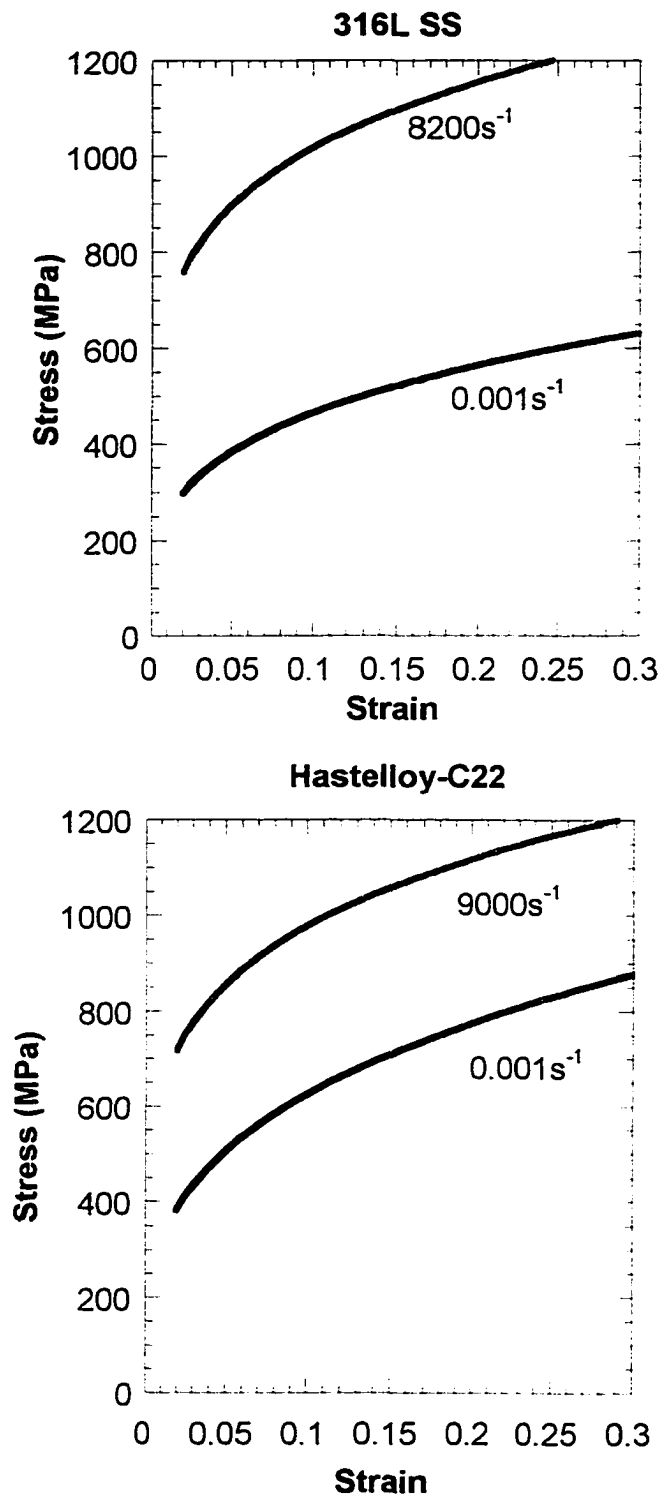


**Figure 21 (a-h).** Stress-strain curves generated for each material over a range of strain rates. For each material, high strain-rate has a pronounced influence on the yield and flow stress of the material.

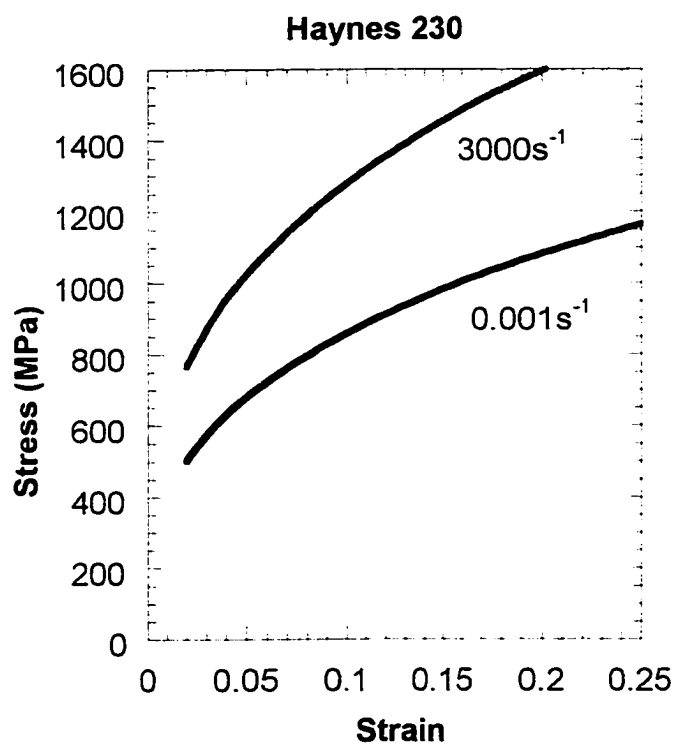
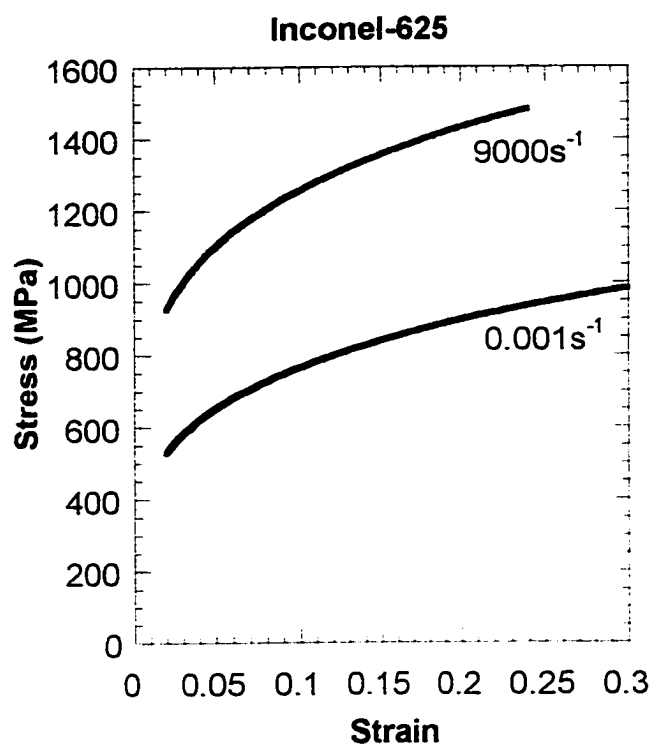


**Figure 21 (cont.)**

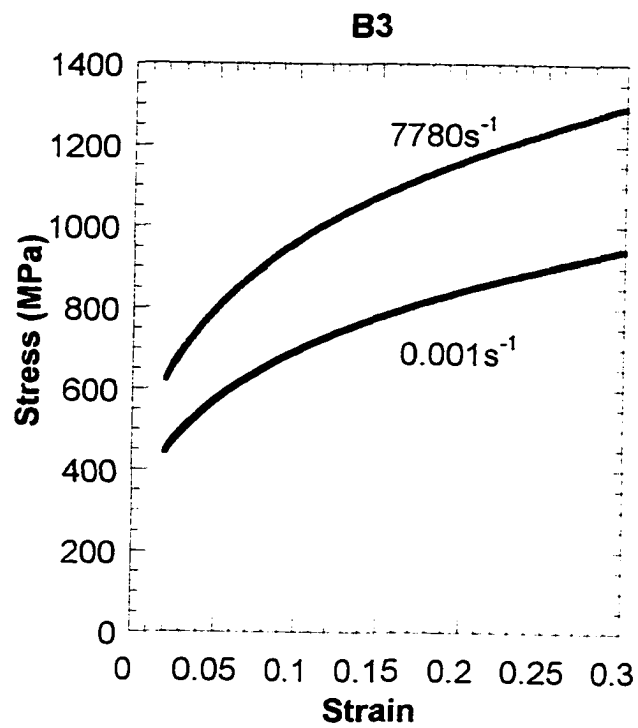


**Figure 21 (cont.)**

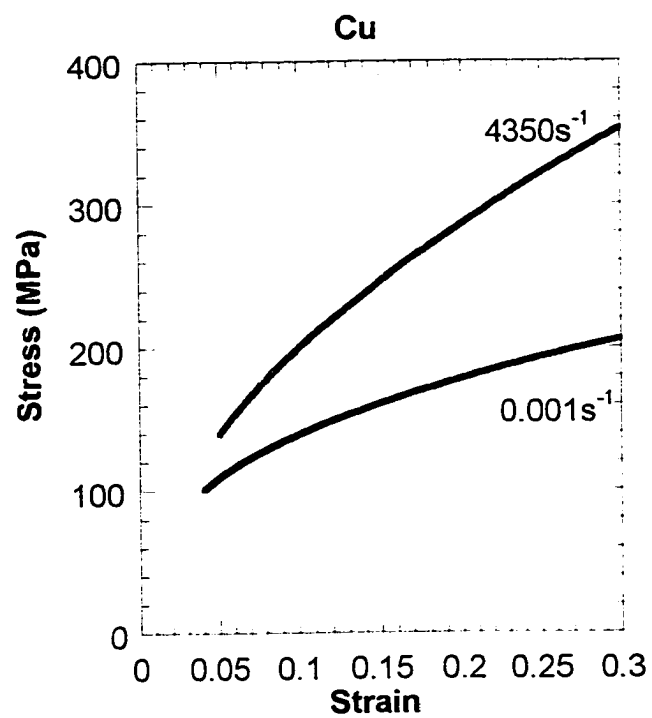


**Figure 21 (cont.)**



$\approx 10^3 - 10^4 \text{ s}^{-1}$ . These strain rates are similar to those calculated by Hutchings [45] using equation 12 for particle impacts at 40 m/s. Therefore, mechanical properties measured from the high-strain-rate tests could be used as an estimate of the mechanical properties during erosion. **Figure 21** shows stress-strain curves generated for each material over a range of strain rates. For each material, strain-rate has a pronounced influence on the yield and flow stress of the materials. In some of the materials, the flow stress at high strain rates may be more than twice that associated with quasi-static conditions. The difference in tensile toughness for each material is therefore very dependent on the strain-rate associated with the erosion process.

**Figure 22** shows the stress-strain curves for Ultimet, Inconel-625, Hastelloy-C22, and 316L SS alloys which had been first tested at high strain rate at room temperature, then reloaded at low strain rate to determine if a quasi-static test (such as the hardness tests) conducted following a high strain rate experiment, accurately predicts the flow stress level achieved during the previous high-strain rate tests. Since the quasi-static reload yield point is close to the flow stress at the end of the high strain rate test, it is reasonable to assume that the hardness measurements of the erosion samples accurately reflect the flow stress levels achieved during erosion. The slightly lower quasi-static reload stress level arises due to recovery following the high-strain-rate test as a result of adiabatic heating associated with the dynamic deformation. The lower reload stress is present even if the sample is reloaded dynamically.

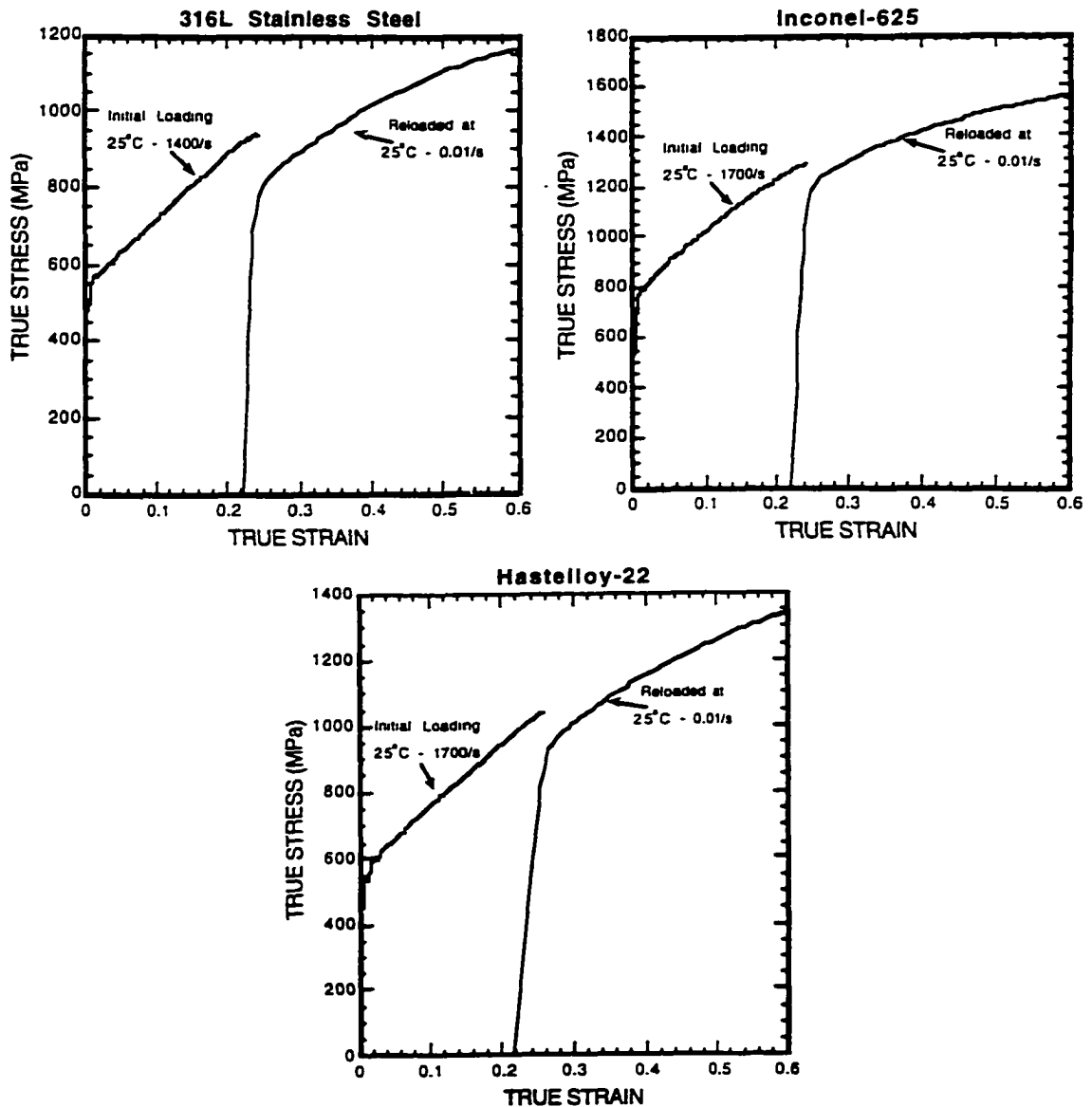


**Figure 22 (a-d).** Stress-strain curves of several of the materials which were first tested at high strain rate at room temperature, then reloaded at low strain rate to determine if a quasi-static test (such as the hardness tests) conducted following a high strain rate experiment, reasonably predicts the flow stress level achieved during the previous high-strain-rate tests.

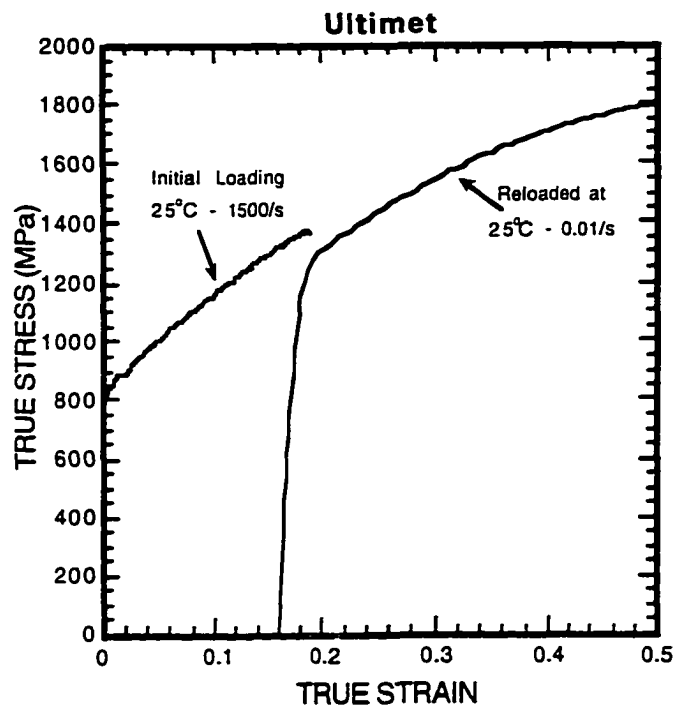


**Figure 22 (cont.)**

### Estimation of tensile toughness during erosion

For eroded materials, the failure strength can be estimated from the microhardness profiles beneath the eroded surface. During particle impact, when the yield strength of the material is locally exceeded, plastic deformation takes place in the vicinity of the impact. After multiple impacts, the yield strength of the material near the surface increases due to strain-rate and strain hardening. Upon further deformation, the yield strength approaches its fracture strength and materials cannot tolerate any further plastic deformation. At this point, the surface becomes brittle and its fragments are removed by subsequent impacts. Thus, the hardness of the material at the eroded surface may be used as a measure of its fracture strength, written as [54]:

$$H = A\sigma_f \quad (21)$$

where  $H$  is the hardness,  $\sigma_f$  is the fracture strength, and  $A$  is a constant which can be experimentally determined from microhardness measurements conducted on compression samples.

To estimate failure strength during erosion, 10g Knoop microhardness tests were conducted on both high-strain-rate compression samples and cross-sections of the eroded alloys. Using known stress values from the high-strain-rate compression curves and corresponding hardness values, the constant  $A$  was determined using Equation 21. Subsequently, the constant  $A$  was used to calculate the erosion failure strength from the microhardness measurements near the eroded surface (5-10  $\mu\text{m}$  from the surface).

Results of the hardness-stress conversion are shown in **Table VI**. Once the erosion fracture strength was determined, fracture strain and toughness were found from the high-strain-rate compression stress-strain curves. Toughness was found by integrating the stress-strain relationship between 0.02 strain (yielding) and failure strain. A schematic illustration of this procedure is shown in **Figure 23**. Estimated failure strength, failure strain, and tensile toughness values during erosion are listed in **Table VII**.

***V.B.4. Erosion model correlation. Effect of mechanical properties on erosion resistance.***

In this study, the erosion test conditions were the same for all materials ( $V_i = 40$  m/s,  $E_p = 400 \cdot 10^9$  N/m<sup>2</sup>,  $\mu_p = 0.21$ ,  $\mu_t = 0.35$ , and  $\rho_p = 4000$  kg/m<sup>3</sup>). Also, all tested alloys have similar elastic moduli values ( $E_t = 210 \cdot 10^9$  N/m<sup>2</sup>) with the exception of copper ( $E_t = 130 \cdot 10^9$  N/m<sup>2</sup>). Thus, tensile toughness (T), maximum hardness near the eroded surface (H), and plastic zone volume (L) values can be used to examine the validity of Equation 20 for the erosion parameter and determine the combined effects of hardness and toughness on erosion resistance. The calculated erosion parameter,  $E_{\text{parameter}}$ , from Equation 20 is plotted against experimentally determined volumetric erosion rates in **Figure 24**. It can be seen that a decrease in values of the erosion parameter leads to a decrease in erosion rates. Thus, materials combining high hardness and high toughness at high strain offer good erosion resistance. Hardness is necessary to reduce the energy transferred from the incident particle into the material while toughness

indicates the ability of the material to absorb this energy without fracture. However, high hardness may reduce the ability of the material to deform plastically and therefore, its toughness may decrease. According to equation 20, the optimum combination of these properties that provides the minimum value of  $E_{\text{parameter}}$  provides the best erosion resistance.

If a ductile material is not strain rate sensitive, its quasi-static mechanical properties can be related with erosion resistance. However, for most ductile materials, mechanical properties at high strain rates are different from the quasi-static properties. Since solid particle erosion involves high-strain-rate deformation of the target material, caution must be taken when a relationship between quasi-static mechanical properties and erosion resistance is drawn. Unfortunately, the exact strain rates during erosion are difficult to estimate because of the gradual change in mechanical properties with distance from the eroded surface. However, as was shown here, compression tests at high strain rates can provide a reasonable estimate of the mechanical properties during erosion and can be used to predict erosion behavior of materials.

#### ***V.B.5. Summary of the erosion model for ductile materials.***

Deformation behavior and erosion resistance of ductile Ni, Co, and Fe-base alloys and commercially pure Cu and Ni were analyzed. High-strain-rate mechanical tests along with microhardness tests were used to estimate the mechanical properties of these materials during erosion. Based on the results of this study, the following can be

summarized:

1. An erosion parameter was developed based on considerations of energy loss during erosion that showed good correlation with experimentally measured erosion rates.
2. Materials combining high hardness and tensile toughness at high strain rates showed good erosion resistance. Hardness is necessary to reduce energy transferred from the particle into the material while toughness indicates the ability of the material to absorb this energy without fracture.
3. A procedure for the estimation of the mechanical properties of a material during erosion using high-strain-rate compression tests and microhardness measurements was developed.

**Table VI.** Hardness-Strength conversion ( $H = A \cdot \sigma_f$ )

Material	Strain rate $s^{-1}$	Stress, $\sigma$ , MPa	Hardness, H (10g Knoop), high strain rate sample MPa	Constant, $A=H/\sigma$ (average value)	Hardness at the eroded surface (10g, Knoop) MPa	Failure strength at the eroded surface, MPa
Ultimet	1500 4200 8700	1350 1500 1600	5030±360 <sup>1</sup> 5500±430 6000±360	3.7 3.7 3.7 3.7	6330±200	1710±60
IN-625	1700 4500 9000	1250 1350 1400	4410±530 4580±220 4740±260	3.5 3.4 3.4 3.4	5660±280	1664±82
C22	1700 4500 9000	1050 1100 1160	3840±230 4465±280 4150±240	3.7 4.0 3.7 3.6	4860±230	1314±62
316L SS	1400 4300 8200	900 1000 1150	3410±260 3750±290 3820±260	3.8 3.8 3.6 3.3	4270±100	1186±28
B3	1300 4500 7800	1095 1248 1392	4290±280 4600±270 4930±320	3.6 3.7 3.8 3.9	5560±330	1463±87
Copper	2500 4500	345 350	1250±60 1310±110	3.6 3.7 3.7	1250±50	338±14
Nickel <sup>2</sup>				3.5	2560±150	731±43

<sup>1</sup> Hardness numbers and standard deviations were calculated from at least 10 indentations.

<sup>2</sup> Since in this study no high strain rate tests were performed for nickel, value for constant A was approximated as 3.5 and failure strain and toughness were estimated from the high strain rate stress-strain curves found in the literature [Follansbee, P.S. et al., *Acta metall. mater.*, Vol. 38, n. 7, 1990, pp. 1241-1254]



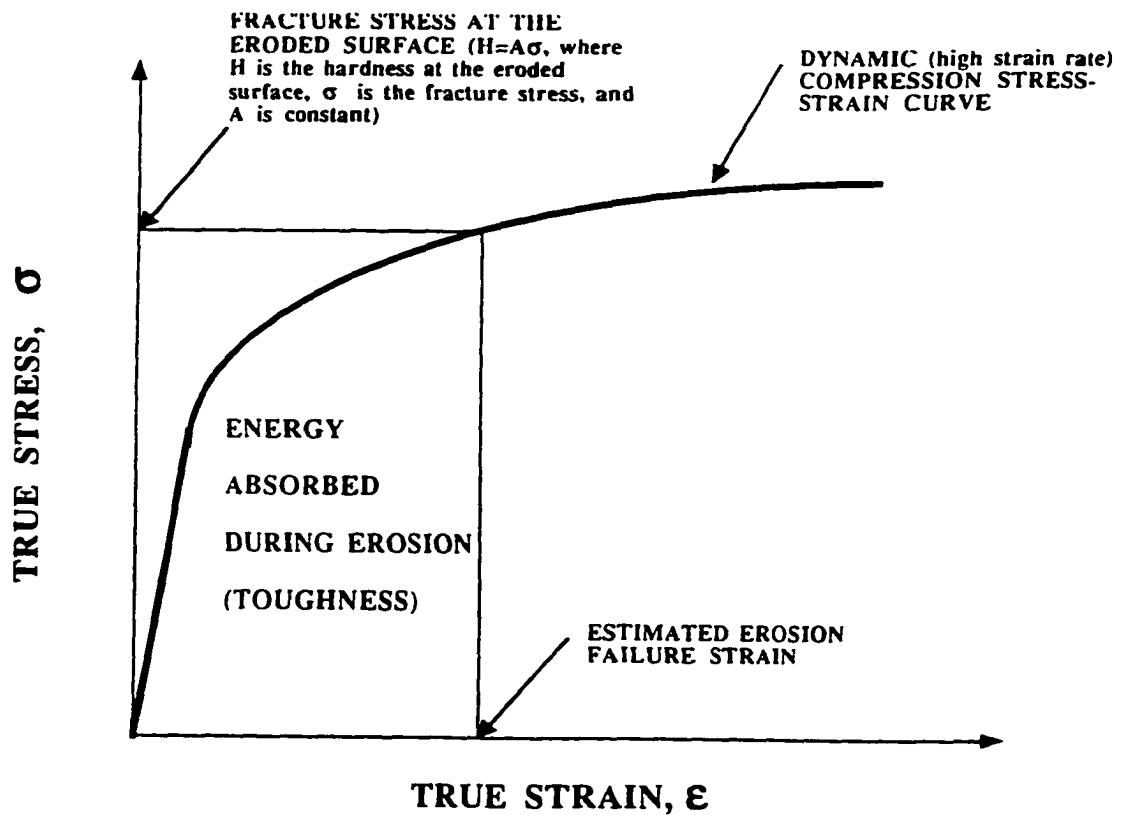


**Figure 23.** Schematic diagram showing procedure that was used to estimate tensile toughness during erosion using high-strain-rate compression and microhardness tests.

**Table VII.** Estimated failure stress, failure strain, and toughness values during erosion.

Alloy	Strain rate, (s <sup>-1</sup> )	Stress-strain relationship <sup>1</sup> $\sigma = \sigma_0 + K\epsilon^n$	Failure strength (MPa), $\sigma_f$	Failure strain, $\epsilon_f$	Toughness (MJ/m <sup>3</sup> )
Ultimet	8700	$804 + 1926\epsilon^{0.55}$	1710±60	0.25±0.02	355±43
IN-625	9000	$830 + 1600\epsilon^{0.6}$	1664±82	0.31±0.05	416±84
C22	9000	$613 + 1200\epsilon^{0.54}$	1314±43	0.35±0.05	370±65
316L SS	8200	$684 + 1208\epsilon^{0.59}$	1186±28	0.22±0.02	220±22
B3	7800	$508 + 1940\epsilon^{0.68}$	1463±87	0.35±0.05	375±70
Copper	4500	$20 + 693\epsilon^{0.6}$	338±14	0.27±0.02	57±5
Nickel <sup>2</sup>	4000	$50 + 1298\epsilon^{0.5}$	731±43	0.32±0.04	158±30

<sup>1</sup>  $\sigma_0$  is the yield strength and K is the strength coefficient.

<sup>2</sup> Stress-strain relationship was obtained from Follansbee, P.S. et al., *Acta metall. mater.*, Vol. 38, n. 7, 1990, pp. 1241-1254.

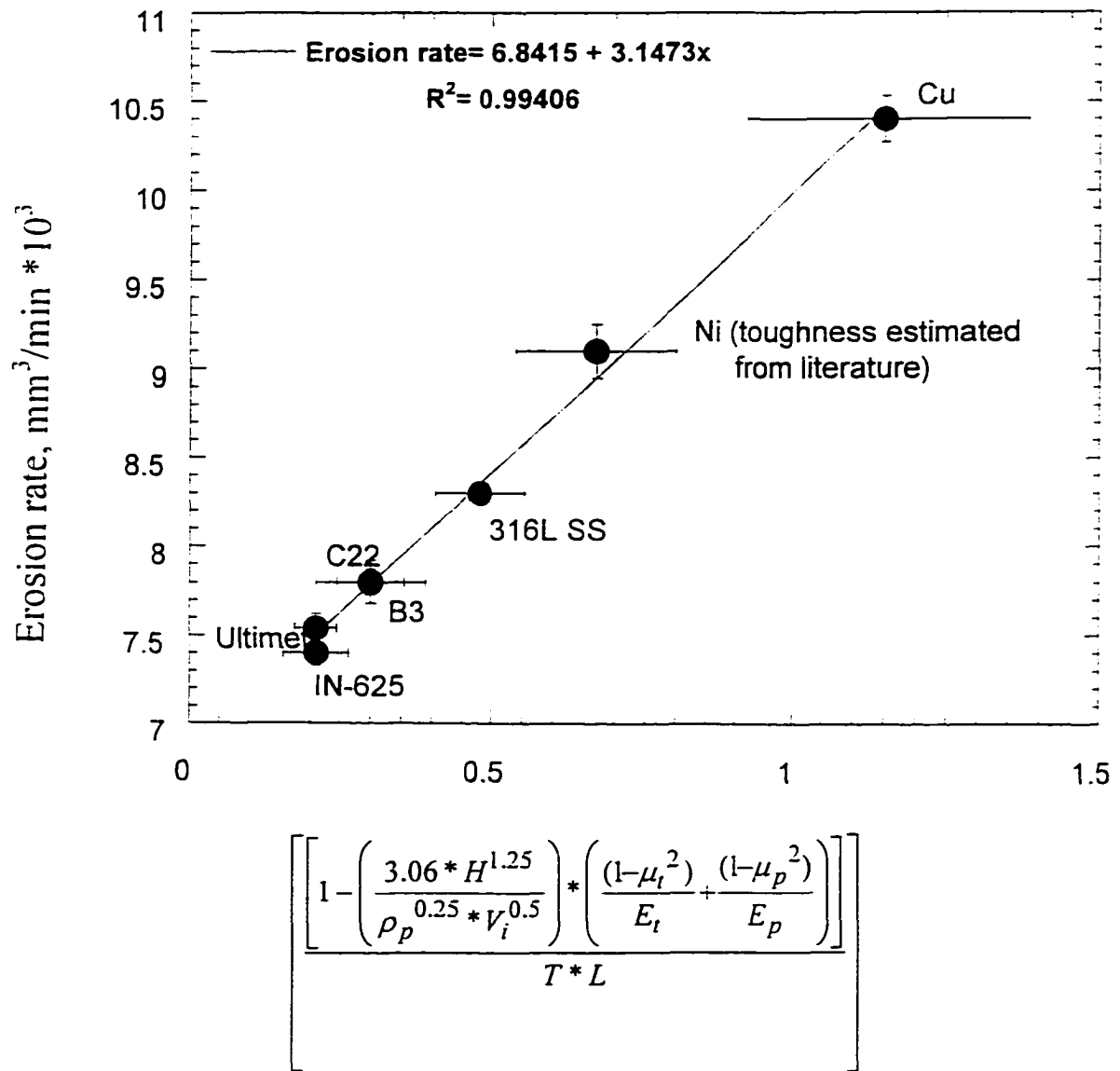


**Figure 24.** Erosion parameter calculated from Equation 20 is plotted against experimentally determined volumetric erosion rate. Good correlation is observed. A decrease in values of erosion parameter lead to a decrease in erosion rate.

## V. C. ANALYSIS OF SUBSURFACE DEFORMATION DURING EROSION BY USING THE NANOINDENTATION TECHNIQUE

### *V.C.1. Theoretical basis for the indentation load-displacement and stress-strain analysis.*

#### Stress-strain analysis

A series of load-displacement diagrams with distance from the eroded surface was produced for each material using Nanoindenter II<sup>®</sup> system with a 50  $\mu\text{m}$  radius spherical indenter. Also, pure tantalum was included for nanoindentation analysis. The main advantage in using a spherical indenter over sharp indenters (i.e. Vickers or Berkovich) is that in spherical indentation, imposed strain is proportional to the indentation size according to [55]:

$$\varepsilon_{pl} \cong \frac{a}{R} \quad (22)$$

where  $\varepsilon_{pl}$  is the plastic strain,  $a$  is the radius of the indentation, and  $R$  is the radius of the indenter. If the indenter penetration depth is small compared with the radius of the indenter, the value of  $a$  can be estimated from the depth of indenter penetration using the following relationship [55]:

$$a = \sqrt{\delta * R} \quad (23)$$

where  $\delta$  is the penetration depth. Also, mean applied pressure or stress values ( $\sigma$ ) can be found from:

$$\sigma = \frac{P}{\pi a^2} \quad (24)$$

where  $P$  is the applied load and  $\pi a^2$  is the projected area of indentation. Therefore, by using equations 22, 23, and 24, the load-displacement diagram,  $P$  vs.  $\delta$ , can be converted into a stress-strain diagram,  $\sigma$  vs.  $a/R$ , which allows an analysis of the strain-hardening behavior of materials. Stress-strain curves of ductile materials can be described by a power law relationship:

$$\sigma = K \left( \frac{a}{R} \right)^n \quad (25)$$

where  $K$  and  $n$  are strength and strain hardening coefficients, respectively. Thus, the use of the small spherical indenter in combination with continuous monitoring of the load-displacement behavior makes it possible to observe changes in strength and strain-hardening behavior with distance from the eroded surface.

#### Elastic recovery analysis

During loading, the work done by the indenter in deforming the material is given by:

$$W = \int_0^{\delta_{\max}} P(\delta) d\delta \quad (26)$$

where  $W$  is work done by indenter,  $P$  is the applied load, and  $\delta$  is the depth of penetration.

The work  $W$  is represented as the area under the loading curve in **Figure 18**. During unloading, the recovered elastic energy ( $W_{elastic}$ ) is given by:

$$W_{elastic} = \int_{\delta_{final}}^{\delta_{\max}} P(\delta) d\delta \quad (27)$$

where  $\delta_{final}$  is the depth of the residual indentation. In **Figure 18**, the elastic energy is represented as the area under the unloading curve. If the indenter is regarded as a free particle, the coefficient of restitution ( $e=V_{rebound}/V$ ) can be found according to [56]:

$$e = \left( \frac{W_{elastic}}{W} \right)^{0.5} \quad (28)$$

$$e^2 = \frac{W_{elastic}}{W} \quad (29)$$

According to equation (14), the particle impact energy that is transferred into plastic deformation equals  $0.5mV^2(1-e^2)$ . Therefore, load-displacement tests and equations 27 and 28 can be used to calculate changes in elastic recovery and restitution coefficient as a function of distance from the eroded surface. Measurement of restitution coefficient is important because its value determines the rebounding ability of the material during erosion. Also, results from the nanoindentation tests can be used (1) to determine the effect of hardness on restitution coefficient of materials and (2) to compare the amount of energy that is transferred into plastic deformation during particle impact.

#### ***V.C.2. Measurements of subsurface elastic recovery and plastic deformation.***

Results of the load-displacement tests conducted on cross-sections of the eroded materials (particle impact angle-90° and velocity-40m/s) are presented in **Figure 25**.

Two observations can be made from the data. First, all materials showed load-unload hysteresis which represents a measure of the amount of energy dissipated into plastic

deformation during indentation. Second, elastic recovery ( $W_{\text{elastic}}/W$ ) was significantly higher near the eroded surface than away from the eroded surface. Subsequently, energy that is dissipated into plastic deformation  $W_{\text{plastic}}$  decreased near the eroded surface and materials became less ductile. **Table VIII** lists the values of  $W_{\text{plastic}}$  and  $W_{\text{elastic}}/W$  or  $e^2$  for all tested materials. Average values of  $e^2$  within the plastic zone were determined using the following equation:

$$\text{average } e^2 = \frac{\int_0^{L_{pl}} e^2(L) dL}{L_{pl}} \quad (30)$$

where  $L_{pl}$  is the plastic zone size due to erosion. **Table VIII** shows that, at 10  $\mu\text{m}$  from the eroded surface, anywhere from 36 to 88% of total energy is elastically recovered during unloading cycle. Tantalum showed the lowest elastic recovery ( $e^2=0.36$ ) while B3 alloy showed the highest elastic recovery ( $e^2=0.88$ ). On average, between 27-72% of total energy is recovered during the unloading cycle. These findings are important because often researchers assumed that during particle impact, only 5-10% of the total energy transfers into elastic recovery (particle rebound) and 90-95% transfers into plastic deformation of the target [40]. Therefore, elastic recovery was largely ignored in energy balance calculations. This research suggests that elastic recovery plays a substantial role in the total energy loss and thus, must be considered in the energy balance calculations.

Latham et al. [57] measured rebound velocity and coefficient of restitution ( $V_{\text{rebound}}/V$ ) of

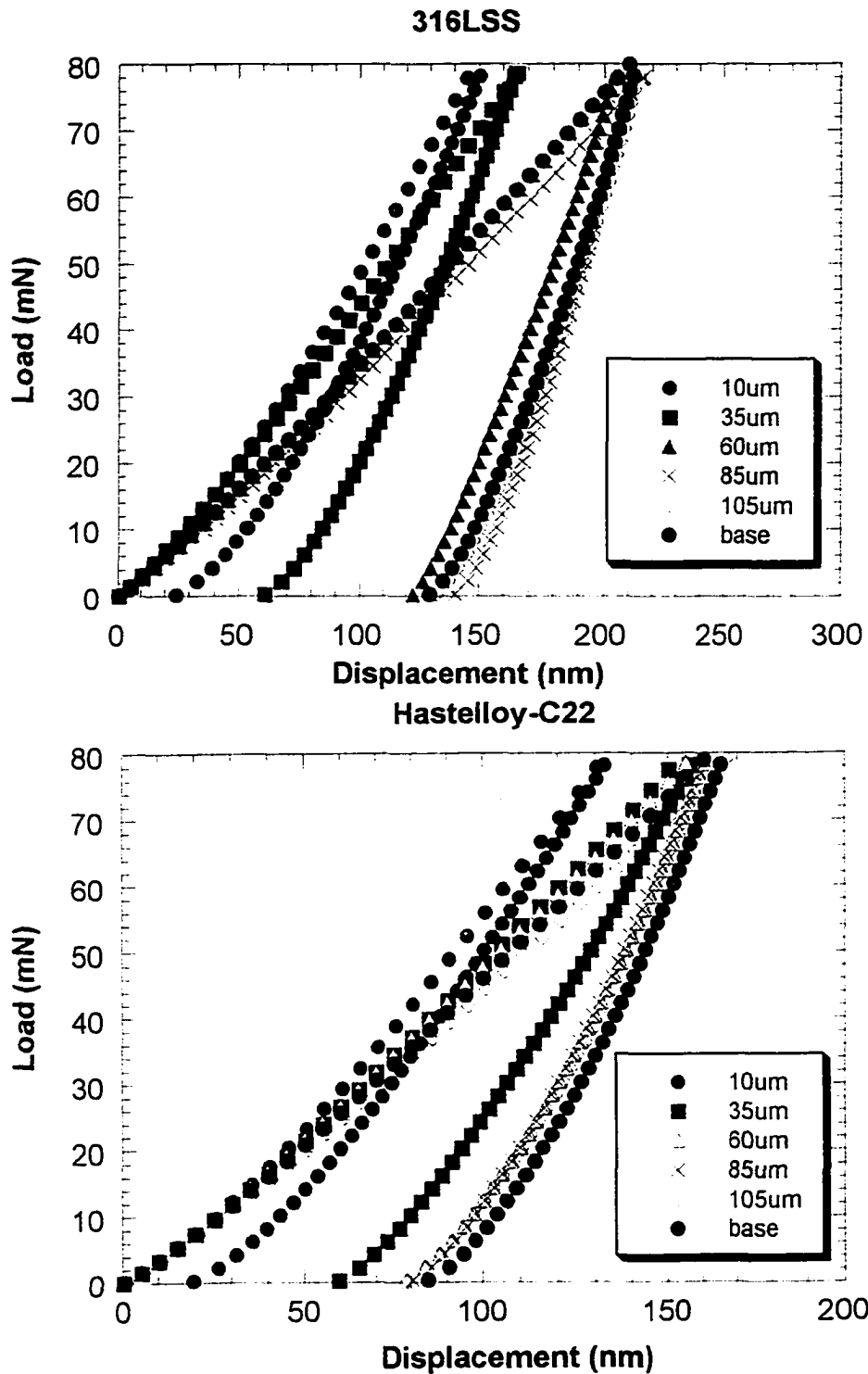


**Figure 25 (a-i).** Indentation load,  $P$ , versus displacement,  $\delta$ , for tested materials as a function of distance from the eroded surface. Measurements were made on the cross-sections of the eroded materials ( $90^\circ$  particle impact angle and velocity of 40 m/s). Note an increase in elastic recovery near the eroded surface.



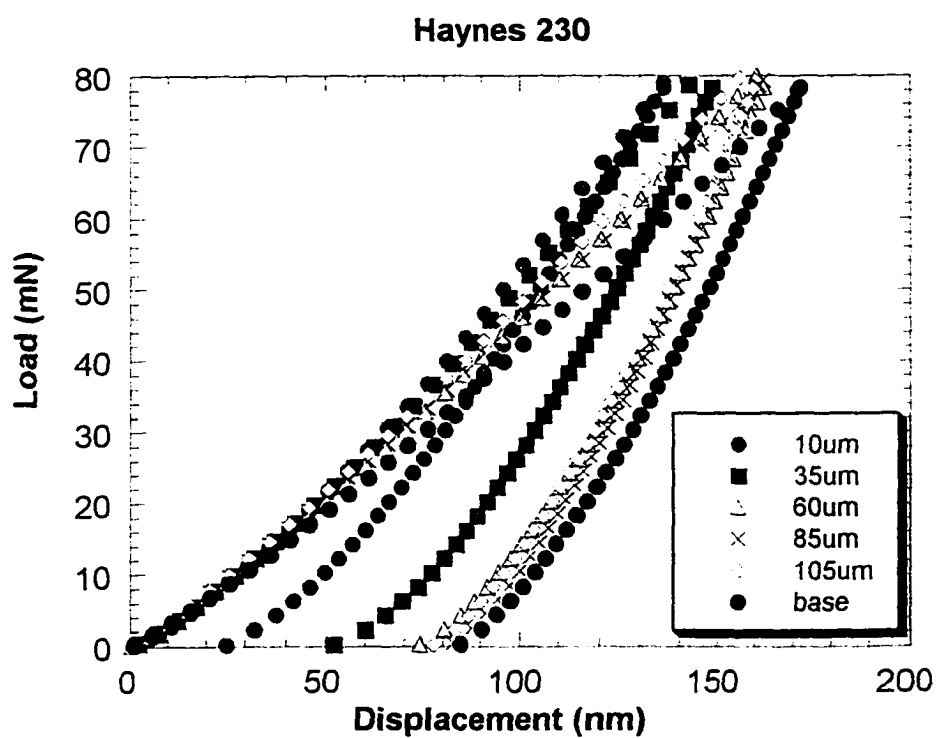
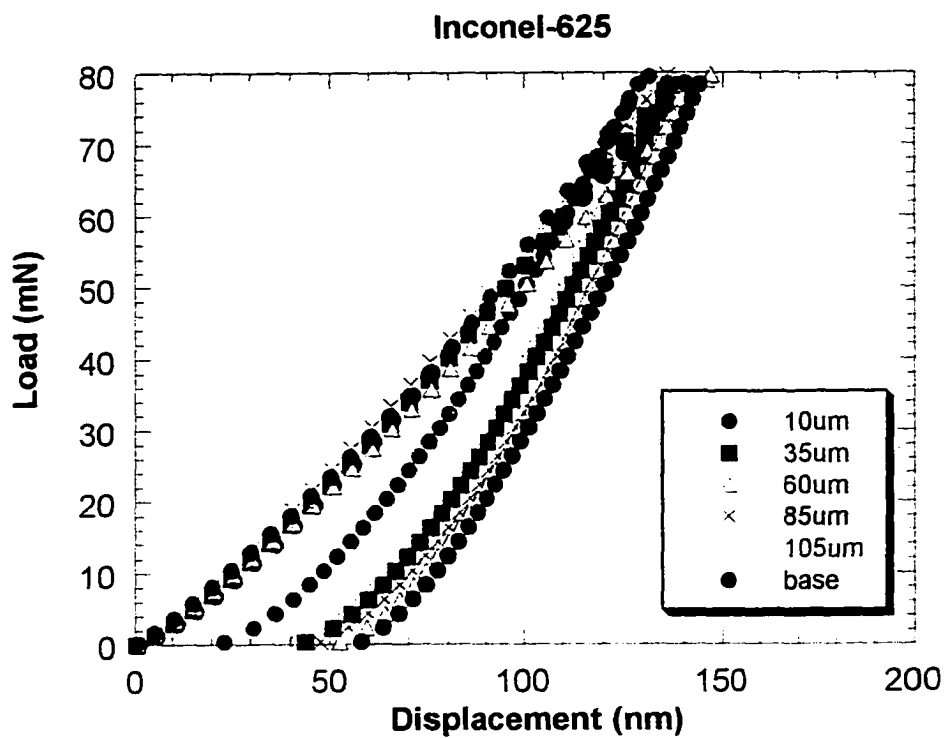


**Figure 25 (cont).**

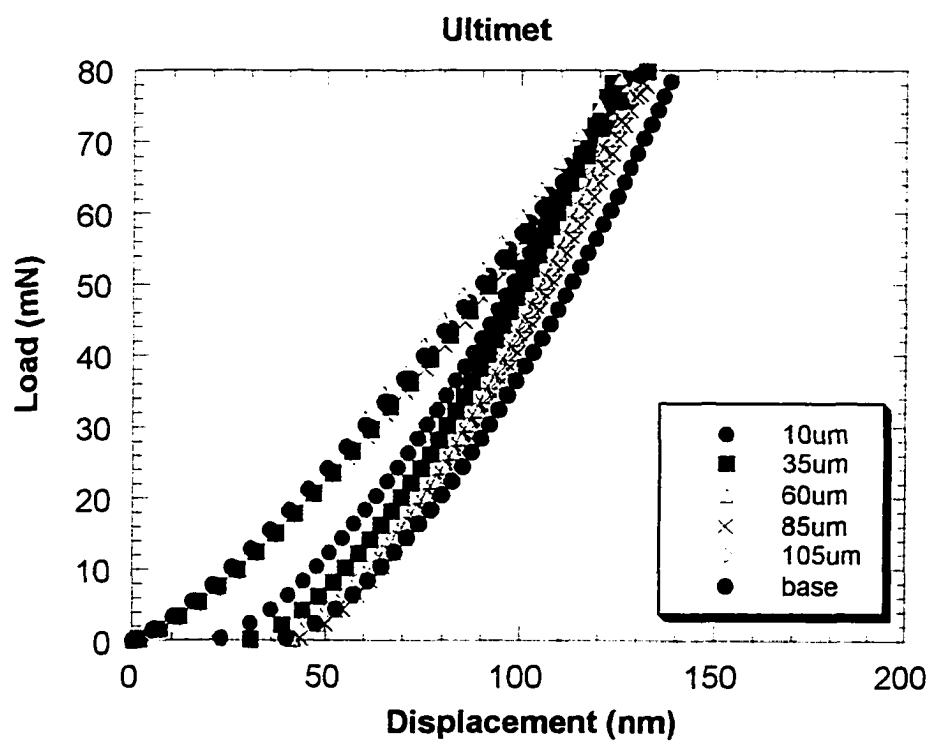
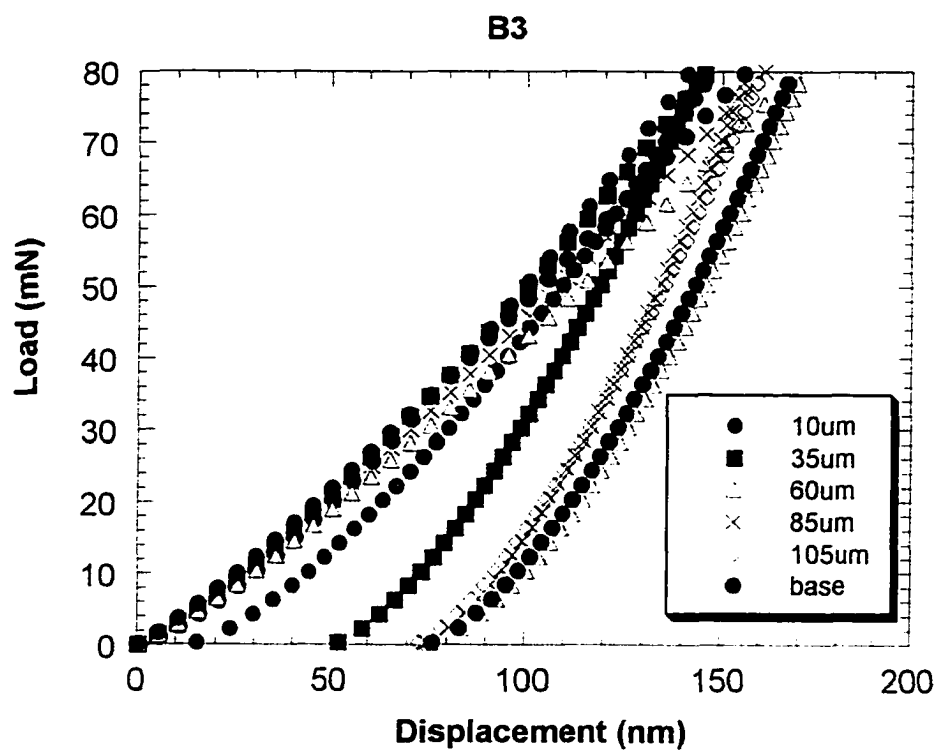


**Figure 25 (cont.)**

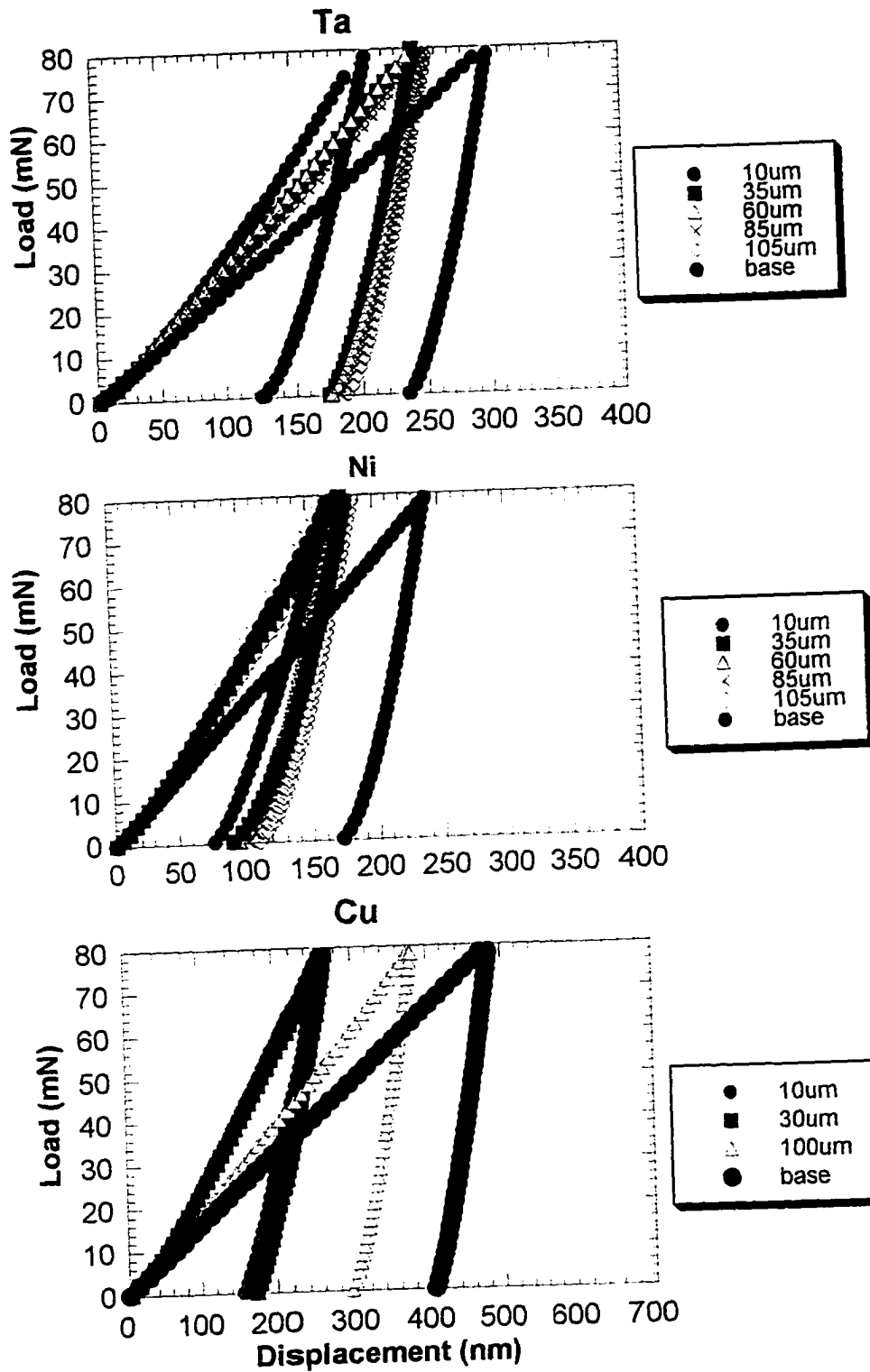


Figure 25 (cont).

**Table VIII.** Summary of the load-displacement data for eroded materials. Particle impact angle-90<sup>0</sup> and velocity-40m/s.

Material	Distance from the eroded surface, $\mu\text{m}$	Plastic zone depth, $\mu\text{m}$	Plastic energy, $W_{\text{plastic}}$ $\text{J} \cdot 10^{-9}$	Total energy, $W$ $\text{J} \cdot 10^{-9}$	Measure of elastic recovery, $W_{\text{elastic}}/W$ or $e^2$	Average $e^2$ within the deformed volume
Cu	10	145	5.54	9.43	0.41	0.28
	35		6.17	9.64	0.36	
	105		11.50	14.59	0.21	
	base <sup>1</sup>		16.41	19.28	0.15	
Ta	10	110	4.83	7.57	0.36	0.27
	35		6.86	9.32	0.26	
	60		7.36	10.12	0.27	
	85		7.45	9.82	0.24	
	105		7.55	9.75	0.23	
	base		9.38	11.50	0.18	
Ni	10	80	2.87	6.11	0.53	0.40
	35		3.68	6.43	0.43	
	60		3.61	6.22	0.42	
	85		3.96	6.40	0.38	
	base		7.14	9.64	0.26	
316L SS	10	60	1.09	5.52	0.80	0.58
	35		2.74	6.60	0.58	
	60		4.85	8.20	0.41	
	base		5.23	8.30	0.36	
Hastelloy -C22	10	50	0.83	5.13	0.84	0.66
	35		2.40	5.84	0.59	
	60		3.24	6.06	0.47	
	base		3.48	6.29	0.45	
Haynes 230	10	50	0.96	4.96	0.80	0.65
	35		2.28	5.55	0.60	
	60		2.98	6.00	0.50	
	base		3.30	6.51	0.49	
B3	10	40	0.61	5.03	0.88	0.7
	35		2.02	5.34	0.62	
	60		3.09	6.09	0.49	
	base		3.24	6.31	0.47	
Inconel 625	10	50	0.84	4.65	0.82	0.71
	35		1.91	5.17	0.63	
	60		2.15	5.30	0.59	
	base		2.28	5.44	0.58	
Ultimet	10	40	0.90	4.51	0.80	0.72
	35		1.55	4.57	0.66	
	60		1.66	4.72	0.65	
	base		1.81	5.25	0.65	

<sup>1</sup> Base measurements were made on unaffected material away from the eroded surface ( $\approx 500 \mu\text{m}$ ).

several annealed metals impacted by iron microspheres. It was found that, in the impact velocity range 20-100 m/s, average  $e^2$  values for Cu, Ni, and stainless steel were 0.12, 0.10, and 0.3, respectively. These values are in reasonable agreement with those measured using nanoindentation technique for base Cu, Ni, and 316L stainless steel (0.15, 0.2, and 0.36, respectively). These results suggest that load-displacement experiments can be successfully used to estimate restitution coefficient within small volume of material. Also, this study definitively showed that, within plastically deformed region, all materials exhibited an increase in restitution coefficient with an increase in hardness near the eroded surface.

*Effect of hardness on restitution coefficient and plastic deformation energy.*

The effect of hardness on measured restitution coefficient is shown in **Figure 26**. Interestingly, the data for all materials and distances from the eroded surface (see Table VIII) can be fitted into a logarithmic-type relationship ( $R^2 = 0.94$ ):

$$e = -0.68 + 0.39 \log(H) \quad (31)$$

where  $H$  is hardness in MPa. This result is somewhat different from that obtained by Latham et al. [57] who showed a linear relationship between Vickers hardness and restitution coefficient (**Figure 27**). However, upon examining **Figure 27**, it can be seen that the hardest tested material was graphite with Vickers hardness of only 400 kg/mm<sup>2</sup> ( $\approx 4000$  MPa). In this study (**Figure 26**), for materials with hardness below 4000-5000

MPa, the relationship between  $H$  and  $e$  could also be described as linear. However, materials with hardness greater than 5000 MPa deviated from the linear relationship. At the same applied load, hard materials have a smaller deformed volume beneath the indenter than soft materials. It can be suggested that, at some level of hardness, the size of the deformed region becomes comparable with the size of the dislocation stress field generated by the indentation. Therefore, changes and any further increase in material hardness will not produce a significant increase in elastic recovery. Tabor [54] suggested that, when the deformed volume is very small, it may contain only a limited number of dislocations and one should expect the hardness of material to approach the theoretical value of a perfect crystal. However, near the eroded surface all materials were highly hardened and, therefore, it is unlikely that during indentation experiments only a limited number of dislocations were affected. It seems that, when indentation size becomes small, additional deformation mechanisms (other than elastic and plastic deformation) may take place that affect energy dissipation. More research is required to determine the effect of hardness on energy loss mechanisms during the indentation process.

#### *Stress-strain analysis of subsurface deformation*

Stress-strain curves were generated from the loading portion of the load-displacement diagrams according to the procedure described in section V.C.1. Stress-strain relationships obtained within the plastically deformed zone at various distances below the eroded surface are shown in **Table IX**. In general, all materials exhibited a decrease in strength coefficient ( $K$ ) and strain hardening coefficient ( $n$ ) with increasing distance from the eroded surface. These findings were expected because material near the eroded

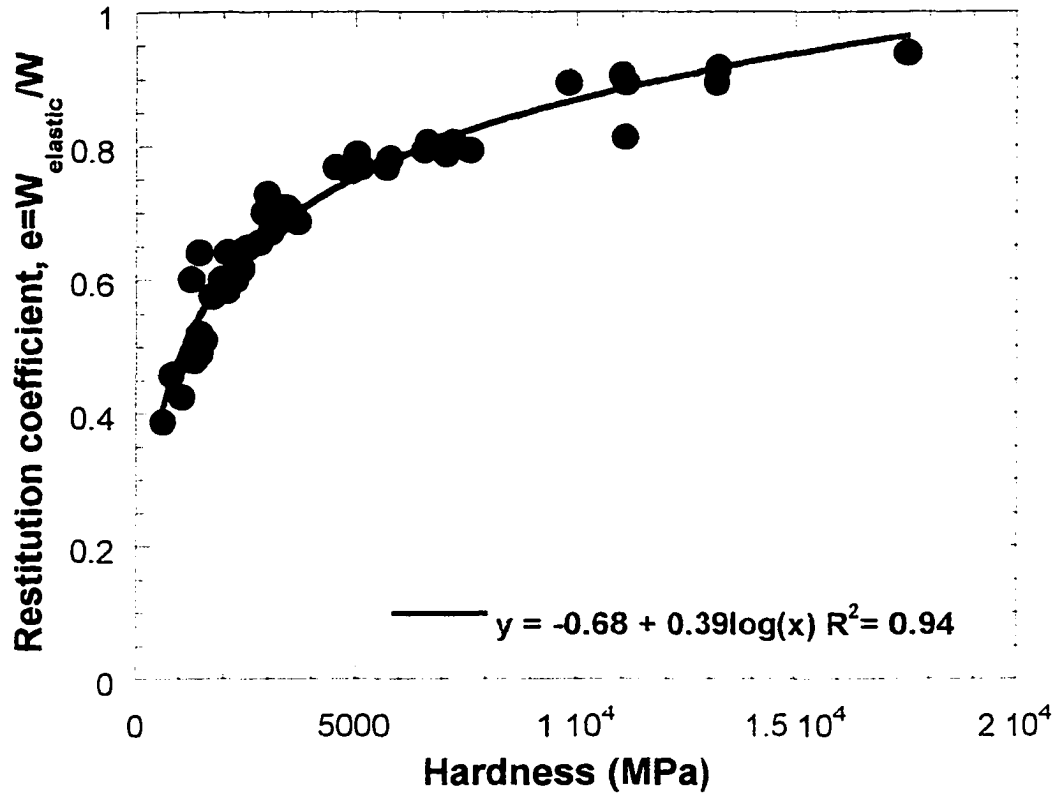


**Figure 26.** Effect of hardness on restitution coefficient,  $e$ , ( $e = \sqrt{W_{\text{elastic}} / W}$ ). logarithmic-type relationship is observed. An increase in material hardness led to an increase in elastic recovery.

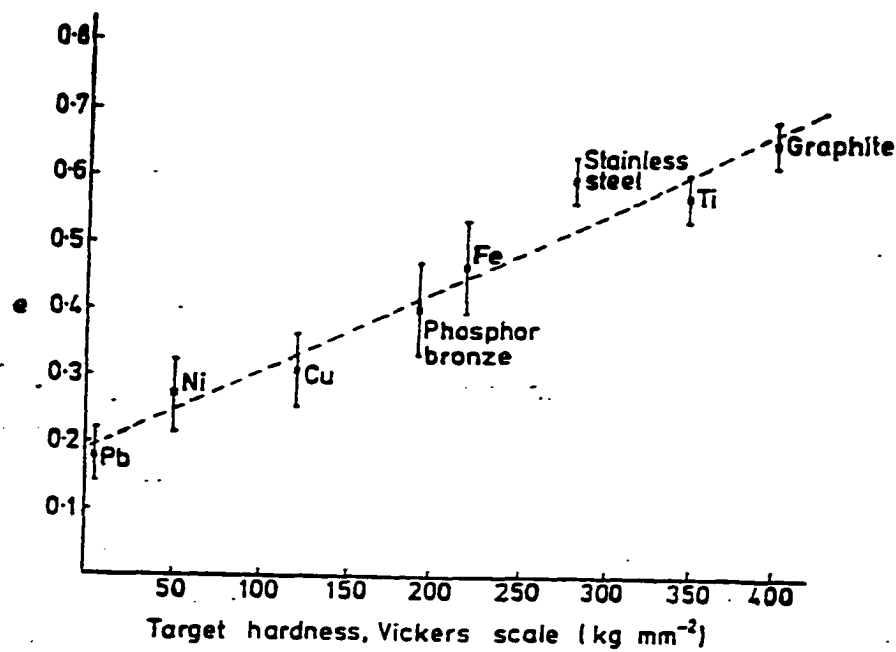


**Figure 27.** Dependence of the restitution coefficient,  $e$ , within the velocity range 20-100m/s on the Vickers hardness [57]; Latham et al. *J. Phys.D: Appl. Phys.*, vol. 10, 1977, p.144]. Linear relationship was observed. Note that maximum hardness is only 400 kg/mm<sup>2</sup>  $\approx$ 4000MPa.



**Table IX.** Stress-strain relationship for all materials eroded at 90<sup>0</sup> particle impact angle and velocity of 40m/s.

Material	Distance from the eroded surface, $\mu\text{m}$	Estimated plastic zone depth, $\mu\text{m}$	Stress-strain equation $\sigma = K\epsilon^n$
Cu	10	140	$4992\epsilon^{0.68}$
	35		$2826\epsilon^{0.48}$
	105		$1046\epsilon^{0.22}$
	base		$569\epsilon^{0.08}$
Ta	10	110	$4131\epsilon^{0.5}$
	35		$1826\epsilon^{0.24}$
	60		$1585\epsilon^{0.18}$
	85		$1579\epsilon^{0.20}$
	105		$1579\epsilon^{0.20}$
	base		$1217\epsilon^{0.16}$
Ni	10	80	$6200\epsilon^{0.55}$
	35		$4447\epsilon^{0.45}$
	60		$5213\epsilon^{0.5}$
	85		$4438\epsilon^{0.44}$
	base		$1432\epsilon^{0.16}$
316L SS	10	60	$8102\epsilon^{0.62}$
	35		$4584\epsilon^{0.46}$
	60		$2959\epsilon^{0.36}$
	base		$2474\epsilon^{0.30}$
Hastelloy-C22	10	50	$10828\epsilon^{0.66}$
	35		$5566\epsilon^{0.46}$
	60		$3945\epsilon^{0.36}$
	base		$3929\epsilon^{0.38}$
Haynes 230	10	50	$9789\epsilon^{0.64}$
	35		$7066\epsilon^{0.56}$
	60		$4734\epsilon^{0.44}$
	base		$4911\epsilon^{0.46}$
B3	10	40	$17398\epsilon^{0.86}$
	35		$8471\epsilon^{0.62}$
	60		$5894\epsilon^{0.54}$
	base		$5240\epsilon^{0.46}$
Inconel 625	10	50	$14913\epsilon^{0.78}$
	35		$7819\epsilon^{0.58}$
	60		$7366\epsilon^{0.54}$
	base		$7134\epsilon^{0.52}$
Ultimet	10	40	$13499\epsilon^{0.72}$
	35		$10826\epsilon^{0.66}$
	60		$8696\epsilon^{0.56}$
	base		$9318\epsilon^{0.60}$

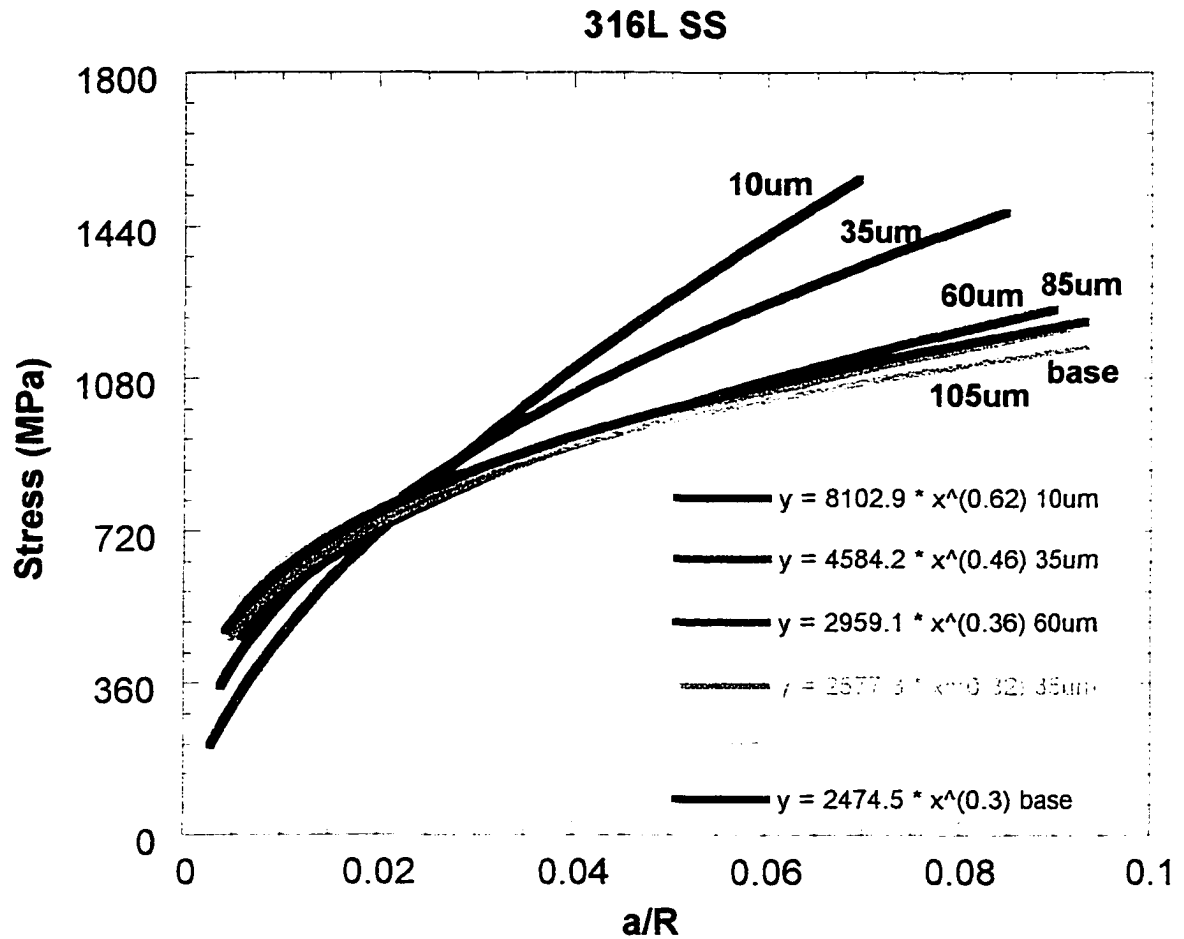


**Figure 28.** Stress-strain curves obtained by using load-displacement measurements at various distances below the eroded surface of the 316L SS alloy. Note changes in the stress-strain behavior with distance from the eroded surface.

surface is more brittle than material away from the surface. As an example, stress-strain curves obtained at various distances below the eroded 316L SS alloy are shown in **Figure 28**. This figure illustrates changes in the stress-strain behavior with distance from the eroded surface. It can be seen that the strength and strain hardening coefficients decreased from 8102 to 2474 MPa and 0.62 to 0.30, respectively, with distance from the eroded surface. To illustrate the use of load-displacement measurements in analyzing stress-strain behavior within a small volume of material, data from the *indentation* tests and conventional compression were compared. Good correlation was observed between the two test methods for strain hardening and strength coefficients in **Figure 29a and b**. Thus, indentation load-displacement measurements can be used to analyze stress-strain behavior of materials within small volumes of material for which conventional compression tests cannot be conducted (i.e., coatings).

To analyze the stress-strain behavior of materials that experienced high strain-rate deformation, load-displacement tests were done on selected bulk samples (316L SS, Inconel-625, B3, and Cu) that were compressed at high strain-rates ( $\approx 10^3$ - $10^4$  s<sup>-1</sup>) using the Hopkinson bar technique. The results were then compared with the stress-strain behavior of the materials near the eroded surface (10-35µm from the surface) that also experienced high strain rate deformation during particle impact. If the stress-strain relationship for the eroded sample was similar to its relationship in the high strain-rate compression sample, it can be suggested that strain rates during erosion and high-strain rate compression tests are also comparable. **Figure 30** shows the stress-strain curves

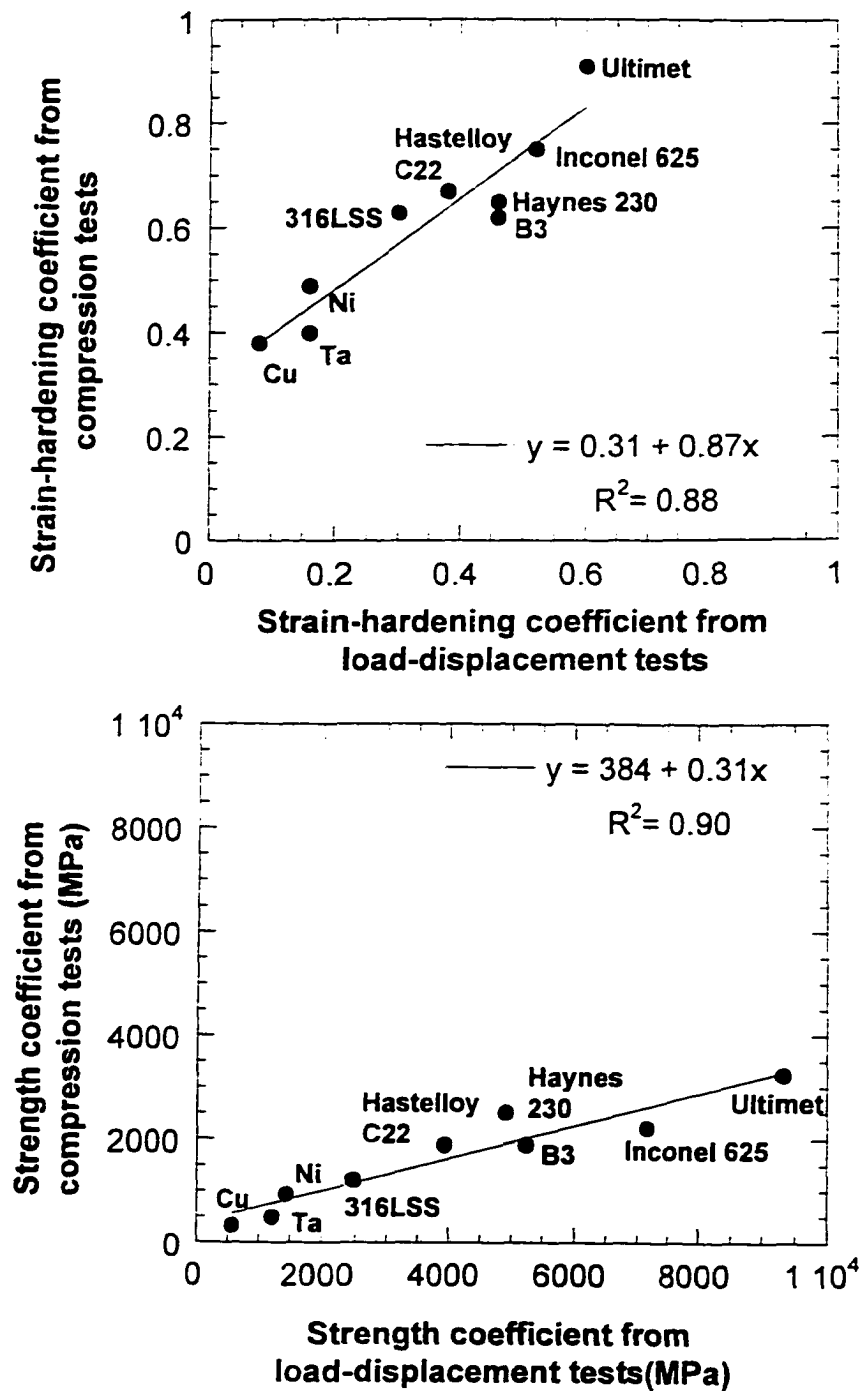


**Figure 29 a and b.** Correlations between *indentation* tests performed on annealed materials and conventional compression tests performed on the bulk samples. a) correlation between strain hardening coefficients; b) correlation between strength coefficients.

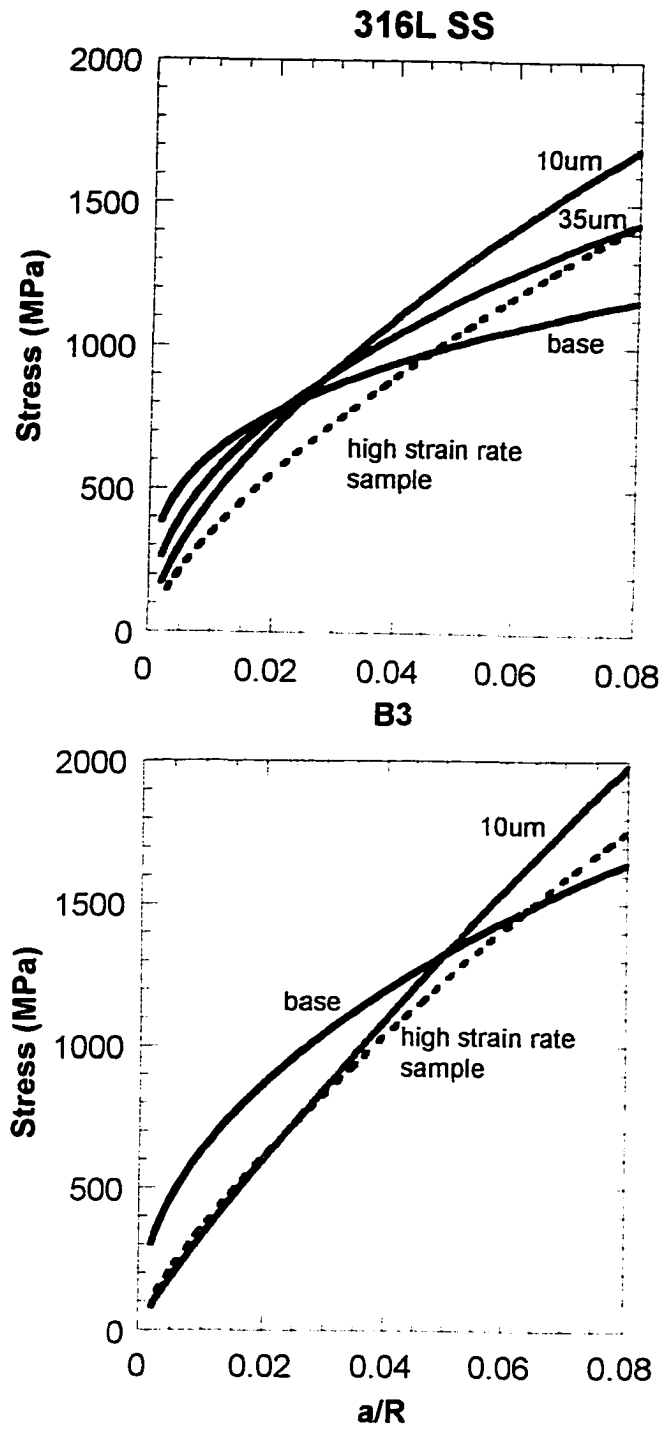


**Figure 30 (a-d).** Indentation stress-strain diagrams obtained for samples below the eroded surface and on bulk high strain-rate compression samples (Hopkinson bar method, strain rates  $10^3$ - $10^4$  s $^{-1}$ ). Note similarities between stress-strain curves in the vicinity of the eroded surface (10-35  $\mu$ m) and stress-curves obtained on high strain-rate compression samples.

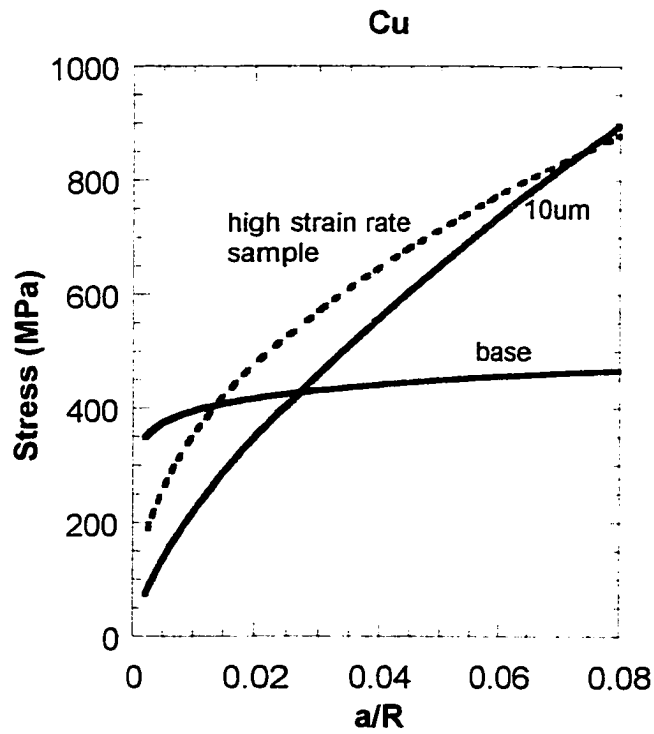
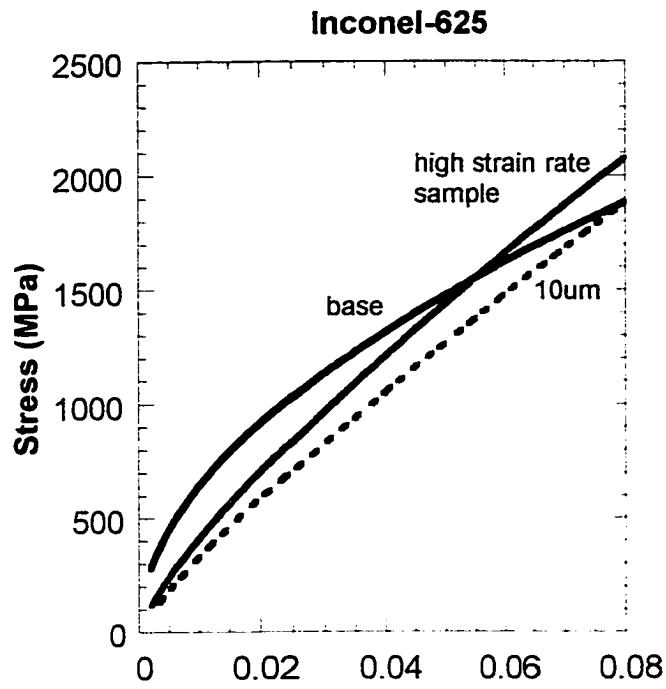


**Figure 30 (cont.)**

**Table X.** Indentation stress-strain relationship obtained on samples below the eroded surface and on bulk high strain-rate compression samples (Hopkinson bar method, strain rates  $10^3$ - $10^4$  s<sup>-1</sup>). Note similarities in the stress-strain relationships in the vicinity of the eroded surface (10-35  $\mu$ m) and stress-strain relationship obtained on high strain-rate compression samples.

Material	Distance from the eroded surface,  $\mu$ m	Stress-strain relationship below the erode surface  $\sigma=K\epsilon^n$	Stress-strain relationship for bulk high strain-rate compression samples  $\sigma=K\epsilon^n$
Cu	10 35 105 base	$4992\epsilon^{0.68}$ $2826\epsilon^{0.48}$ $1046\epsilon^{0.22}$ $569\epsilon^{0.08}$	$2626\epsilon^{0.44}$
316L SS	10 35 60 base	$8102\epsilon^{0.62}$ $4584\epsilon^{0.46}$ $2959\epsilon^{0.36}$ $2474\epsilon^{0.30}$	$7987\epsilon^{0.68}$
B3	10 35 60 base	$17398\epsilon^{0.86}$ $8471\epsilon^{0.62}$ $5894\epsilon^{0.54}$ $5240\epsilon^{0.46}$	$11979\epsilon^{0.76}$
Inconel 625	10 35 60 base	$14913\epsilon^{0.78}$ $7819\epsilon^{0.58}$ $7366\epsilon^{0.54}$ $7134\epsilon^{0.52}$	$15721\epsilon^{0.84}$

obtained on both type of samples. Best-fit, stress-strain relationships for both type of samples are shown in **Table X**. Note similarities between stress-strain curves obtained near the eroded surface (10-35 $\mu$ m) and those obtained on using indentation tests on bulk compression samples. For example, for the 316L SS and Inconel-625 alloys, K and n values for the high strain-rate compression samples were less than 10% different than those measured at 10  $\mu$ m from the eroded surface. For the Cu and B3 alloys, K and n values lie somewhere between those measured at 10-35  $\mu$ m below the eroded surface. It should be noted that because of the indenter size, no indentations were made closer than 10 $\mu$ m from the eroded surface. Therefore, it is possible that values for K and n at the immediate surface could be higher than those measured at 10  $\mu$ m from the surface. Also, the stress-state experienced by materials during uniaxial compression and erosion are different. During solid particle erosion, the material below the impacting particle has large hydrostatic stresses imposed by the elastic field that surrounds the plastically deformed field. In contrast, these stresses are negligible during uniaxial compression tests. Therefore, some caution must be taken when correlations are made between uniaxial compression and erosion tests. Stress-strain relationships provided a reasonable estimate that, for the experimental conditions used in this study, strain rates imposed below the eroded surface are comparable to those measured during high strain-rate compression tests. Thus, high strain-rate compression tests can be used to estimate stress-strain behavior of materials during erosion. Also, since material below the eroded surface experiences a gradient of strain rates (highest at the surface), nanoindentation load-



displacement tests can be performed on eroded samples to provide useful information on stress-strain behavior of materials at high strain rates without conducting the Hopkinson bar test.

### ***V.C.3. Summary of the analysis of the subsurface deformation during erosion***

Subsurface deformation behavior of ductile Ni, Co, and Fe-base alloys and commercially pure Ni, Cu, and Ta exposed to solid particle erosion ( $90^0$  particle impact angle and velocity of 40m/s) was analyzed. The Nanoindenter II<sup>®</sup> was used to determine load-displacement and stress-strain response of materials below the eroded surface. The results are summarized as follows:

1. A nanoindentation method was utilized to estimate the restitution coefficient within plastically deformed regions of eroded samples which provides a measure of the rebounding ability of a material during particle impact.
2. An increase in hardness ( $H$ ) near the eroded surface led to an increase in restitution coefficient ( $e$ ) according to the logarithmic-type relationship:  $e = -0.38 + 0.39 \log(H)$ . Consequently, the increase in hardness produced a decrease in amount of plastic deformation dissipated into the material.
3. An experimental technique was developed to determine changes in stress-strain behavior of material below the eroded surface. Strength and strain-hardening coefficients decreased with distance from the eroded surface.
4. Stress-strain behavior of materials near the eroded surface was similar to that observed during high strain-rate compression tests. Thus, strain rates imposed below

the eroded surface were comparable to those measured during high strain-rate compression tests ( $10^3$ - $10^4$  s<sup>-1</sup>). High strain-rate compression tests can be used to estimate stress-strain behavior of materials during erosion.

## **V.D. MECHANISM OF ENERGY DISSIPATION DURING EROSION AT NORMAL IMPACT ANGLE**

### ***V.D.1. Measurement of energy absorbed during erosion***

The relative ability of a material to dissipate particle impact energy can be determined by calculating the area under the curve of microhardness versus distance from the eroded surface. This area can be interpreted as a measure of the amount of energy that the material absorbs during particle impact before it reaches the critical fracture stress. An analogy can be made between the true stress-strain curve and the microhardness profile curve after erosion. The area under the stress-strain curve represents the energy per unit volume that the material can absorb before fracture. For the microhardness profiles, the hardness of the material can be correlated to its strength. This relationship can be described by  $H=A\sigma_y$ , where  $H$  is the hardness,  $\sigma_y$  is the yield strength, and  $A$  is a constant. A schematic illustration of the change in microhardness with depth below the eroded surface is shown in **Figure 31**. The microhardness profile curve represents the variation in strength beneath the eroded surface as a result of changes in strain and strain-rate imposed by particle impacts. The decrease in hardness with distance from the eroded surface is caused by a decrease in strain-rate and strain. Therefore, the hardness versus distance from the eroded surface curve can be qualitatively correlated to the stress versus strain curve (**see Figure 31**). By analogy with the true stress-strain curve, the area under hardness-distance curve may be interpreted as energy used to plastically deform a volume of material. Deformation energy or work is defined as a force necessary to deform a unit volume. The force that is being applied during

erosion is determined by the increase in hardness within the plastically deformed volume, and the deformed volume is defined by the plastic zone size. To further illustrate similarities between the stress-strain diagram and a hardness profile, the slopes of microhardness profile and average strain hardening coefficient within the plastically deformed volume can be correlated as shown in **Figure 32**. The average strain hardening coefficients within the plastically deformed volume were determined from indentation stress-strain diagrams obtained at various distances below the eroded surface using a Nanoindenter II<sup>®</sup>. The following equation was used to calculate the average value of strain hardening coefficient:

$$average = \frac{\int_0^d n(d) \partial d}{d} \quad (32)$$

where  $n$  is the strain hardening coefficient and  $d$  is the plastic zone depth. The procedure for determining the strain hardening coefficient from nanoindentation tests was described in section V.C. **Figure 32** shows a trend of an increase in the slope of the microhardness profile with the increase in the average strain hardening coefficient. This correlation suggests similarities between microhardness profiles developed for eroded sample and high strain rate compression samples. Qualitatively, microhardness profile represents a variation of strength with distance from the eroded surface that resulted from changes in stress-strain behavior below the eroded surface due to the changes in strain-rate and strain. It can be suggested that microhardness curve is a compilation of different stress-strain responses below the eroded surface.

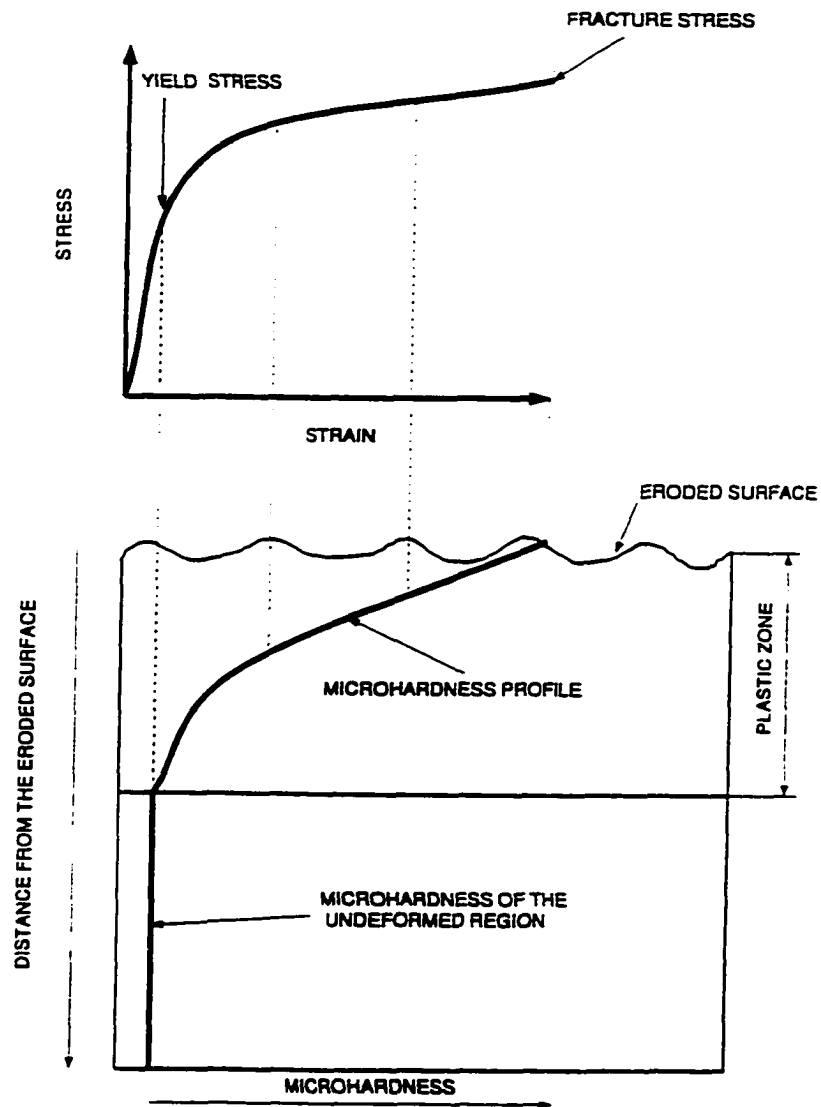


**Figure 31.** A schematic diagram of change in microhardness with distance from the eroded surface. Correlation between the true stress-strain diagram and microhardness profile is only qualitative.

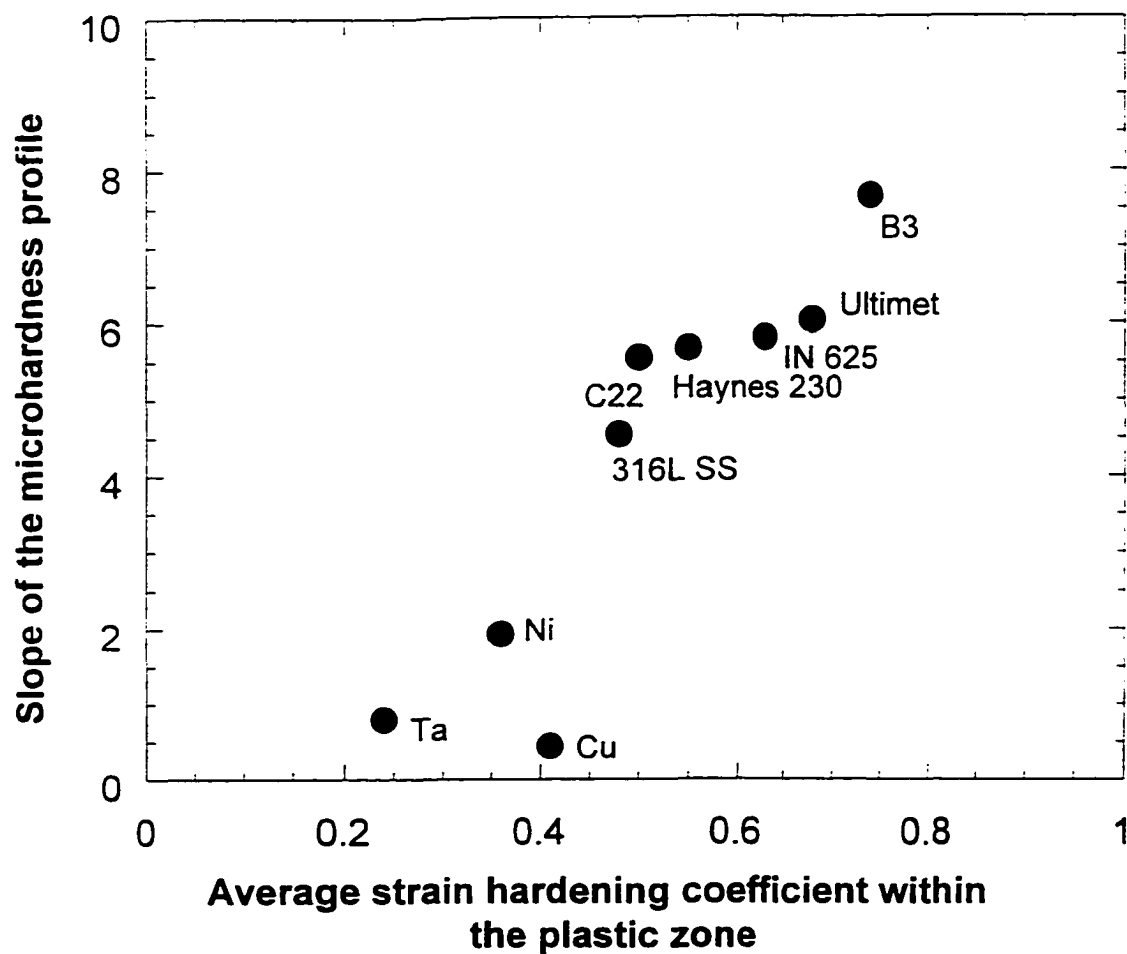


**Figure 32.** The slopes of microhardness profiles for all materials are plotted against their average strain hardening coefficient within the plastically deformed volume. The average strain hardening coefficients were determined from the indentation stress-strain curves obtained at different distances below the eroded surface.

A schematic diagram that illustrates calculation of the area under the microhardness profile curve is shown in **Figure 33**. To find this area, the microhardness data within the plastically deformed zone was fitted into the power-law relationship and then integrated from 0 to L range according to:

$$Area = \int_0^L H(L) dL \quad (33)$$

where  $L$  is the plastic zone volume, and  $H(L)$  is the variation of hardness with distance from the eroded surface. Plastic zone volume ( $L=S*d$ ) is determined by the plastic zone depth  $d$  and the surface area  $S$  of the eroded samples which was kept constant at  $\approx 0.90 \text{ cm}^2$ . To simplify calculations of area under the microhardness curve, it can be assumed that hardness decreases linearly from the eroded surface and the area under the microhardness curve can be estimated according to:

$$Area = \frac{H_{surface} + H_{base}}{2} * L \quad (34)$$

The use of equation 34 to estimate the area under the curve is reasonably accurate with less than 5% difference between the two approaches (eqs. 33 and 34).

#### Area under the microhardness curve and erosion resistance

In the previously developed erosion model (section V.B.) the erosion rate was shown to be proportional to the unitless erosion parameter. This parameter is equal to the ratio of input energy to the energy that the material can absorb before fracture. The energy absorbed is represented by the area under the microhardness curve, while the energy transferred is determined by the impacting particle energy and the restitution

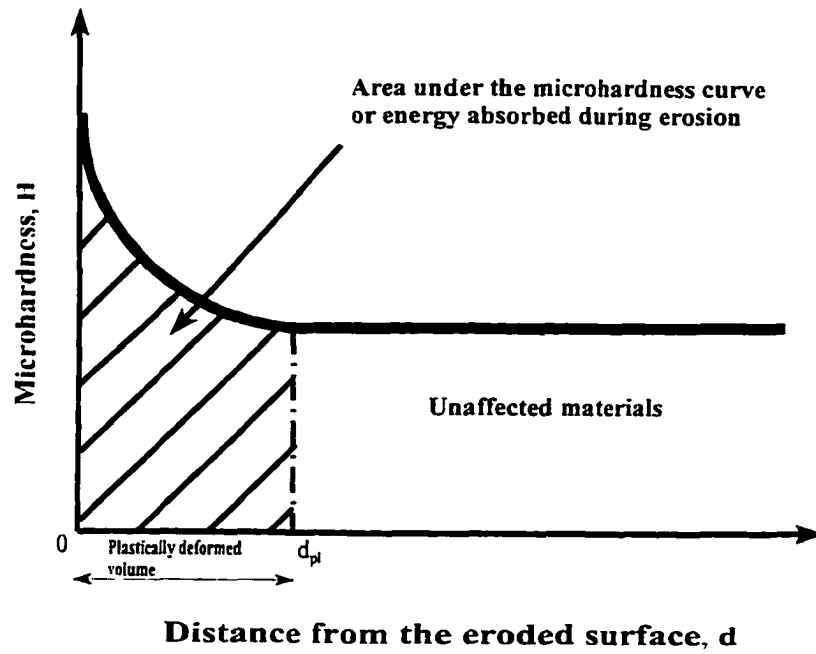


**Figure 33.** A schematic diagram that illustrates calculation of the area under the microhardness curve.



coefficient of the target material according to the previously shown relationship:

$$KE_{pd} = \frac{mV^2}{2}(1 - e^2) \quad (14)$$

where  $KE_{pd}$  is the energy transferred into plastic deformation in Joules and  $e$  is the restitution coefficient. The empirical relationship between restitution coefficient and hardness of material ( $H$ ) was determined from load-displacement indentation experiments below the eroded surface (section V.C):

$$e = -0.68 + 0.39 \log(H) \quad (31)$$

Thus, an equation for erosion rate and erosion parameter can be written as:

$$Erosion \sim E_{parameter} = \frac{\frac{mV^2}{2}(2.38 - 0.53 \log(H))}{A} \quad (35)$$

where the  $E_{parameter}$  is the erosion parameter,  $A$  is the area under the microhardness curve in Joules and  $H$  is the average hardness within plastic zone in MPa. The calculated values of erosion parameter from equation 35 are plotted against experimentally measured erosion rates in **Figure 34**. It can be seen that a decrease in the erosion parameter leads to a decrease in erosion rates. Thus, materials with high hardness and large area under the microhardness curve offer good erosion resistance. According to equation 34, materials that show high hardness ( $H_{base}$ ) and high hardening ability ( $H_{surface}$ ) along with large plastic zone size ( $L$ ) will have a large area under the

microhardness curve. To predict erosion resistance of materials, it is important to determine factors affecting surface hardness and plastic zone size during erosion.

#### ***V.D.2. Surface hardening effect during erosion***

In the erosion literature it is assumed that surface hardening occurs mainly because of the *strain hardening effect* [42]. However, the *strain-rate hardening* effect is largely ignored. If the eroded material is strain-rate sensitive, it will experience both strain and strain-rate hardening effects. The resulting flow stress,  $\sigma$ , is given by [58]:

$$\sigma = C\varepsilon^n \dot{\varepsilon}^m \quad (36)$$

where  $C$  is a constant,  $\varepsilon$  is the strain,  $\dot{\varepsilon}$  is the strain rate,  $n$  is the strain hardening coefficient, and  $m$  is the strain-rate sensitivity. This equation shows that at high strain rates ( $>10^2 \text{ s}^{-1}$ ), strain-rate sensitive materials ( $m \gg 0$ ) can exhibit a significant increase in flow stress due to *strain-rate hardening*. Recall **Figure 21**, for example, during the high strain-rate compression test conducted at high strain rates of  $\approx 10^3$  to  $10^4$ , the materials in this study exhibited an increase in yield strength ( $\sigma_{0.2}$ ) by a factor of 1.1-2.0. Therefore, the increase in hardness at the eroded surface consists of two components: (1) an increase due to the strain-rate hardening ( $H \sim \dot{\varepsilon}^m$ ) and (2) an increase due to the strain hardening ( $H \sim \varepsilon^n$ ). **Table XI** lists the ratios of  $\sigma_{0.02, \text{ high rate}}/\sigma_{0.02, \text{ low rate}}$  during compression tests and  $H_{\text{surface}}/H_{\text{base}}$  for materials after erosion tests. It can be seen that for eroded

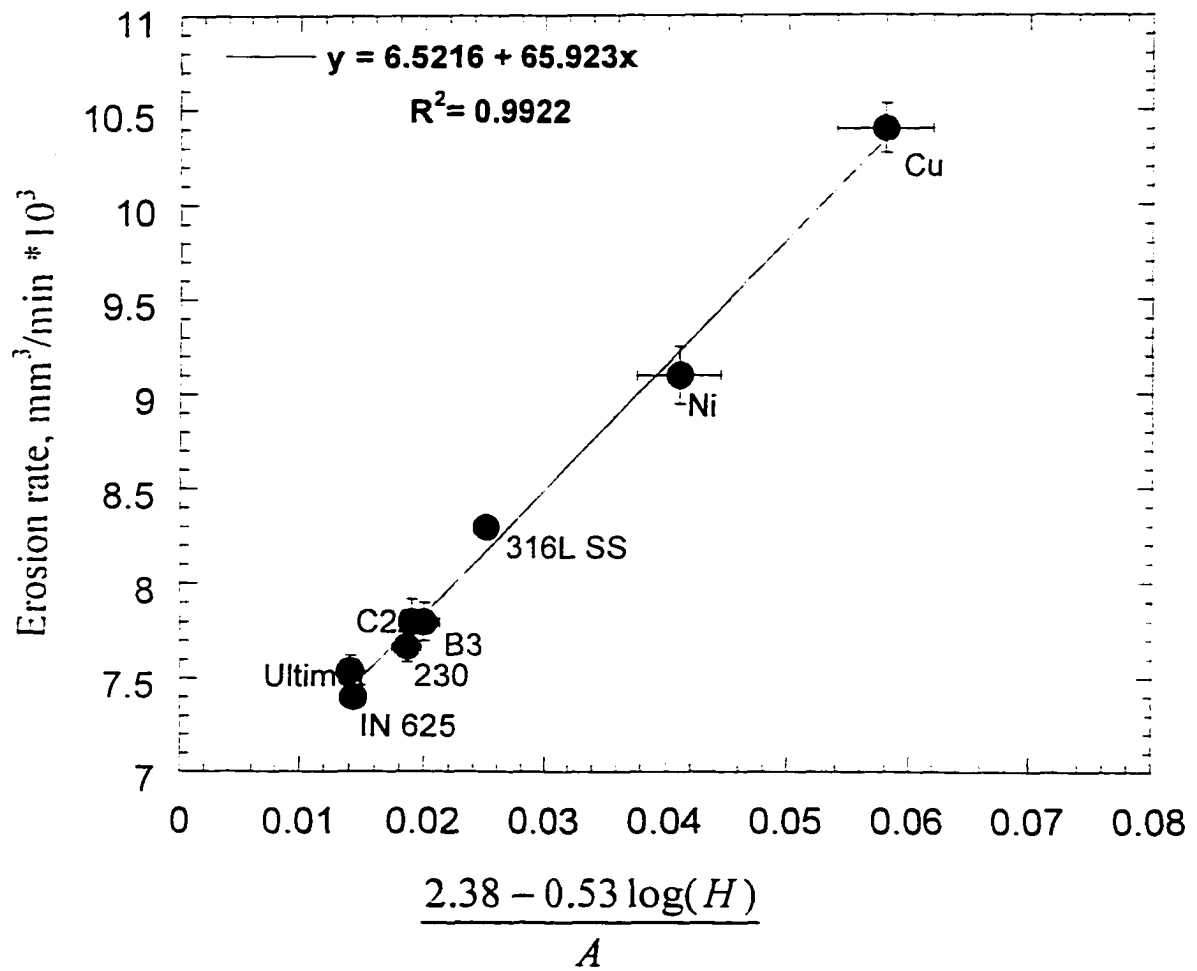


**Figure 34.** Erosion parameter calculated from equation 35 is plotted against experimentally determined volumetric erosion rates. Good correlation is observed. A decrease in the erosion parameter leads to a decrease in the erosion rate.

materials this ratio ranges between 1.4-2.15. For most of the materials, a good agreement between strength and hardness ratios is observed. These results indicate that, because of the high strain rates imposed during erosion, strain-rate hardening effect is a major cause for the increase in surface hardness. It should be noted that strain-hardening could also contribute to the increase in surface hardness. However, because of the imposed strain - rates during erosion, strain hardening addition to surface hardness seems to be much smaller than that due to strain-rate hardening.

#### Strain-rate sensitivity during erosion

To determine the effect of material properties of its strain-rate sensitivity, indentation stress-strain curves were obtained at various distances below the eroded surface by using Nanoindenter II with a 50  $\mu\text{m}$  ball indenter. Because of the gradient in strain-rates below the eroded surface, the resultant stress-strain curves represent the materials behavior at different strain rates. Thus, for a given strain level, strain rate sensitivity,  $m$ , can be calculated from [58]:

$$\frac{\sigma_2}{\sigma_1} = \left( \frac{\dot{\epsilon}_2}{\dot{\epsilon}_1} \right)^m \quad (37)$$

where  $\sigma_1$  and  $\sigma_2$  are the flow stresses at two strain rates  $\dot{\epsilon}_1$  and  $\dot{\epsilon}_2$ . The stress-strain relationships for materials near the eroded surface (10  $\mu\text{m}$ ), that correspond to the highest imposed strain rate, and stress-strain relationship for unaffected materials are shown in **Table XII**. Also, calculated strain-rate sensitivities are listed in this table. It should be

**Table XI.** Comparison of the effect of strain-rate on strength increase during high strain-rate compression and erosion tests.

Material	$\sigma_{2(0.02)}/\sigma_{1(0.02)}$ at $\dot{\epsilon}_2 \approx 10^3 - 10^4 \text{ s}^{-1}$ and $\dot{\epsilon}_1 \approx 10^{-3} \text{ s}^{-1}$ , compression tests	$H_{\text{surface}}/H_{\text{base}}$ , erosion tests
Ta	2.00	1.78
316L SS	2.00	2.15
Hastelloy-C22	1.82	1.84
Inconel-625	1.80	1.70
Cu	1.63	1.84
Ultimet	1.60	1.4
Haynes 230	1.52	1.75
B3	1.40	1.7
Ni	1.10 <sup>1</sup>	1.68

<sup>1</sup> Estimated from the literature; [Follansbee, P.S. et al., *Acta metall. mater.*, Vol. 38, n. 7, 1990, pp. 1241-1254].

**Table XII.** Estimated strain-rate sensitivities of eroded materials. Indentation tests below the eroded surface were conducted to determine stress-strain relationships. At 10um from the eroded surface strain rate is the highest  $\approx 10^5 \text{ s}^{-1}$ , while strain rate in the base material is  $10^{-3} \text{ s}^{-1}$ . Equation 36 was used to estimate values of m.

Material	Depth, $\mu\text{m}$	$\sigma = K\dot{\epsilon}^n$	m
Cu	10	$4992\dot{\epsilon}^{0.68}$	0.078
	base	$569\dot{\epsilon}^{0.08}$	
Tu	10	$4131\dot{\epsilon}^{0.5}$	0.044
	base	$1217\dot{\epsilon}^{0.16}$	
Ni	10	$6200\dot{\epsilon}^{0.55}$	0.054
	base	$1432\dot{\epsilon}^{0.16}$	
316L SS	10	$8102\dot{\epsilon}^{0.62}$	0.043
	base	$2474\dot{\epsilon}^{0.30}$	
Hastelloy-C22	10	$10828\dot{\epsilon}^{0.66}$	0.037
	base	$3929\dot{\epsilon}^{0.38}$	
Haynes 230	10	$9789\dot{\epsilon}^{0.64}$	0.026
	base	$4911\dot{\epsilon}^{0.46}$	
B3	10	$17398\dot{\epsilon}^{0.86}$	0.039
	base	$5240\dot{\epsilon}^{0.46}$	
Inconel 625	10	$14913\dot{\epsilon}^{0.78}$	0.028
	base	$7134\dot{\epsilon}^{0.52}$	
Ultimet	10	$13499\dot{\epsilon}^{0.72}$	0.012
	base	$9318\dot{\epsilon}^{0.60}$	

noted that, due to the indenter resolution, no measurements were made closer than 10  $\mu\text{m}$  from the eroded surface and therefore, actual stress-strain relationship at the eroded surface could be different from those measured at 10  $\mu\text{m}$  below the surface. However, to estimate and compare strain-rate behavior of different alloys, the data obtained at 10  $\mu\text{m}$  from the eroded surface provides a reasonable approximation.

For the normal impact of a sphere on to a rigid plastic surface, Hutchings [45] showed that:

$$\dot{\epsilon} = \frac{2^{1.5} v^{0.5}}{5\pi r} \left[ \frac{3P}{2\rho} \right]^{0.25} \quad (12)$$

where  $\dot{\epsilon}$  is the mean strain rate ( $\text{s}^{-1}$ ),  $v$  is the particle velocity (m/s),  $r$  is the sphere radius (m),  $H$  is the hardness of the target material ( $\text{N/m}^2$ ), and  $\rho$  is the particle density ( $\text{kg/m}^3$ ).

By using this equation for the experimental conditions and materials used in this study, it was found that the strain rates during erosion could range between  $1.2\text{-}2.0 \times 10^5 \text{ s}^{-1}$ .

**Table XII** shows that the softest material, Cu, showed the highest strain-rate sensitivity of 0.078, while the hardest material, Ultimet, showed the lowest strain-rate sensitivity of 0.012. These values indicate relatively low strain-rate sensitivity and they are similar to those observed for metallic materials at room temperature [58]. During particle impact, materials with high strain-rate sensitivity could exhibit a larger increase in surface hardness ( $H_{\text{surface}}/H_{\text{base}}$ ) than materials with low strain-rate sensitivity. However, it does

not necessarily lead to an increase in the area under the curve or energy absorbed. Strain-rate sensitivity is also related to the base hardness of the material, as discussed below.

*Effect of hardness on strain-rate sensitivity and plastic deformation depth*

The effect of base material hardness on strain-rate sensitivity is shown in **Figure 35**. Strain-rate sensitivity decreases with increasing material hardness. Other researchers observed a similar relationship in bulk steel samples [58]. Thus, harder materials exhibit a lower strain-rate hardening ability than softer materials. This behavior could be related to the activation energy required to initiate deformation according to [59]:

$$H = A_0 e^{\frac{-Q}{RT}} \quad (38)$$

where  $H$  is hardness,  $A_0$  is a constant,  $Q$  is the activation energy,  $R$  is the gas constant, and  $T$  is temperature. Hard materials have a high activation energy and, thus, are less sensitive to changes in strain rates than soft materials. Strain-rate sensitivity affects the ability of a material to absorb impact energy erosion. On one hand, an increase in strain-rate sensitivity is desirable for erosion resistance because of the increase in  $H_{\text{surface}}$  that will increase the area under the microhardness curve. However, materials with high strain-rate sensitivity usually have lower hardness or yield strength which will decrease the area under the curve.

To determine the area under the microhardness profile curve, microhardness tests below the eroded surface are necessary. Results presented in this study showed that, because strain-rate hardening is the major contributor to the increase in surface hardness,

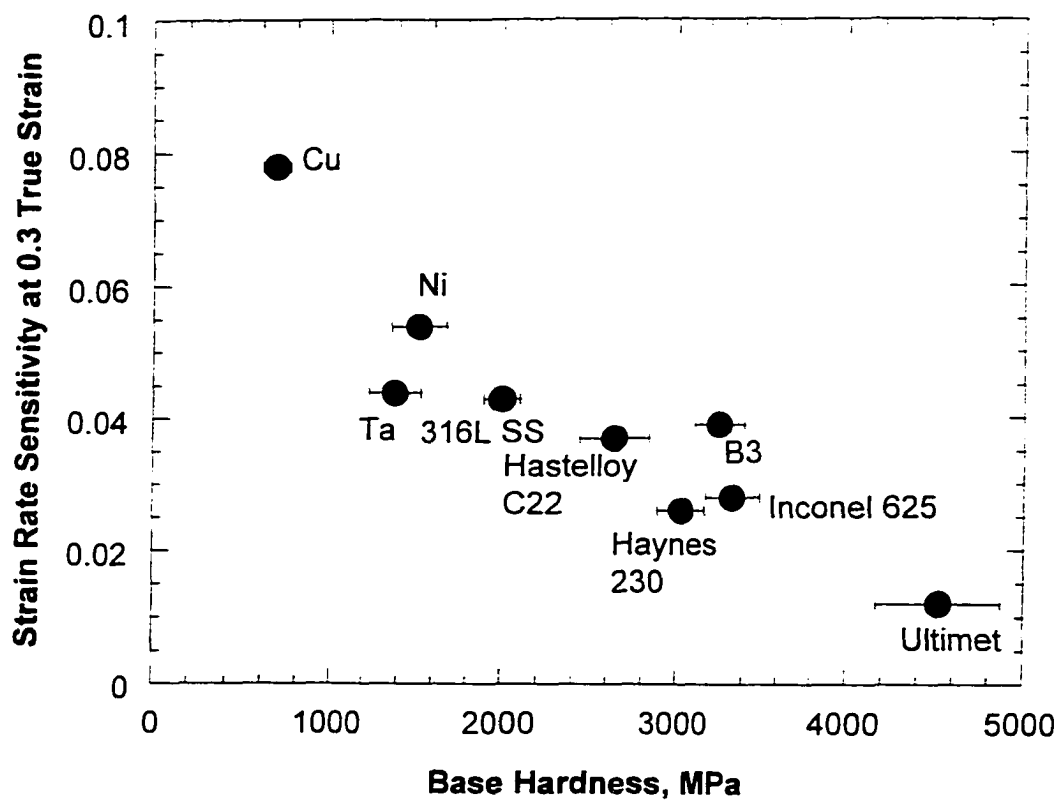


**Figure 35.** The effect of hardness on strain-rate sensitivity. Strain-rate sensitivity decreases with increasing hardness.



( $H_{\text{surface}}$ ) can be reasonably estimated from equation 37 knowing a material hardness ( $H_{\text{base}}$ ) and strain-rate sensitivity. Thus, it is important to estimate the plastic zone size based on easily measurable mechanical properties of the material. It can be assumed that during the impact process, the size of the plastic zone beneath the particle is proportional to the size of the activation area during deformation. Activation area is defined as the area swept out by dislocations during the activation event (i.e., deformation) [60, 61] and can be found from [62]:

$$A_{\text{activation}} = \frac{mkT}{b\sigma} \quad (39)$$

where  $A_{\text{activation}}$  is the activation area,  $m$  is the strain-rate sensitivity,  $k$  is the Boltzmann constant,  $T$  is the temperature,  $b$  is the Burgers vector, and  $\sigma$  is the applied stress. The applied stress needed to initiate plastic deformation corresponds to the hardness of the material. Also, Hertzberg [63] measured the size of the Burgers vectors for a variety of steels, superalloys, and aluminum alloys. He found that their Burgers vectors were very similar and varied between  $2.48\text{--}2.86 \times 10^{-10}$  m. Therefore, equation 39 illustrates that, at constant temperature, materials with high strain-rate sensitivity to hardness ratio ( $m/H$ ) should have a large activation area. The plastic zone beneath the impacting particle represents the volume of material in which dislocation movement and generation take place. Its depth represents the cumulative effect of multiple particle impacts. Therefore, the size of the plastic zone during erosion should be related to the activation area during the deformation event. The effect of strain rate sensitivity and hardness on plastic zone

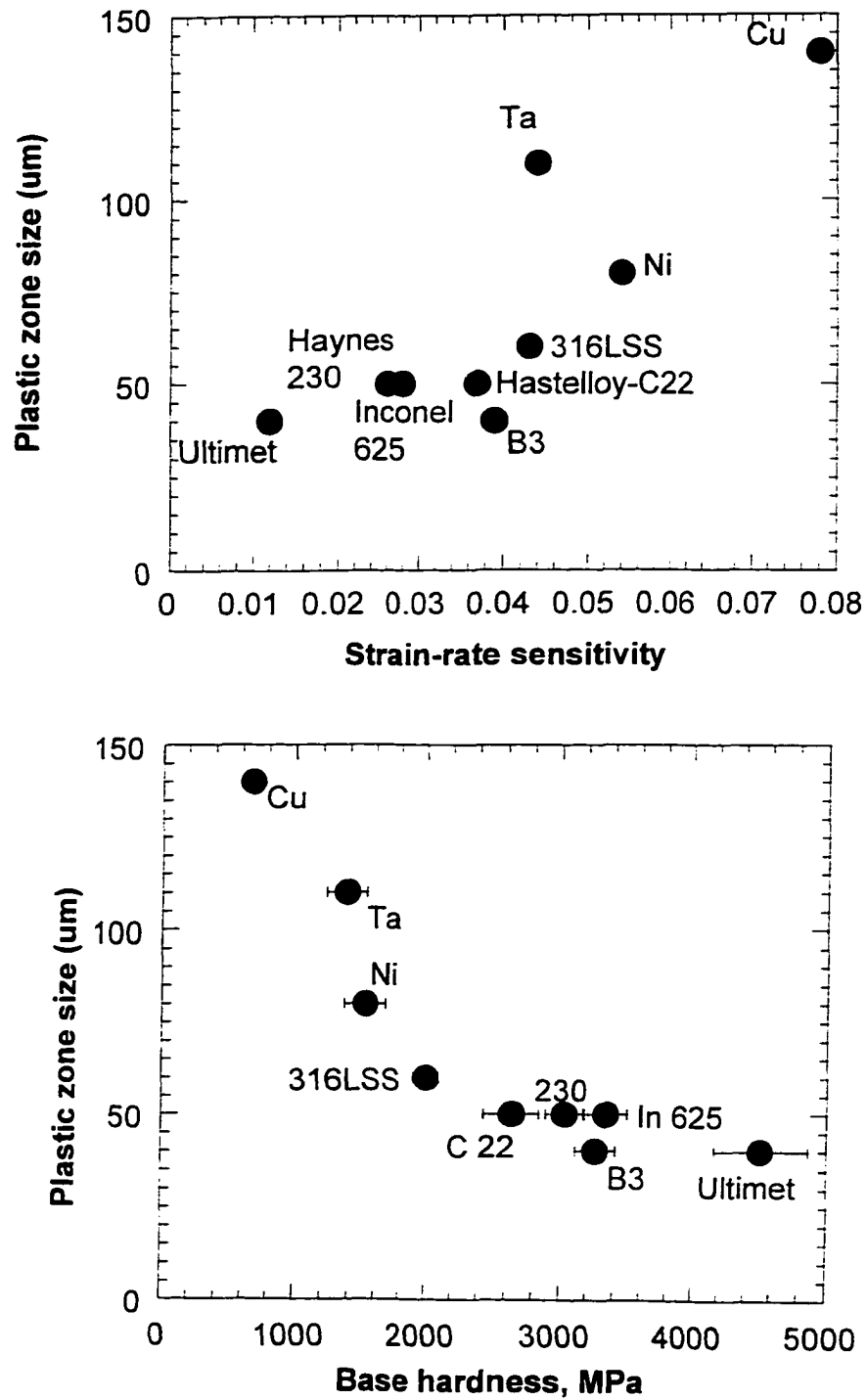


**Figure 36 a and b.** The effect of strain-rate sensitivity and hardness on plastic zone size during erosion. a) strain-rate sensitivity effect; b) hardness effect.

size is shown in **Figure 36a and b**. This figure shows a trend of an increase in plastic zone size with an increase in strain-rate sensitivity and decrease in hardness. These results are in agreement with equation 39. To observe the effect of both strain-rate sensitivity and

hardness on plastic zone size during erosion, the plastic zone depth is plotted against the  $m/H$  ratio in **Figure 37**. With the exception of Ta, good correlation is observed between these two parameters indicating that materials with high  $m/H$  ratio may develop a large plastic zone during erosion. Thus, for different materials, the size of the plastic zone can be compared based on their strain-rate sensitivity to hardness ratio.

#### *Proposed procedure to estimate relative erosion resistance of ductile materials*

According to the developed erosion model, the erosion resistance of ductile materials can be compared based on their mechanical properties. Hardness of the material determines the amount of energy that will be transferred into plastic deformation during erosion, while the area under the microhardness curve represents the portion of this energy that the material can absorb. Area under the curve can be estimated from equation 34 based on the measured  $H_{\text{base}}$ ,  $H_{\text{surface}}$ , and plastic zone size ( $L$ ). Then, the erosion rate can be correlated to the erosion parameter that incorporates hardness and the area under the microhardness curve. However, post-erosion analysis of the eroded samples is required to determine  $H_{\text{surface}}$  and plastic zone size. To compare relative erosion resistance of ductile materials without conducting erosion tests, the following procedure can be used as a guideline:

1)  $H_{base}$  can be measured from a hardness test on a bulk sample.

2)  $H_{surface}$  can be estimated based on strain-rate imposed during erosion ( $\dot{\epsilon}_{erosion}$ ),

strain-rate sensitivity of the eroded material ( $m$ ), and its base hardness according to:

$$H_{surface} \approx H_{base} \left( \frac{\dot{\epsilon}_{erosion}}{\dot{\epsilon}_{quasi-static}} \right)^m \quad (a)$$

3) Plastic zone size ( $L$ ) for ductile materials is related to the strain-rate sensitivity and base hardness of the target material from:

$$L \sim \frac{m}{H_{base}} \quad (b)$$

4) By substituting equations a and b into equation 34, the area under the microhardness curve can be found from:

$$A \sim \frac{\left[ \left( \frac{\dot{\epsilon}_{erosion}}{\dot{\epsilon}_1} \right)^m + 1 \right] * m}{2} \quad (c)$$

Thus, equation 35 for erosion rate and erosion parameter can be rewritten as:

$$Erosion \sim E_{parameter} \sim \frac{MV^2(2.38 - 0.53 \log(H))}{\left[ \left( \frac{\dot{\epsilon}_{erosion}}{\dot{\epsilon}_{quasi-static}} \right)^m + 1 \right] * m} \quad (d)$$

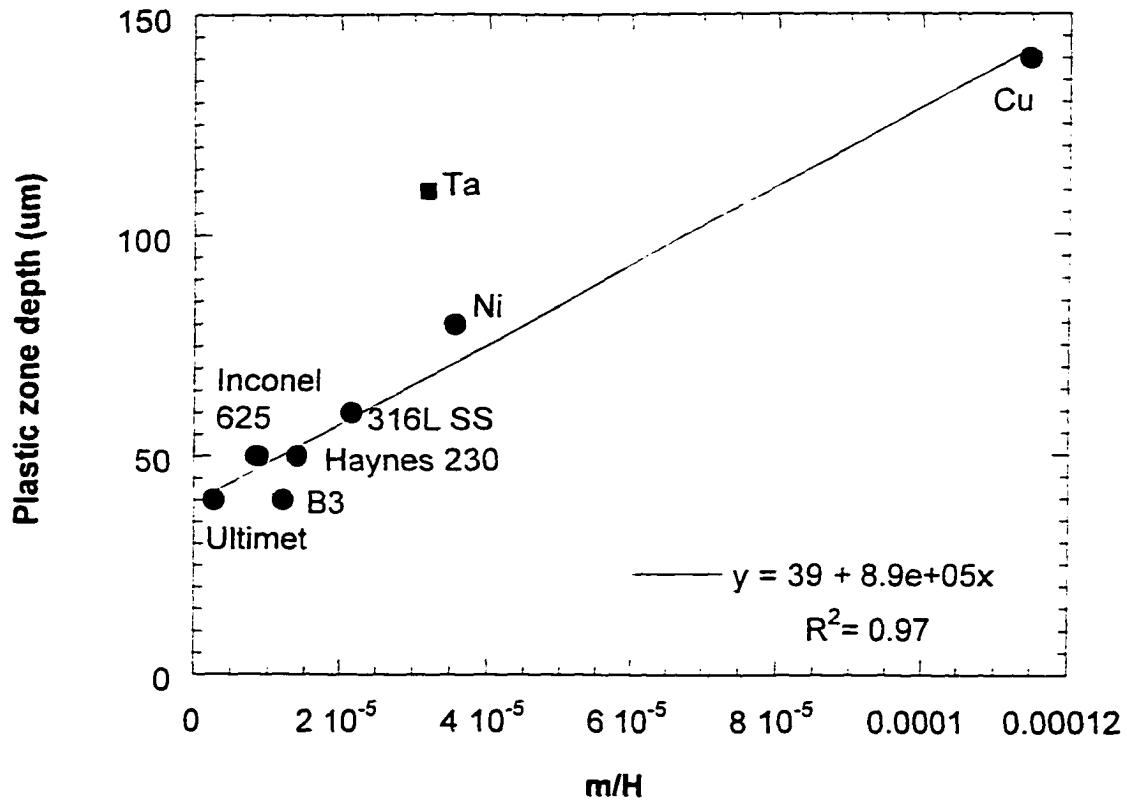


**Figure 37.** Combined effect of strain-rate sensitivity and hardness ( $m/H$ ) on plastic zone size during erosion.

This equation shows that, for a given erosion condition (i.e.,  $mV^2 = \text{const.}$ ), materials with high hardness and strain-rate sensitivity may exhibit low erosion rate. However, an increase in hardness causes a decrease in strain-rate sensitivity. Therefore, an optimum combination of hardness and strain-rate sensitivity that minimizes erosion parameter are needed for good erosion resistance.

#### ***V.D.3. Summary of the energy dissipation analysis during erosion***

Energy dissipation during erosion was analyzed by microhardness and nanoindentation techniques. Based on this analysis the following can be concluded:

1. A new parameter, "area under the microhardness curve" was developed that represents the ability of a material to absorb impact energy. By incorporating this parameter into a new erosion model, calculated erosion parameter showed good correlation with experimentally measured erosion rates.
2. Strain-rate hardening of a material during erosion significantly contributes to the increase in surface hardness during erosion. Strain-rate sensitivities of tested materials were estimated from nanoindentation tests and showed a decrease with an increase in hardness. The size of the plastic zone formed during erosion is controlled by the strain-rate sensitivity to hardness ratio ( $m/H$ ).
3. A methodology was developed to predict relative erosion resistance of ductile materials based on their hardness, strain-rate sensitivities, and strain-rates during erosion. Materials combining high hardness and strain-rate sensitivity may offer good erosion resistance.

## VI. CONCLUSIONS

The effect of mechanical properties on erosion resistance of ductile materials was investigated and the following conclusions were drawn:

1. An erosion model was developed based on considerations of energy loss. The calculated erosion parameter was developed which showed good correlation with experimentally measured erosion rates.
2. Materials combining high hardness and tensile toughness at high strain rates showed good erosion resistance. Hardness is necessary to reduce energy transferred from the particle into the material and toughness indicates the ability of the material to absorb this energy without fracture.
3. A nanoindentation method was utilized to estimate restitution coefficient ( $e$ ) within plastically deformed region. This coefficient provides a measure of the rebounding ability of a material during particle impact. It is related to their hardness,  $H$ , according to the logarithmic-type relationship:  $e = -0.68 + 0.39 \log(H)$ . Consequently, an increase in hardness produced a decrease in the amount of plastic deformation dissipated into material.
4. An experimental technique was developed to determine changes in stress-strain behavior of material below the eroded surface. Stress-strain behavior of materials near the eroded surface was similar to those during high strain-rate compression tests. Thus, strain rates imposed below the eroded surface were comparable to those measured during high strain-rate compression tests ( $10^3$ - $10^4$  s<sup>-1</sup>).

5. A new parameter, “area under the microhardness curve”, was developed which represents the ability of a material to absorb impact energy. This new parameter was incorporated into the erosion model. Calculated erosion parameter showed good correlation with experimentally measured erosion rates.
6. Strain-rate hardening of the material during erosion significantly contributes to the increase in surface hardness during erosion. Strain-rate sensitivity was estimated from the nanoindentation data and decreased with increasing material hardness. The size of the plastic zone formed during erosion is controlled by the strain-rate sensitivity to hardness ration ( $m/H$ ).
7. A methodology was developed to predict relative erosion resistance of ductile metals based on their hardness, strain-rate sensitivities, and strain-rates during erosion. Materials combining high hardness and strain-rate sensitivity may offer good erosion resistance.



## VII. REFERENCES

1. Lammarre, L., *EPRI Journal*, October/November, 1990, p. 31.
2. Meng, H.C. and Ludema, K.C., *Wear*, 181-183, 1995, pp.443-457.
3. Richman, R.H. and McNaughton, W.P., *Wear*, 140, 1990, pp.63-82.
4. Hutchings, I.M., *Monograph On The Erosion Of Materials By Solid Particle Impact*, MTI Publication No 10, 1983.
5. McCabe, L.P., Sargent, G.A., and Conrad, H., *Wear*, vol. 105, 1985, 257-277.
6. Hutchings, I.M., Winter, R.E., and Field, J.E., *Proc. R. Soc. London Ser. A* 348, 1976, pp.379-392.
7. Hutchings, I.M. and Levy, A.V., *Wear*, vol. 131, 1981, pp. 105-121.
8. Veerabhadra Rao, P., Young, S.G., and Buckley, D.H., *Wear*, vol.85, 1983, pp. 223-237.
9. Bitter, J.G.A., *Wear*, 6, 1963, pp.5-21.
10. Sundararajan, G. and Shewmon, P.G., *Wear*, vol.84, 1983, pp. 237-258.
11. Sundararajan, G., *Wear*, v.149, 1991, pp.111-127.
12. Sundararajan, G., *Wear*, v. 186-187, 1995, pp.129-144.
13. Rao, M. and Keiser, J. R., Report, Oak Ridge National Laboratory, ORNL/TM-11946, March 1992, pp. 80-83.
14. Moteff, J. and Rosa, E., Presented at the Gas Turbine Conference, Houston, *ASME*, 1985, GT-201.
15. Kuhlman-Wilsdorf, D., *Metallurgical Transactions A*, 1, 1970, p. 3171.
16. Holt, D. L., *J. Appl. Phys*, 41, 1970, p. 3197.

17. Hutchings, I.M., *Journal Of Applied Physics*, 25, 1986, pp. A212-A221.
18. Buijs, M., *J. Am. Ceram. Soc.*, 77(6), 1994, pp. 1676-78
19. Evans, A.G., Gulden, M.E., and Rosenblatt, M., *Proc. R. Soc. Lond. A*. 361, 1978, pp 342-365.
20. Doule, R.A, and Ball, A., *Wear*, Vol. 151, 1991, pp. 87-95.
21. Ninham A., *Wear Of Materials*, 1987, pp. 813-823.
22. Jennings, V.H., Head, W.J., and Manning, C.R., *Wear*, 40, 1976, pp. 93-112.
23. Hutchings, I.M., and Levy, A., *Wear*, Vol. 131, 1989, p. 105.
24. Finnie, I., Wolak, J., and Kulil, Y., *Journal of Materials*, vol. 2, 1967, p. 682.
25. Levy, A.V., *Solid Particle Erosion and Erosion Corrosion of Materials*, ASM, Materials Park, OH, 1995.
26. Oca, Y. and Hutchings I.M, *Corrosion Engineering*, 39, 1990, pp.677-687.
27. Guo, D.Z., Wang, L.J., and Li, J.Z, *Wear*, Vol. 161, 1993, pp. 173-178.
28. Lankov, A.A., *Trenie and Iznos* (Russian), 13, n.1, 1992, pp. 206-221.
29. Wert, J.J., and Oppliger., S.J, *Materials Science and Technology*, Vol. 8, September, 1992, pp.825-835.
30. Ruff, A.W., and Wiederhorn, S.M., *Treatise on Materials Science and Technology* (ed. C. Preece), Vol.16, 1979, pp.69-124, New-York/London, Academic Press.
31. Ball, A.,*Wear*, Vol. 91, 1983, pp. 201-207.
32. de Gee, A.W.J., *Wear*, Vol. 81, 1981, p. 373.
33. Venugopal Reddy, A. and Sundararajan, G., *Wear*, Vol. 103, 1985, pp. 133-148.

34. Srinvas M., Malakondaiah, G., Linda Murty, K., and Rama Rao, P, *Scripta Metallurgica et Materialia*, Vol. 25, 1991, pp.2585-2588.
35. Srinvas, M., Malakondaiah, G., and Rama Rao, P., *Acta metall. mater.* vol.41, n. 4, 1993, pp. 1301-1312.
36. Argon, A.S., Im, J., and Safoglu, R., *Metallurgical Transactions*, 6A, 1975, p. 825.
37. Lindsley, B.A. and Marder, A.R., *Mettalurgical Transactions*, 29A, 1998 (in press).
38. Hertzberg R.W., *Deformation and Fracture Mechanics of Engineering Materials*, 3<sup>d</sup>, John Wiley and Sons, 1989.
39. Lawn, B.R., Evans, A.G., and Marshall, D.D., *Journal of American Ceramic Society*, 63, 1980, p. 574.
40. Hutchings, I.M., *Wear*, 70, 1981, pp. 269-281.
41. Levin, B.F., J.N. DuPont, and A.R. Marder, *Wear*, Vol. 181-183, 1995, pp. 810-820.
42. Soderberg, S., Hogmark, S., and Swahn, H., *ASLE Transactions*, v.26, 2, 1982, pp.161-172.
43. Reddy A.V., Sundararajan G., Sivakumar, R., and Rama Rao, P., *Acta Metallurgica*, vol. 32, 1984, pp. 1305-1316.
44. Reddy, A.V. and Sandararajan, G., *Wear*, 111, 1986, 313-323.
45. Hutchings, I. M., *J, Physics, D: App. Phys.*, 10, 1977, L179.

46. Lindsley, B., *Ph.D. Thesis*, Lehigh University, 1996, pp. 28-43.
47. Lindsley, B, Stein, K, and Marder, A.R., *Measurement Science Technology*, 6, 1995, pp. 1169-1174.
48. ASTM E 384-89 standard, *Annual Book of ASTM Standards*, section 3, v. 03.01, ASTM, Philadelphia, 1994, pp.385-403.
49. Oliver, W.C. and Pharr, G.M., *J. Mater. Res.*, vol. 7, n. 6, June 1992, pp. 1564-1583.
50. Doerner, M.F. and Nix, W.D., *J. Mater. Res.*, vol. 1, 1986, p. 601.
51. Follansbee, P.S., *Metals Handbook*, ASM, Metals Park, OH, 8, 1985, pp. 198-203.
52. Nemat-Nascer, S., Isaacs, J.B., and Starrett, J.E., *Proc. Roy. Soc. London*, A 435, 1991, p. 371.
53. Johnson, K. L., *Contact Mechanics*, Cambridge University Press, Cambridge, 1985, p. 363.
54. Tabor, D., *The Hardness of Metals*, Clarendon Press, Oxford, 1951.
55. Field, J.S. and Swain, M.V., *J. Mater. Res.*, vol. 8, n.2, 1993, pp. 297-306.
56. Cook, R.F. and Pharr, G.M., *J. Hard Mater.*, 5, 1994, pp. 179-190.
57. Latham, R.V., Brah, A.S., Fok, K., and Woods., *J. Phys. D: Appl. Phys.*, vol. 10, 1977, pp. 139-150.
58. Hosford, W.F. and Caddel, R.M., *Metal Forming*, Prentice-Hall, Inc., N.J., 1983, p. 91.
59. Larsen-Badse, J., *Trans. Jap. Inst. Metals.*, vol. 9, 1960-61, p.312.

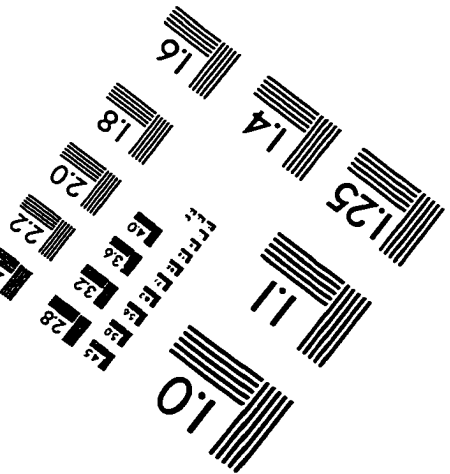
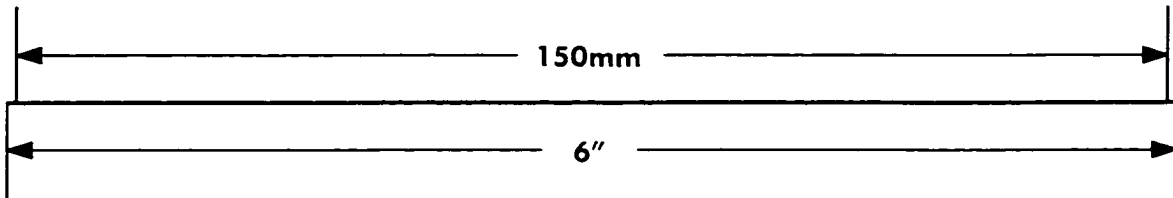
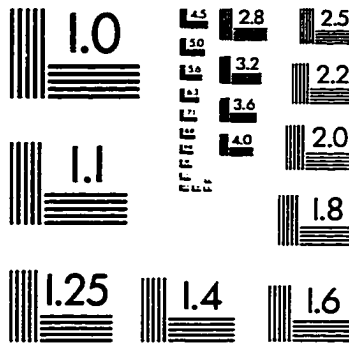
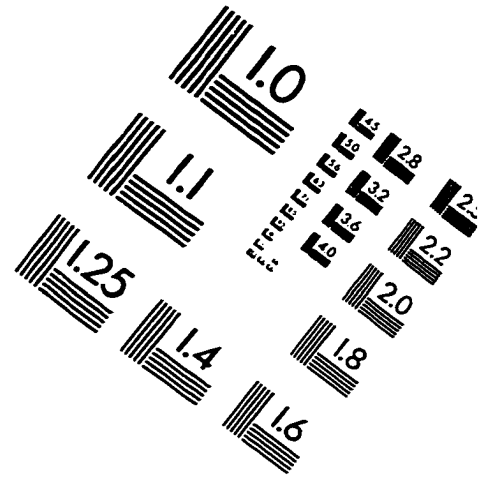
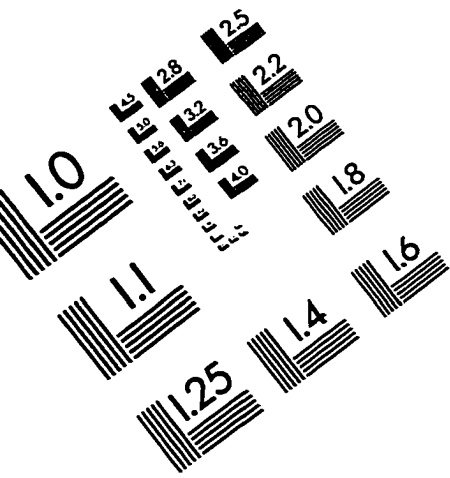
60. Sastry, D.H., Prasad, Y.V.R., and Vasu, K.I., *Journal of Materials Science*, v. 6, 1971, pp. 1433-1440.
61. Stone, D.S. and Yoder, K.B., *Journal of Materials Research*, v. 9, n. 10., 1994, 2524-2533.
62. Mulford, R.A., *Acta Metallurgica*, vol. 27., 1979, pp. 1115-1124.
63. Hertzberg, R.W., *Materials Science and Engineering*, A 190, 1995, pp. 25-32.

## VITA

Boris Levin was born to Felix and Anna Levin on June 15, 1968 in Moscow, Russia. Boris attended Moscow High school # 201 where he graduated in May, 1985. The fall of the same year he enrolled at Moscow Institute of Steel and Alloys, where he completed four years.

Boris enrolled Lehigh University in January of 1992 and began work under the advisorship of Dr. A.R. Marder in the Department of Material Science and Engineering. He received his Master's Degree in October, 1994 and has been working toward his doctorate until its completion in the spring of 1998.

# IMAGE EVALUATION TEST TARGET (QA-3)



APPLIED IMAGE, Inc  
1653 East Main Street  
Rochester, NY 14609 USA  
Phone: 716/482-0300  
Fax: 716/288-5989

© 1993, Applied Image, Inc., All Rights Reserved

